UPC CTTC

Numerical simulations of thermal storage systems. Emphasis on latent energy storage using phase change materials (PCM).

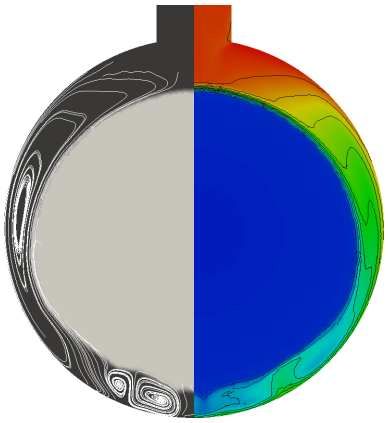

Centre Tecnològic de Transferència de Calor
Departament de Màquines i Motors Tèrmics
Universitat Politècnica de Catalunya

Pedro Andrés Galione Klot
Doctoral Thesis

Numerical simulations of thermal storage systems. Emphasis on latent energy storage using phase change materials (PCM).

Pedro Andrés Galione Klot

TESI DOCTORAL

presentada al

Departament de Màquines i Motors Tèrmics
E.T.S.E.I.A.T.
Universitat Politècnica de Catalunya

per a l'obtenció del grau de

Doctor per la Universitat Politècnica de Catalunya

Terrassa, December 2014

Numerical simulations of thermal storage systems. Emphasis on latent energy storage using phase change materials (PCM).

Pedro Andrés Galione Klot

Directors de la Tesi

Dr. Assensi Oliva Llena
Dr. Oriol Lehmkuhl Barba
Dr. Joaquim Rigola

Tribunal Qualificador

Dr. José Manuel Pinazo Ojer
Universitat Politècnica de València

Dr. Jesús Castro González
Universitat Politècnica de Catalunya

Dr. Cristóbal Cortés Gracia
Universidad de Zaragoza

Abrigamos una multitud de prejuicios
si no nos decidimos a dudar, alguna vez,
de todas las cosas en que encontremos
la menor sospecha de incertidumbre.

Discurso del método. René Descartes. 1637.

Acknowledgements

Este trabajo no hubiera sido posible sin el apoyo de muchas personas a quienes debo agradecer.

Al profesor Assensi Oliva, director del *Centre Tecnològic de Transferència de Calor* (CTTC), quien me dió la oportunidad de realizar los estudios de posgrado en dicho centro. Él ha sido muy receptivo a mis intereses a la hora de decidir los temas en los cuales centrar mi trabajo, y con su entusiasmo ha influido decididamente en mi interés por el CFD.

A Joaquim Rigola, por su guía y orientación a la hora de organizar los tiempos y objetivos de dedicación de mi trabajo, y cuyo impulso a la hora de plantearse objetivos difíciles de cumplir me ha ayudado a avanzar en situaciones de incertidumbre.

A Oriol Lehmkuhl, quien ha sido el orientador y tutor de mi trabajo con el código *TermoFluids*, que compone una gran parte de esta tesis, y con quién he aprendido mucho acerca de la simulación numérica en todos estos años.

Al profesor David Segarra, con quien he trabajado intensamente en estos últimos dos años, siendo el responsable de uno de los proyectos en los que se ha desarrollado gran parte de este trabajo.

A Ivette Rodríguez, así como a David y a Oriol, les debo agradecer su dedicación, orientación y paciencia a la hora de revisar a fondo los trabajos que componen una parte importante de esta tesis.

A Xavi Trias por su ayuda en todo lo que a simulación numérica se refiere y a Jorge Chiva, por su paciencia y sabiduría a la hora de resolver cualquier tipo de problema relacionado con la programación en C++. A Octavi y Ramiro por su inestimable ayuda con los problemas informáticos con mi computadora y el clúster. A Manolo, por su gran ayuda en la actividades experimentales, su disposición para enseñar y su (particular) sentido del humor.

Al profesor Roberto Verzicco, quien me permitió realizar una estancia en la *Università degli Studi di Roma Tor Vergata*, en la que he podido sacar ideas muy útiles en temas de simulación numérica, y en donde conocí a un grupo de gente entrañable, que hizo que dicha experiencia haya sido tan enriquecedora.

En general, a los compañeros del laboratorio, con quienes además de compartir actividades laborales, hemos compartido innumerables comidas, tertulias, cafés y partidos de fútbol; y gracias a quienes he podido conocer culturas diferentes. Especialmente al Chamo, Willy, Aleix, Fede y sus parejas, con quienes además de compartir muchas actividades y discusiones de trabajo, mi pareja y yo hemos generado una amistad que espero dure más allá de las distancias. A Leslye, Fei, Firas, Hao, Nico, con quienes hemos compartido diversas actividades y momentos muy agradables. A Aleix (nuevamente), Joan Farnos y Lluis, que a pesar de tener una vida ya for-

mada aquí, también se han abierto a compartir momentos fuera del ámbito laboral ayudando a integrarnos más fácilmente.

En el terreno institucional, debo agradecer a la *Agencia Nacional de Investigación e Innovación*, Uruguay, por haberme otorgado una beca de máster, el cual me ha dado acceso al doctorado. Al la *Facultad de Ingeniería de la Universidad de la República*, Uruguay, por haberme dado su apoyo a la hora de tomar la decisión de emigrar para realizar estudios de posgrado, y durante todo el tiempo que ha durado. Asimismo, agradecer a la *Secretaria d'Universitats i Recerca* (SUR) del *Departament d'Economia i Coneixement* (ECO) de la *Generalitat de Catalunya* y al *Fondo Social Europeo*, por la beca de doctorado que me ha permitido desarrollar este trabajo. En este sentido, debo agradecer también al CTTC por haberme apoyado durante los meses en que no contaba con ninguna beca.

En el terreno más personal, quiero agradecer a mis hermanas, padres y abuela paterna, con quienes me crié y me han apoyado siempre. A mi padre debo agradecerle el interés en la ciencia y la necesidad de llegar al fondo de las cuestiones. A mis abuelos maternos, con quienes disfruté de innumerables vacaciones en mi niñez, y quienes me acogieron en su casa durante varios años cuando tuve que emigrar a la capital a estudiar la carrera de ingeniería.

A los amigos de Uruguay, con quienes a pesar de no tener siempre un contacto fluido (generalmente por mi culpa, lo reconozco), nos hemos reencontrado muchas veces en estos años y no dejan de estar presentes.

A la tribu Gaba-Torres, mi otra familia, por su apoyo incondicional. A la tía Popi, por habernos recibido tan generosamente en su casa en Barcelona y por su apoyo y afecto inestimables durante todos estos años.

Y finalmente, y muy especialmente, a mi Sole, con quien decidimos embarcarnos en esta aventura fuera de nuestro país dejando familia y amigos, y me ha aguantado durante todo este tiempo. Creo que hemos crecido mucho como pareja con esta experiencia y que volveremos a Uruguay siendo más maduros y fuertes (y más viejos, claramente).

Abstract

The present thesis aims at studying the use of phase change materials (PCM) in thermal energy storage (TES) applications and to develop and implement different numerical tools for their evaluation. Numerical analysis is currently an indispensable tool for the design, evaluation and optimization of thermal equipment, complementing the experimental techniques.

Two levels of analysis are carried out, one in the field of Computational Fluid Dynamics (CFD), allowing the accurate simulation of the complex heat transfer and fluid dynamics phenomena present in solid-liquid phase change problems; and another one in which the governing equations are treated assuming several suitable simplifications and integrating empirical correlations, intended for the study of whole thermal storage systems throughout several charge/discharge cycles.

Furthermore, the specific application of thermal storage in concentrated solar power (CSP) stations is studied. Different single-tank systems, making use of both sensible and latent energy capacities of the materials, are evaluated and compared against the standard two-tank molten-salt systems used in current CSP plants. Moreover, a new single-tank TES concept which combines the use of solid and PCM filler materials is proposed, with promising results for its utilization in CSP.

All the contents of the main chapters of this thesis, apart from the Introduction and Conclusions, have been either published or submitted to international journals, and thus, they are written in order to be self-contained. For this reason, some concepts and equations are repeated throughout different chapters.

In chapters 2 and 3, a numerical fixed-grid enthalpy model for the simulation of the solid-liquid phase change is developed. This technique is implemented using the Finite Volume Method in a collocated unstructured domain discretization and using explicit time integration schemes. Issues regarding the form of the energy equation, the treatment of the pressure equation as well as the momentum source term coefficient introduced by the enthalpy-porosity method are described in detail in the first chapter. In the second, the possibility of taking into account the variation of the different thermo-physical properties with the temperature is dealt with. Thermal expansion and contraction associated to the phase change are taken into account in the conservation equations and different strategies for the numerical treatment of the energy equation are discussed in detail. Furthermore, simulations of an interesting and challenging case of melting of an encapsulated PCM are carried out using two and three-dimensional meshes, and the results are compared against experimental results from the literature.

In the next two chapters, the issue of numerically simulating whole single-tank TES systems is developed. These systems are composed of a single tank filled with solid and/or PCM materials, forming a packed bed through which a heat transfer fluid

(HTF) flows. Thermal stratification separates the fluid layers at different temperatures, with the hot fluid remaining at the top and the cold at the bottom. The vertical temperature gradient is generally referred to as "thermocline" and it is desirable to keep it as steep as possible in order to maintain the exergy available as high as possible. Different designs of single-tank TES systems —classified according to the filler material/s used— are evaluated for their use in CSP plants. The analysis is performed evaluating different aspects —as the energy effectively stored/released and the efficiency in the use of the theoretical capacity— after several charge/discharge cycles, in order to obtain results independent of the initial thermal state. The operating time is not fixed, but depends on the temperature of the fluid coming out of the tank, since it is limited by the restrictions of the receiving equipment (solar field and power block). It is observed how the degradation of the stratification occurs after several cycles due to the temperature restrictions. In this context, a new concept of single-tank TES is presented, which consists of the combination of different layers of solid and PCM filler materials in a suitable manner, diminishing the thermocline degradation and increasing the use of the theoretical capacity. This concept, which is called Multi-Layered Solid PCM (MLSPCM), is demonstrated as a promising alternative for its use in CSP plants.

Contents

Abstract **v**

1 Introduction **1**
1.1 Prologue . . . 1
1.1.1 Solid-liquid phase-change modeling . . . 2
1.1.2 TES in CSP . . . 3
1.2 Background . . . 4
1.3 Objectives and Outline . . . 5
1.4 Applicability . . . 6
References . . . 6

2 Fixed-Grid Modeling of Solid-Liquid Phase-Change **11**
2.1 Introduction . . . 13
2.2 Mathematical model . . . 14
2.2.1 Nondimensionalization of the equations . . . 16
2.3 Numerical procedure . . . 17
2.3.1 Time discretization . . . 18
2.3.2 Space discretization . . . 20
2.3.3 Pressure equation . . . 26
2.3.4 Different expressions of the momentum source term factor (S) . . . 29
2.3.5 Algorithm overview . . . 32
2.4 Numerical results . . . 32
2.4.1 Gallium melting . . . 32
2.4.2 Melting of pure tin . . . 33
2.4.3 Spherical capsules filled with N-Octadecane . . . 35
2.5 Conclusions . . . 38
References . . . 39

3 Fixed-grid modeling with variable thermo-physical properties. Melting of n-Octadecane inside a spherical capsule. **43**
3.1 Introduction . . . 44
3.2 Mathematical modeling . . . 46
3.2.1 Enthalpy - temperature relations . . . 47
3.3 Numerical implementation . . . 51
3.3.1 Overview of the previous implementation . . . 51
3.3.2 Mass and momentum . . . 53
3.3.3 Energy . . . 62

3.4 Definition of the case study . . . 64
3.4.1 Spatial discretization schemes . . . 65
3.4.2 Physical properties . . . 67
3.4.3 Initial and boundary conditions . . . 71
3.5 Results . . . 73
3.5.1 Convective scheme and grid convergence . . . 74
3.5.2 Thermo-physical properties . . . 74
3.5.3 2D vs. 3D . . . 76
3.5.4 Agreement between experimental and numerical results . . . 81
3.6 Conclusions . . . 88
References . . . 89

4 Numerical modeling and proposal of a multi-layered solid-PCM thermocline thermal storage concept for CSP. 95
4.1 Introduction . . . 98
4.2 Mathematical modeling and numerical implementation . . . 101
4.2.1 Energy . . . 102
4.2.2 Momentum . . . 104
4.2.3 Exergy . . . 105
4.2.4 Discretization details . . . 105
4.2.5 Model validation . . . 106
4.3 Evaluation of different solutions . . . 108
4.3.1 Study cases . . . 109
4.3.2 Results and discussion . . . 113
4.4 Conclusions . . . 126
References . . . 127

5 Evaluation of MLSPCM for its application in a 50MWe CSP plant. 131
5.1 Introduction . . . 134
5.2 Mathematical modeling and numerical implementation . . . 136
5.2.1 Packed bed . . . 136
5.2.2 Tank walls, insulation and foundation . . . 139
5.3 Cases of isolated TES under nominal conditions . . . 140
5.3.1 Results and discussion . . . 142
5.4 Cases of TES integrated into a CSP facility . . . 151
5.4.1 Operating conditions . . . 151
5.4.2 Tank configurations . . . 154
5.4.3 Results and discussion . . . 155
5.5 Conclusions . . . 159
References . . . 161

6 Conclusions and further research **165**
6.1 Conclusions 165
6.2 Further research 169
References 170

A Main publications in the context of this thesis **171**
A.1 Journal papers 171
A.2 Conference papers 171

1

Introduction

1.1 Prologue

Solid-liquid phase change processes are present in countless situations. Melting and freezing phenomena play an important role in our world since the formation of the Earth, until the actual days where it is present in many industrial applications, as the manufacturing of metal alloys or glass [1]. It is also worth mentioning the renewed interest that has been developed during the last years in the so-called phase change materials (PCM) as thermal-energy-storing agents —e.g. in storage devices for solar thermal power stations [2]— as a way of increasing the efficiency in the utilization of energy [3].

Thermal energy storage (TES) systems are useful for reducing the mismatch between energy supply and demand. For example, their application into heating and cooling systems allow to reduce the consumed electricity costs by shifting the production of heat/cold into off-peak hours. Furthermore, they allow to "flatten" the load curve of the heat/cold pumps, spreading their operation into more hours of the day, with the result of needing smaller equipment, working closer to their optimal operation point and thus, with a higher efficiency.

TES systems are an essential feature to make a major profit of solar energy, since they allow using the thermal energy stored in hours of high solar radiation in times of lower radiation and higher energy demands. In fact, in low-temperature solar water heating systems, a water tank working as a thermal storage device is always included. In solar power generation stations, the incorporation of TES systems produce an increase in system reliability and generation capacity, and a decrease of the levelized cost of electricity (LCOE) [4, 5].

Harnessing the inherent latent energy changes of the phase transitions of the materials, should result in the design of more compact and hopefully cheaper thermal storage devices than those only relying on the materials sensible energy capacity.

Although liquid-vapor phase change usually results in greater latent energy changes, solid-liquid transitions are usually preferred due to their lower changes in density. This is an important aspect to take into account when designing suitable devices for the containment of the PCMs.

PCMs are being used or studied for its use in several thermal storage applications in a wide range of temperatures. Some examples are the ice storage for air conditioning (see e.g. [6]), the integration of PCMs into different elements of the buildings for reducing the energy demand of heating and cooling (see e.g. [7]), thermal storage for both low-temperature solar collectors (see e.g. [8]) and medium-high temperature concentrating solar power stations (treated in more detail next in this work).

A common feature of many of the PCMs usually considered —such as paraffins, hydrated salts and salt mixtures— is their low thermal conductivity. For this reason, different strategies for increasing the heat transfer rate of devices using PCMs are considered [9, 10]. One of the most studied thermal enhancement options is the containment of the PCM in small capsules, in order to obtain a high surface-to-volume ratio. Studies of storage systems consisting of packed beds of encapsulated PCM are abundant in the literature, e.g. [11–13].

On the other hand, it has been seen that natural convection effects in the melting of PCMs enclosed in different kind of cavities, play a significant role in the evolution of the melting rate and shape of the solid-liquid interface (see e.g. [14,15]). Besides the dynamics and heat transfer phenomena involved within the fluid phase, simulations need to address the heat transfer within the solid phase and an accurate representation of the moving boundary between phases.

1.1.1 Solid-liquid phase-change modeling

One of the first works on the modeling of the solid-liquid phase change was carried out by J. Stefan in 1891 [16], to whom the development of the well-known Stefan condition is attributed, although some previous works had already addressed this problem [17]. This condition describes the velocity of the interface of a moving boundary between solid and liquid phases of the same substance, which depends on the balance of heat fluxes coming from the solid and liquid phases and on the latent energy released/absorbed in the melting/solidification. Some analytical solutions have been found for some one-dimensional problems but the usual approach for the general kind of problems is through numerical methods.

During a solid-liquid phase change process, density variations due to temperature changes combined with the gravitational force, produce fluid motion which affects the heat transfer mechanism (natural convection) and evolution of the solid-liquid interface. Therefore, it is of interest to be able to accurately simulate this phenomenon and its interaction with the interface. This is a challenging task, not only due to the inherent difficulty of simulating convection phenomena, but also to the added

problem of presenting a moving boundary, whose evolution is unknown a priori and has to be determined as part of the solution.

There are different techniques for the numerical simulation of solid-liquid phase change, which can be broadly classified into fixed-grid models [18], adaptive mesh models [19] and mixed Eulerian-Lagrangian methods [20]. Fixed-grid models use a fixed mesh for the entire domain independently of the location of the liquid phase; adaptive mesh models adapt the mesh in order to follow the evolution of the liquid-solid interface; while in Eulerian-Lagrangian methods the computations are performed in a fixed grid but the interface is explicitly tracked by a set of extra points. Fixed grid methods are mathematically and computationally easier to implement than other methods. Adaptive mesh methods admit coarser meshes —as the grid density is dynamically modified in order to be higher near the interface— than fixed grid methods for the same accuracy. On the other hand, fixed-grid models allow to simulate flow through "mushy zones" developed in a solid-liquid phase change ocurring at a temperature range. One commonly cited reference which compares a fixed-grid model and an adaptive-mesh model is [21]

Fixed-grid enthalpy models have been extensively used for solid-liquid phase change CFD simulations. Generally, implicit time schemes are used by most authors [18, 22–24].

1.1.2 TES in CSP

Nowadays, many CSP plants incorporate a molten-salt two-tank TES system (e.g. Andasol and Extresol in Spain, Crescent Dunes and Solana in USA), which makes use of the sensible energy capacity of the molten-salt [25, 26]. However, different TES designs resulting in lower investment costs are currently under study, some of which are also based on the sensible energy capacity of the materials, such as thermocline single-tanks [27, 28] and concrete storage designs [29].

In thermocline systems, the fluid with both high and low temperature levels is contained in a single tank. Thermal stratification is the mechanism separating them, and the thermal gradient produced within the fluid is called thermocline. The thermocline thickness indicates the amount of thermal mixing, which may be due to natural convection effects (see e.g. [30, 31]) and strong inlet flow currents [32], and is intended to be maintained at a minimum. A modification to the original concept, aiming at reducing the thermal mixing and also reducing the amount of molten-salt used, is to fill the tank with a cheaper solid material such as quartzite rocks, granite, sand [27], asbestos-containing wastes [33], forming a porous packed bed through which the heat transfer fluid flows.

On the other hand, several researchers have been investigating the use of phase change materials (PCM) as thermal storage media for CSP facilities. Liu et al. [9] carried out an extensive review of high-temperature phase change storage materials

and of thermal enhancement techniques. For example, Michels and Pitz-Paal [34] performed a numerical and experimental investigation of storage systems using different PCMs with cascaded melting points, contained in shell and tube heat exchangers, for parabolic trough CSP plants. Shabgard et al. [35] performed a numerical analysis of cascaded latent heat storage with gravity-assisted heat pipes for CSP applications. Nithyanandam et al. [36] studied packed bed thermal storage with encapsulated PCMs for CSP by means of a numerical model. They performed parametric analyses and established guidelines for the design of latent storage systems. Flueckiger et al. [13] analyzed latent-heat-augmented thermocline storage for CSP using an integrated system-level model for the whole CSP plant and evaluated the effect of the increase of the storage capacity with the latent heat. Limitations in the thermal performance of tanks including PCMs were observed, while some improvement was obtained with some of the cascaded PCM designs.

Furthermore, Steinmann and Tamme [37] studied the combination of latent and sensible storage heat exchangers specially suited for direct steam generation solar field technology (DSG). A PCM storage unit was intended for producing the vapor generation (evaporation) and two concrete storage units for storing the sensible portion of the fluid's energy (pre and superheating).

1.2 Background

The present thesis has been developed at the *Heat and Mass Transfer Technological Center* (CTTC) of the *Technical University of Catalonia* (UPC). CTTC is a research center whose activities are focused on two main lines, one dedicated to the mathematical formulation, numerical resolution and experimental validation of fluid dynamics and heat and mass transfer phenomena, and another involving the application of the acquired know-how from the basic studies into the thermal and fluid dynamic optimisation of thermal systems and equipment. Solar energy systems and thermal storage are within the main topics of research of CTTC. A list of the activities, research projects and publications of the center can be found in [38].

Some of the models presented in this thesis have been implemented into the CFD platform *TermoFluids* (TF) [39], developed by *Termo Fluids S.L.* —a spin-off of the CTTC-UPC— which is a high performance computing code designed for three-dimensional (3D) CFD simulations in unstructured meshes, using the Finite Volume Method (FVM) for the discretization of the governing equations. Termo Fluids S.L. is was born in year 2006 from members of the CTTC and, together with CTTC, have a high capacity of simulating thermal systems and equipment.

Several theses and scientific papers in the subject of solid-liquid phase change modeling have been published by researchers from the CTTC in the past, e.g. [23, 40–42]. Theses of Miquel Costa [40] and Bárbara Vidal [42], dealing with the fixed-

grid modeling of solid-liquid phase change in structured meshes and using implicit integration schemes, have served as a very good starting point for the work developed in this thesis.

1.3 Objectives and Outline

The work developed in the framework of this thesis can be encompassed into three main objectives. First, to develop and implement a numerical model for the simulation of solid-liquid phase change phenomena in a highly parallel, unstructured CFD platform. Second, to develop and implement a numerical model of thermal storage systems, consisting of a tank filled with solid and/or PCM materials forming a packed bed through which a heat transfer fluid flows, for the fast simulation of several charge/discharge cycles. Third, to study and evaluate different single-tank TES systems for their application into concentrated solar power plants.

The next two chapters are devoted to the fulfillment of the first objective. In *chapter 2*, a fixed-grid enthalpy model is developed in detail. This model has been implemented into the CFD platform *TermoFluids* (TF), As the intention is to be able make use of the turbulence models already available within the TF framework for the simulation of the liquid phase flow, the present fixed-grid model is designed for its use with explicit time integration schemes, specially suited for the simulation of turbulence.

In *chapter 3*, the referred model is extended in order to take into consideration the variation of the thermo-physical properties with the temperature, with a special consideration of the change in density present in the phase change. Several modifications to the model developed in chapter 2 are indicated in detail. Furthermore, simulations of a case of the constrained melting of a PCM contained in a spherical capsule are performed using two and three-dimensional meshes, and the results are compared against experimental results from the literature.

The second and third objectives are addressed in chapters 4 and 5. *Chapter 4* deals with the development of a numerical model for the simulation of tanks filled with solid particles and/or PCM capsules forming a packed bed, through which a HTF flows exchanging heat. In the same chapter, a new concept of thermocline-like storage system is presented, in which both solid and PCM filler materials are suitably combined. The main idea behind MLSPCM configurations is the inclusion of high and low melting-point PCMs as filler materials at the ends of the tank, close to the inlet/outlet ports. This packed bed configuration is named Multi-Layered Solid-PCM (MLSPCM) and is compared against different thermocline-like systems, which can be classified according to the filler materials included as: single solid, single PCM and cascaded-PCM. The analysis is performed evaluating different aspects —as the energy effectively stored/released and the efficiency in the use of the theoretical ca-

pacity— after several charge/discharge cycles, in order to obtain results independent of the initial thermal state. The operating time is not fixed, but is dependent on the temperature of the fluid coming out of the tank, since it is limited by the restrictions of the receiving equipment (solar field and power block). It is observed how the degradation of the stratification occurs after several cycles due to the temperature restrictions. The performed study shows that the multi-layered solid-PCM concept is a promising alternative for its use as in thermal storage units for CSP plants.

In *chapter 5* the MLSPCM concept is used for making up single-tank TES systems for a CSP plant. 50 MWe parabolic trough plant Andasol 1 (Granada, Spain) is adopted as a reference. Two sets of analyses are performed, one with the objective of testing the TES systems individually, by defining specific operating conditions and taking the systems to a periodic steady state; and another, aiming at the perfomance evaluation after several days of operation in a CSP plant, in which the weather variability and the thermal behavior of tank walls and foundation are simulated. For the second set, the numerical model is integrated into the modular object-oriented code NEST [43], which links the different models corresponding to the elements under study.

Finally, conclusions are taken and an overview of further research is presented.

1.4 Applicability

A significant part of the present work has been developed within the framework of different research projects of the CTTC with the industry, such as *SEILA - New technologies for an efficient, ecologic and intelligent washing system for textiles of the future* [44] and *TESCONSOL - Thermal storage for concentrating solar power plants* [45].

References

[1] L. S. Yao and J. Prusa, *Advances in Heat Transfer. Melting and Freezing*, vol. 19. Elsevier, 1989.

[2] A. Gil, M. Medrano, I. Martorell, A. Lázaro, P. Dolado, B. Zalba, and L. F. Cabeza, "State of the art on high temperature thermal ebergy storage for power generation. part 1—Concepts, materials and modellization," *Renew. Sust. Energ. Rev.*, no. 14, pp. 31–55, 2010.

[3] B. Zalba, J. M. Marín, L. F. Cabeza, and H. Mehling, "Review on thermal energy storage with phase change: materials, heat transfer analysis and applications," *Appl. Therm. Eng.*, no. 23, pp. 251–283, 2003.

[4] M. Medrano, A. Gil, I. Martorell, X. Potau, and L. F. Cabeza, "State of the art on high temperature thermal ebergy storage for power generation. part 2—Case studies," *Renew. Sust. Energ. Rev.*, no. 14, pp. 56–72, 2010.

[5] G. J. Kolb, C. K. Ho, T. R. Mancini, and J. A. Gary, "Power Tower Technology Roadmap and Cost Reduction Plan," Tech. Rep. SAND2011-2419, Sandia National Laboratories, 2011.

[6] R. Verma, R. Hudler, and B. Maeda, "Ice storage air conditioners. compliance options application. staff report.," tech. rep., California Energy Comission, 2003.

[7] Y. Zhang, G. Zhou, K. Lin, Q. Zhang, and H. Di, "Application of latent heat thermal energy storage in buildings: State-of-the-art and outlook," *Build. Environ.*, no. 42, pp. 2197–2209, 2007.

[8] H. Mehling, L. F. Cabeza, S. Hippeli, and S. Hiebler, "PCM-module to improve hot water heat stores with stratification," *Renew. Energ.*, vol. 28, pp. 699–711, 2003.

[9] M. Liu, W. Saman, and F. Bruno, "Review on storage materials and thermal performance enhancement techniques for high temperature phase change thermal storage systems," *Renew. Sust. Energ. Rev.*, vol. 16, pp. 2118–2132, 2012.

[10] S. Jegadheeswaran and S. D. Pohekar, "Performance enhancement in latent heat thermal storage system: A review," *Renew. Sust. Energ. Rev.*, vol. 13, pp. 2225–2244, 2009.

[11] K. A. R. Ismail and R. Stuginsky Jr., "A parametric study on possible fixed bed models for pcm and sensible heat storage," *Appl. Therm. Eng.*, vol. 19, pp. 757–788, 1999.

[12] J. P. Bédécarrats, J. Castaing-Lasvignottes, F. Strub, and J. P. Dumas, "Study of a phase change energy storage using spherical capsules. Part ii: Numerical modelling," *Energ. Convers. Manage.*, vol. 50, pp. 2537–2546, 2009.

[13] S. M. Flueckiger and S. V. Garimella, "Latent heat augmentation of thermocline energy storage for concentrating solar power —A system-level assessment," *Appl. Energ.*, vol. 116, pp. 278–287, 2014.

[14] C. J. Ho and V. R., "Heat transfer during melting from an isothermal vertical wall," *J. Heat Trans.-T. ASME*, vol. 106, pp. 12–19, 1984.

[15] F. Wolff and R. Viskanta, "Melting of a pure metal from a vertical wall," *Exp. Heat Transfer*, vol. 1, pp. 17–30, 1987.

[16] J. Stefan, "Ueber die Theorie der Eisbildung, insbesondere ueber die Eisbildung im Polarmeere," *Ann. Physik Chemie*, vol. 42, pp. 269–286, 1891.

[17] `http://www.encyclopediaofmath.org/index.php?title=Stefan_problem&oldid=15955`. Encyclopedia of Mathematics, "Stefan Problem."

[18] V. Voller and C. Prakash, "A fixed grid numerical modelling methodology for convection-diffusion mushy region phase change problems," *Int. J. Heat Mass Tran.*, vol. 30, pp. 1709–1719, 1987.

[19] G. Beckett, J. A. Mackenzie, and R. M. L., "A Moving Mesh Finite Element Method for the Solution of Two-dimensional Stefan Problems," *J. Comput. Phys.*, vol. 168, pp. 500–518, 2001.

[20] H. S. Udaykumar, R. Mittal, and W. Shyy, "Computation of Solid-Liquid Phase Fronts in the Sharp Interface Limit on Fixed Grids," *J. Comput. Phys.*, vol. 153, pp. 535–574, 1999.

[21] R. Viswanath and Y. Jaluria, "A comparison of different solution methodologies for melting and solidification problems in enclosures," *Numer. Heat Tr. B-Fund.*, vol. 24, pp. 77–105, 1993.

[22] A. D. Brent, V. R. Voller, and K. J. Reid, "Enthalpy-Porosity Technique for Modelling Convection-Diffusion Phase Change: Application to the Melting of a Pure Metal," *Numer. Heat Transfer*, vol. 13, pp. 297–318, 1988.

[23] M. Costa, A. Oliva, C. D. Pérez-Segarra, and R. Alba, "Numerical simulation of solid-liquid phase change phenomena," *Comput. Method. Appl. M.*, vol. 91, no. 1-3, pp. 1123–1134, 1991.

[24] F. L. Tan, S. F. Hosseinizadeh, J. M. Khodadadi, and L. Fan, "Experimental and computational study of constrained melting of phase change materials (PCM) inside a spherical capsule," *Int. J. Heat Mass Tran.*, vol. 52, pp. 3464–3472, 2009.

[25] U. Herrmann, B. Kelly, and H. Price, "Two-tank molten salt storage for parabolic trough solar power plants," *Energy*, vol. 29, pp. 883–893, 2004.

[26] J. I. Ortega, J. I. Burgaleta, and F. M. Téllez, "Central Receiver System Solar Power Plant Using Molten Salt as Heat Transfer Fluid," *J. Sol. Energ.-T. ASME*, vol. 130, pp. 024501–1–6, 2008.

[27] J. E. Pacheco, S. K. Showalter, and W. J. Kolb, "Development of a Molten-Salt Thermocline Thermal Storage System for Parabolic Trough Plants," *J. Sol. Energ.-T. ASME*, vol. 124, pp. 153–159, 2002.

[28] A. Yang and S. V. Garimella, "Molten-salt thermal energy storage in thermoclines under different environmental boundary conditions," *Appl. Energ.*, vol. 87, pp. 3322–3329, 2010.

[29] R. Tamme, D. Laing, and W. D. Steinmann, "Advanced Thermal Energy Storage Technology for Parabolic Trough," *J. Sol. Energ.-T. ASME*, vol. 126, pp. 794–800, 2004.

[30] J. L. Shyu, R.J. and L. Fang, "Thermal analysis of stratified storage tanks," *J. Sol. Energ.-T. ASME*, vol. 111, pp. 54–61, 1989.

[31] I. Rodríguez, J. Castro, C. Pérez-Segarra, and A. Oliva, "Unsteady numerical simulation of the cooling process of vertical storage tanks under laminar natural convection," *Int. J. Therm. Sci.*, vol. 48, pp. 708–721, 2009.

[32] L. J. Shah and S. Furbo, "Entrance effects in solar storage tanks," *Sol. Energy*, vol. 75, pp. 337–348, 2003.

[33] N. Calvet, J. C. Gomez, A. Faik, V. V. Roddatis, A. Meffre, G. C. Glatzmaier, S. Doppiu, and X. Py, "Compatibility of a post-industrial ceramic with nitrate molten salts for use as filler material in a thermocline storage system," *Appl. Energ.*, vol. 109, pp. 387–393, 2013.

[34] H. Michels and R. Pitz-Paal, "Cascaded latent heat storage for parabolic trough solar power plants," *Sol. Energy*, vol. 81, pp. 829–837, 2007.

[35] H. Shabgard, C. W. Robak, T. L. Bergman, and A. Faghri, "Heat transfer and exergy analysis of cascaded latent heat storage with gravityassisted heat pipes for concentrating solar power applications," *Sol. Energy*, vol. 86, no. 3, pp. 816–830, 2012.

[36] K. Nithyanandam, R. Pitchumani, and A. Mathur, "Analysis of a latent thermocline storage system with encapsulated phase change materials for concentrating solar power," *Appl. Energ.*, vol. 113, pp. 1446–1460, 2014.

[37] W. Steinmann and R. Tamme, "Latent heat storage for solar steam systems," *J. Sol. Energ.-T. ASME*, vol. 130, pp. 011004–1–011004–5, 2008.

[38] `http://www.cttc.upc.edu`.

[39] O. Lehmkuhl, C. D. Pérez-Segarra, R. Borrell, M. Soria, and A. Oliva, "TERMOFLUIDS: A new Parallel unstructured CFD code for the simulation of turbulent industrial problems on low cost PC Cluster," *Lect. Notes Comput. Sci. Eng.*, vol. 67, pp. 275–282, 2009.

[40] M. Costa, *Desenvolupament de criteris numèrics per a la resolució de la transferencia de calor en medis amb conducció, convecció i canvi de fase sólid-líquid. Contrastació experimental.* PhD thesis, Universitat Politècnica de Catalunya, Spain, 1993.

[41] M. Costa, A. Oliva, and C. D. Pérez-Segarra, "A three-dimensional numerical study of melting inside a heated horizontal cylinder," *Numer. Heat Tr. A-Appl.*, vol. 32, no. 5, pp. 531–553, 1997.

[42] B. Vidal, *Modelización del cambio de fase sólido líquido. Aplicación a sistemas de acumulación de energia térmica.* PhD thesis, Universitat Politècnica de Catalunya, Spain, 2007.

[43] R. Damle, O. Lehmkuhl, G. Colomer, and I. Rodríguez, "Energy simulation of buildings with a modular object-oriented tool," in *Proc. ISES Solar World Congress 2011*, 2011.

[44] "SEILA - New technologies for an efficient, ecologic and intelligent washing system for textiles of the future," 2010-2012. Research Project C07973, ref. CEN-20091005. Company: FAGOR Electrodomésticos.

[45] "TESCONSOL - Thermal storage for concentrating solar power plants," 2011-2014. Research Project Q-00023, ref. CEN-20091005. Company: EIT-KIC InnoEnergy project.

2

Fixed-Grid Modeling of Solid-Liquid Phase-Change

Contents of this chapter have been published in:

P. A. Galione, O. Lehmkuhl, J. Rigola and A. Oliva, "Fixed-Grid Modeling of Solid-Liquid Phase Change in Unstructured Meshes Using Explicit Time Schemes," *Numer. Heat Tr. B-Fund.*, vol. 65, pp. 27–52, 2014.

Abstract

Fixed-grid enthalpy models have been extensively used for solid-liquid phase change CFD simulations with implicit time schemes. In this work, this technique is implemented for explicit time schemes and collocated unstructured domain discretization, due to the interest in coupling phase change formulation with turbulence models for the liquid motion.

Issues regarding the form of the energy equation, the treatment of the pressure equation as well as the momentum source term coefficient introduced by the enthalpy-porosity method are described in detail.

Numerical implementation is tested with different study cases, showing a good agreement with other experimental and numerical results.

NOMENCLATURE

A	surface area
C_p	specific heat at constant pressure
$\overrightarrow{d_{PF}}$	distance vector, going from present node centroid to neighbor node centroid
$\overrightarrow{d_{Psf}}$	distance vector, going from present node centroid to face centroid
f	mass liquid fraction
$\vec{f}$	momentum source term
g	gravity acceleration
h	specific total enthalpy
$\hat{j}$	unitary vector in the vertical direction
k	thermal conductivity
L	specific latent enthalpy
$m, \dot{m}$	mass and mass flux
$\hat{n}$	surface normal vector
p_d	hydrodynamic part of the pressure ($p_d = p + \rho g y$, where y is the vertical coordenate)
Pr	Prandtl number
Ra	Rayleigh number
R	Sum of convective and diffusive terms
S	Momentum source term coefficient introduced by the porosity method
Ste	Stefan number
T	temperature
$u, \vec{u}, \vec{u}^p$	velocity magnitude, vector and predictor velocity vector
Δt	time step
V	volume
α	thermal diffusivity ($\alpha = \frac{\lambda}{\rho C_p}$)
β	volumetric expansion coefficient
ϵ	volume liquid fraction (porosity)
μ	dynamic viscosity
ρ	density
ϕ	non-dimensional temperature

Superscripts and subscripts:

f	corresponding to a face
F	corresponding to a neighbor node/cell
l, liq	liquid phase
P	corresponding to the present node/cell
s, sol	solid phase
sf	solid face
$*$	non-dimensional variable

2.1 Introduction

Solid-liquid phase change processes are present in countless situations. Melting and freezing phenomena play an important role in our world since the formation of the Earth, until the actual days where it is present in many industrial applications, as the manufacturing of metal alloys or glass [1]. It is also worth mentioning the renewed interest that has been developed during the last years in the so-called phase change materials (PCM) as thermal-energy-storing agents —e.g. in storage devices for solar thermal power stations [2]— as a way of increasing the efficiency in the utilization of energy [3].

One of the first works on the modeling of the solid-liquid phase change was carried out by J. Stefan in 1891 [4], to whom the development of the well-known Stefan condition is attributed, although some previous works had already addressed this problem [5]. This condition describes the velocity of the interface of a moving boundary between solid and liquid phases of the same substance, which depends on the balance of heat fluxes coming from the solid and liquid phases and on the latent energy released/absorbed in the melting/solidification. Some analytical solutions have been found for some one-dimensional problems but the usual approach for the general kind of problems is through numerical methods.

During a solid-liquid phase change process, density variations due to temperature changes combined with the gravitational force, produce fluid motion which affects the heat transfer mechanism (natural convection) and evolution of the solid-liquid interface. Therefore, it is of interest to be able to accurately simulate this phenomenon and its interaction with the interface. This is a challenging task, not only due to the inherent difficulty of simulating convection phenomena, but also to the added problem of presenting a moving boundary, whose evolution is unknown a priori and has to be determined as part of the solution.

There are different techniques for the numerical simulation of solid-liquid phase change, which can be broadly classified into fixed-grid models [6], adaptive mesh models [7] and mixed Eulerian-Lagrangian methods [8]. Fixed-grid models use a fixed mesh for the entire domain independently of the location of the liquid phase; adaptive mesh models adapt the mesh in order to follow the evolution of the liquid-solid

interface; while in Eulerian-Lagrangian methods the computations are performed in a fixed grid but the interface is explicitly tracked by a set of extra points. Fixed grid methods are mathematically and computationally easier to implement than other methods. Adaptive mesh methods admit coarser meshes —as the grid density is dynamically modified in order to be higher near the interface— than fixed grid methods for the same accuracy. On the other hand, fixed-grid models allow to simulate flow through "mushy zones" developed in a solid-liquid phase change ocurring at a temperature range. One commonly cited reference which compares a fixed-grid model and an adaptive-mesh model is [9]

Fixed-grid enthalpy models have been extensively used for solid-liquid phase change CFD simulations. Generally, implicit time schemes are used by most authors [6, 10–12].

This work deals with solid-liquid phase change simulation using fixed-grid enthalpy modeling but using explicit time schemes. This is due to the intention of coupling the phase change formulation with some turbulence modeling for the liquid motion, where explicit time schemes are common.

Some issues regarding the formulation of the energy equation, the treatment of the pressure equation (resulting from the pressure-velocity decoupling) as well as the form of the momentum source term coefficient introduced by the enthalpy-porosity method are treated in detail.

Resulting numerical implementation, using an unstructured domain discretization and a collocated mesh scheme, is tested using some study cases for which experimental and numerical results have been obtained from the literature.

2.2 Mathematical model

When the PCM changes of phase, natural convection is produced due to the difference between solid and liquid densities and gravity action. To simulate this phenomenon, Navier-Stokes and energy equations are numerically solved. Some of the most relevant simplyfying assumptions that are made here are:

- Incompressible fluid.
- Boussinesq aproximation (density is considered constant, except in the gravity forces term).
- Constant thermo-physical properties and equal between solid and liquid states.

Based on the above mentioned hypotheses and adopting the enthalpy-porosity model to account for the phase change phenomenon [6, 10], mass, momentum and

energy equations can be written in the following form:

$$\nabla \cdot \vec{u} = 0 \tag{2.1}$$

$$\frac{\partial \rho \vec{u}}{\partial t} + (\vec{u} \cdot \nabla)\vec{u} = -\nabla p_d + \mu \nabla^2 \vec{u} - \rho \epsilon g \beta (T - T_0)\hat{j} - S\vec{u} \tag{2.2}$$

$$\frac{\partial \rho h}{\partial t} + \nabla \cdot (\rho \vec{u} C_{pl} T) = \nabla \cdot (k \nabla T) \tag{2.3}$$

where $\vec{u}$ is the seepage velocity (or Darcy velocity), which is defined as the the average fluid velocity over a representative volume that may contain both liquid and solid phases [13]. Enthalpy h includes both sensible and latent components. The source term $-S\vec{u}$ is introduced into the momentum equation to account for the presence of solid in the control volumes. Its final form depends on the porosity ϵ (or liquid fraction), as explained in [6, 10]. There is a slight difference between momentum equation (2.2) and the presented in [6] in the Boussinesq source term (buoyancy force): here it is multiplied by the porosity, due to the fact that only the weight of the liquid phase should be considered in this term.

To solve these equations, it is necessary to define a relation between enthalpy and temperature of the PCM. Depending on the type of PCM studied, the change of phase can be produced either at a fixed temperature or in a temperature interval. A pure substance typically changes of phase at a fixed temperature, while a PCM consisting of a mixture of substances will undergo a temperature variations during the phase change. Following equations define the enthalpy–temperature relations for constant and variable phase change temperature cases.

- Constant phase change temperature:

$$h - h_{ref} = C_p(T - T_{ref}), \qquad T < T_{sl} \tag{2.4}$$

$$h - h_{ref} = C_p(T - T_{ref}) + L, \qquad T > T_{sl} \tag{2.5}$$

$$\begin{aligned} h - h_{ref} &= (1 - f)h_{sol} + f h_{liq} - h_{ref} \\ &= C_p(T_{sl} - T_{ref}) + fL, \qquad T = T_{sl} \end{aligned} \tag{2.6}$$

  with:

$$f = \frac{m_{liq}}{m_{liq} + m_{sol}} = \frac{h_{int} - h_{sol}}{h_{liq} - h_{sol}} \tag{2.7}$$

  where f is the liquid fraction, whose values range from 0 (pure solid) to 1 (pure liquid). h_{ref} and T_{ref} are a reference enthalpy and a reference temperature, respectively; T_{sl} indicates the phase change temperature; h_{sol} and h_{liq} indicate the specific enthalpies of the solid and liquid phases present in the same control volume (where the phase change is occurring).

- Variable phase change temperature:

$$h - h_{ref} = C_p(T - T_{ref}), \qquad T < T_s \tag{2.8}$$
$$h - h_{ref} = C_p(T - T_{ref}) + L, \qquad T > T_l \tag{2.9}$$
$$\begin{aligned} h - h_{ref} &= (1-f)h_{sol} + fh_{liq} - h_{ref} \\ &= C_p(T - T_{ref}) + fL, \qquad T_s < T < T_l \end{aligned} \tag{2.10}$$

  with:

$$f = \frac{T - T_s}{T_l - T_s} \tag{2.11}$$

  where T_s and T_l indicate solidus and liquidus temperatures, respectively. Here, there is a unique value of h for each value of T. The $f - T$ relation defined by Eq. (2.11) results in a linear $h - T$ curve in the phase change. This is just an approximation, since actually, the latter normally have a non–linear shape, which depend on the material.

Due to the assumption of constant density and equal between liquid and solid phases, mass liquid fraction f and volume liquid fraction (or porosity) ϵ are the same. Therefore, from here on ϵ will be used either as porosity or liquid fraction.

A fixed grid is used for the entire domain (including liquid, solid and interface), where the liquid fraction determines the state of the substance in each control volume. Liquid fraction with values between 0 and 1 indicates the presence of both phases in the same mesh node. These nodes are called "interface" nodes.

2.2.1 Nondimensionalization of the equations

To minimize the number of parameters on which the problem depends, nondimensionalization of the equations is carried out.

If D is a characteristic length and T_1 and T_0 characteristic temperatures of the problem:

$$\vec{r} = (x, y, z) \quad \Longrightarrow \quad \vec{r^*} = (x^*, y^*, z^*) \quad \text{(dimensionless position vector)}$$
$$\vec{u} = (u, v, w) \quad \Longrightarrow \quad \vec{u^*} = (u^*, v^*, w^*) \quad \text{(dimensionless velocity)}$$

and:
$\vec{r^*} = \frac{\vec{r}}{D}; \qquad t^* = \frac{t\alpha}{D^2}; \qquad \phi = \frac{T - T_0}{T_1 - T_0}; \qquad h^* = \frac{h}{C_p(T_1 - T_0)}$

then:

$\vec{u^*} = \frac{\vec{u}D}{\alpha}$; $\quad p_d^* = \frac{p_d D^2}{\rho\alpha^2}$; $\quad \nabla^* = D\nabla$

resulting in the following set of equations:

$$\nabla^* \cdot \vec{u^*} = 0 \tag{2.12}$$

$$\frac{\partial \vec{u^*}}{\partial t^*} + (\vec{u^*} \cdot \nabla^*)\vec{u^*} = -\nabla^* p_d^* + Pr(\nabla^*)^2 \vec{u^*} - RaPr\phi\hat{j} - S^*\vec{u^*} \tag{2.13}$$

$$\frac{\partial h^*}{\partial t^*} + \nabla^* \cdot (\vec{u^*}\phi) = \nabla^* \cdot (\nabla^* \phi) \tag{2.14}$$

where: $Pr = \frac{\mu}{\rho\alpha}$; $Ra = \frac{\rho g \beta D^3 (T_1 - T_0)}{\mu\alpha}$; $S^* = \frac{D^2}{\rho\alpha} S$

Nondimensionalizing enthalpy-temperature relations (2.4) to (2.6), assuming that T_{ref} in the referred equations is the same T_0 considered here as a characteristic temperature of the problem, they remain:

$$h^* = \phi, \qquad \phi < \phi_{sl} \tag{2.15}$$

$$h^* = \phi_{sl} + \frac{\epsilon}{Ste}, \qquad \phi = \phi_{sl} \tag{2.16}$$

$$h^* = \phi + Ste^{-1}, \qquad \phi > \phi_{sl} \tag{2.17}$$

where:

$$Ste = \frac{C_p(T_1 - T_0)}{L}$$

is the Stefan number, where either T_1 or T_0 are taken as the phase change temperature.

Therefore, the parameters of the problem are reduced to: Pr, Ra, Ste, S^*, besides the ones that could arise from nondimensionalizing the boundary conditions.

2.3 Numerical procedure

Governing equations ((2.1) to (2.3), or (2.12) to (2.14) in dimensionless form) are solved numerically, since only some very simplified cases can be solved analytically. An added difficulty of the phase change processes is the presence of a solid-liquid interface —which is a moving boundary— whose position has to be determined; this being a crucial part of the problem.

The adoption of the fixed grid enthalpy-porosity method simplifies considerably the problem of placing the solid-liquid interface, as it is determined by the volume fraction ϵ. The control volumes or nodes of the mesh that have a value of ϵ between 0 and 1 contain part of the interface. This procedure has the advantage of not having to solve more equations to find the interface and that the mesh does not have to be modified to follow the interface as in the interface tracking methods.

In cases where the PCM changes of phase at a fixed temperature, it has the disadvantage of not being able of exactly determining the position of the interface (which should be of infinitesimal width), since its width is of at least one control volume. However, when the phase change occurrs at a temperature range (e.g. for a mixture of pure substances), this is an advantage, as the real "interface" is in fact a three-dimensional region called "mushy" region.

2.3.1 Time discretization

Convective and diffusive terms are treated explicitly. Here, a 2$^{\text{nd}}$ order Adams-Bashforth is adopted, although further analysis here is not dependent on the particular explicit time scheme used. Pressure gradient is treated fully implicitly.

Regarding the momentum source term $S\vec{u}$, coefficient S is positive and —as indicated in [6, 10, 11]— it depends on the liquid fraction of the control volume, tending to infinity as ϵ tends to zero. In the differential momentum equations, this makes the velocity near solid control volumes tend to zero. However, in the discretized equations, if an explicit time scheme is used, it results in an equation where the new velocity depends on the last velocity times Δt multiplied by a factor tending to infinity. Thus, the time step adopted to make the system stable would have to be infinitesimal. This can be more clearly seen by working with a simplified differential equation:

$$\frac{\partial u}{\partial t} = -Su \text{ where } S > 0$$

and watching what happens when $S \to \infty$. The solution of this equation is:

$$u(t) = u_0 e^{-S(t-t_0)} \text{ with } u(t_0) = u_0$$

It can be seen that:

$$S \to \infty \Longrightarrow u(t) \to 0 \quad \text{and} \quad u_0 > 0\ (<0) \quad \Longrightarrow \quad u(t) > 0\ (<0)\ \forall t$$

Discretizing the differential equation using an explicit 1$^{\text{st}}$ order Euler time scheme, it results in:

$$u^{n+1} = u^n - \Delta t S u^n$$

To keep the restriction of not crossing the zero limit, the time step Δt has to be limited:

$$u^n > 0 \Longrightarrow u^{n+1} > 0 \Longrightarrow u^n(1 - \Delta t S) > 0 \Longrightarrow \Delta t < \frac{1}{S}$$

Then,

$$S \to \infty \Longrightarrow \Delta t \to 0$$

Therefore, the explicit formulation for this source term is unstable. To overcome this problem, a fully implicit time scheme is adopted for discretizing the momentum source term $-S\vec{u}$.

From now on we assume that the equations are dimensionless and supress the * for simplicity. Time-discretizated governing equations result in:

$$\nabla \cdot \vec{u}^{n+1} = 0 \tag{2.18}$$

$$\frac{\vec{u}^{n+1} - \vec{u}^n}{\Delta t} = \frac{3}{2}R^n(\vec{u}) - \frac{1}{2}R^{n-1}(\vec{u}) - \nabla p_d^{n+1} + \vec{f}^{n+1} \tag{2.19}$$

$$\frac{h^{n+1} - h^n}{\Delta t} = \frac{3}{2}R^n(\phi) - \frac{1}{2}R^{n-1}(\phi) \tag{2.20}$$

where:

$$\vec{f}^{n+1} = -S\vec{u}^{n+1} + RaPr\phi^{n+1} \cdot \hat{j} \tag{2.21}$$

and R represents the sum of convective and diffusive terms.

Working with Eq. (2.19) and grouping terms with u^{n+1} result in:

$$\vec{u}^{n+1}(1 + \Delta t S) = \vec{u}^n + \Delta t \left[-\nabla p_d^{n+1} + \frac{3}{2}R^n(\vec{u}) - \frac{1}{2}R^{n-1}(\vec{u}) - RaPr\phi^{n+1}\hat{j} \right] \Longrightarrow$$

$$\vec{u}^{n+1} = \frac{\vec{u}^n + \Delta t \left[-\nabla p_d^{n+1} + \frac{3}{2}R^n(\vec{u}) - \frac{1}{2}R^{n-1}(\vec{u}) - RaPr\phi^{n+1}\hat{j} \right]}{1 + \Delta t S} \tag{2.22}$$

Then, if $S \to \infty$, i.e. the control volume is almost solid, $u^{n+1} \to 0$.

Decoupling of u^{n+1} and p_d^{n+1} is carried out applying divergence, imposing mass conservation (Eq. (2.18)) and rearranging terms:

$$\Delta t \nabla \cdot \left(\frac{\nabla p_d^{n+1}}{1 + \Delta t S} \right) = \nabla \cdot u^p \tag{2.23}$$

where:

$$u^p = \left\{ \frac{\vec{u}^n + \Delta t \left[\frac{3}{2} R^n(\vec{u}) - \frac{1}{2} R^{n-1}(\vec{u}) - RaPr\phi^{n+1}\hat{j} \right]}{1 + \Delta t S} \right\} \tag{2.24}$$

is a pseudo-predictor velocity, and thus:

$$u^{n+1} = u^p - \Delta t \left(\frac{\nabla p_d^{n+1}}{1 + \Delta t S} \right) \tag{2.25}$$

from where the new velocity field (u^{n+1}) is calculated.

Regarding the energy balance, it should be noted that due to the explicit time scheme adopted, there is no need of an iteration step for calculating the liquid fraction of each control volume. It is just determined by the value of h^{n+1}, which is obtained directly from the energy equation (2.20). This iteration step is indeed needed when an implicit scheme is adopted, such as in [6, 10–12] and several others.

2.3.2 Space discretization

The entire domain is discretized using a fixed mesh. The formulation presented herein correspond to unstructured meshes and collocated schemes, as used in the CFD computer code TermoFluids [14].

In all cases, Finite Volume Method (FVM) is used for the spatial discretization of the equations. This method consists in integrating the governing differential equations over discrete control volumes.

Diffusive term

The diffusive term of the momentum equation —disregarding the multiplying coefficient (Pr or μ)— integrated over a finite control volume, becomes:

$$\frac{1}{V} \int_V \nabla^2 \vec{u}\, dV = \frac{1}{V} \int_A \nabla \vec{u} \cdot \hat{n}\, dA \approx \frac{1}{V} \sum_f (\nabla \vec{u} \cdot \hat{n})_f A_f \tag{2.26}$$

where the divergence theorem has been used in the first equality. Sub-index f indicates that the sum is performed over the surfaces of the control volume.

Using the notation indicated in figure 2.1, the discretized diffusive term is expressed here as [15]:

$$\frac{1}{V} \sum_f (\nabla \vec{u} \cdot \hat{n})_f A_f \approx \frac{1}{V} \sum_f \left(\frac{\vec{u}_F - \vec{u}_P}{\overrightarrow{d_{PF}} \cdot \hat{n}} A \right)_f \tag{2.27}$$

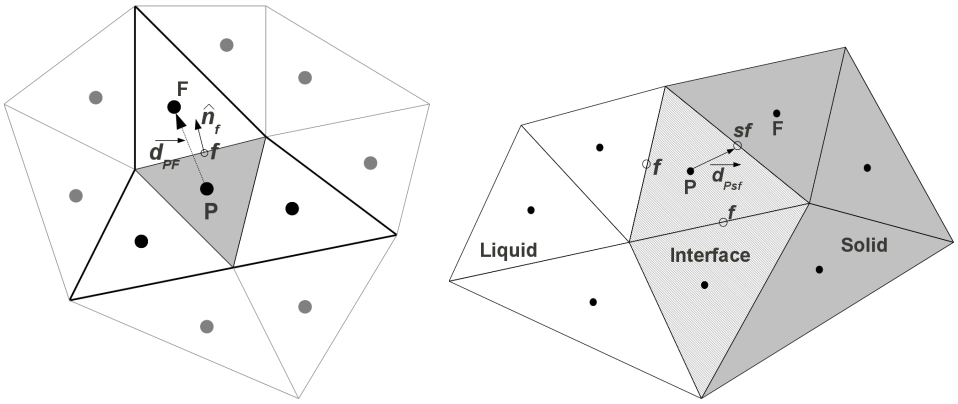

(a) Away from solid nodes.

(b) Near solid nodes. Diferent phases are indicated by the area filling.

Figure 2.1: Notation used for the position of the nodes in an unstructured mesh. Letter P indicates the node being calculated, F a neighboring node, f the face shared by nodes P and F, $\hat{n}_f$ the vector normal to face f pointing outwards P, and $\vec{d_{PF}}$ the vector going from P to F. If node F contains solid, then the face connecting nodes P and F is denoted sf and the distance from P to this face $\vec{d_{Psf}}$.

where sub-indices P and F indicate the node where the integration is being performed and the neighbor cell node corresponding to face f, respectively.

Convective term

The application of the FVM for treating the convective term gives:

$$\frac{1}{V}\int_V \nabla\cdot(\vec{u}\vec{u})\,dV = \frac{1}{V}\int_A \vec{u}(\vec{u}\cdot\hat{n})\,dA \approx \frac{1}{V}\sum_f \left[\vec{u}(\vec{u}\cdot\hat{n})\right]_f A_f \tag{2.28}$$

where —for convenience— the conservative form of the momentum equation has been used. Here again, divergence theorem has been used to derive the first equality.

Using notation from figure 2.1 and adopting a symmetry-preserving scheme [16], the above equation becomes:

$$\frac{1}{V}\sum_f \left[\vec{u}(\vec{u}\cdot\hat{n})\right]_f A_f \approx \frac{1}{V}\sum_f \left(\frac{\vec{u}_P+\vec{u}_F}{2}\right)\dot{m}_f \tag{2.29}$$

where $\dot{m}_f$ is the flux through face f, which is calculated from the velocity field u and corrected in order to satisfy mass conservation [15], similarly as in [17].

In liquid-containing cells neighboring other solid cells (as in fig. 2.1(b)) the flux ($\dot{m}_f$) through solid faces is explicitly set to zero in order not to have artifical "leackage" through the solid, and convection through these faces is completely eliminated.

For the convective term in the energy equation (2.3) an UPWIND scheme [18] has been used due to boundedness reasons.

Discussion about the form of the energy equation

In [6,10] the differential equation for the energy balance in the phase changing process is presented as[a]:

$$\frac{\partial \rho h}{\partial t} + \nabla \cdot (\rho \vec{u} h) = \nabla \cdot (k \nabla T) \tag{2.30}$$

This equation has a slight difference compared to Eq. (2.3): the advection-convection term. The transported property in Eq. (2.30) is the total enthalpy (including latent), while in Eq. (2.3) only the sensible enthalpy of the liquid is considered to be transported by the flow. Actually, Eq. (2.3) results from assuming constant specific heat in the liquid phase and from the incompressibility condition (Eq. (2.1)). In a more general formulation the total liquid enthalpy should be used in the convective term. If the incompressibility condition were not applied, the latent heat of the liquid phase should be included. However, this remains being different from advecting the enthalpy h (as defined here), because the latter is a mean value of the enthalpies of the liquid and solid phases present in the control volume.

In pure solid and liquid phases there is no difference at taking any of both energy equations. This is because in the solid phase there is no enthalpy transport and in the liquid phase only differences in sensible enthalpy are needed to be accounted for, as only one phase is involved. However, in the regions (or control volumes) where both liquid and solid phases are present (i.e. interface or "mushy zone" nodes), the volume integration of both formulations give different results.

As the interface will not be of infinitesimal width due to the adopted fixed-grid model (even in the case of phase change at a fixed temperature), there will be control volumes that will contain the interface and where the fluid part will have a velocity different from zero. Furthermore, mass and energy will be entering and leaving these "interface" control volumes, and these interactions will be produced between liquid and interface nodes and also between different interface nodes (see figure 2.2). Thus,

[a] Actually, in those references, h represents only the sensible enthalpy and an extra source term is included to account for the latent enthalpy, which is represented by ΔH.

discretized momentum and energy equations will have non-zero advective terms in these control volumes (see section 2.3.1 below).

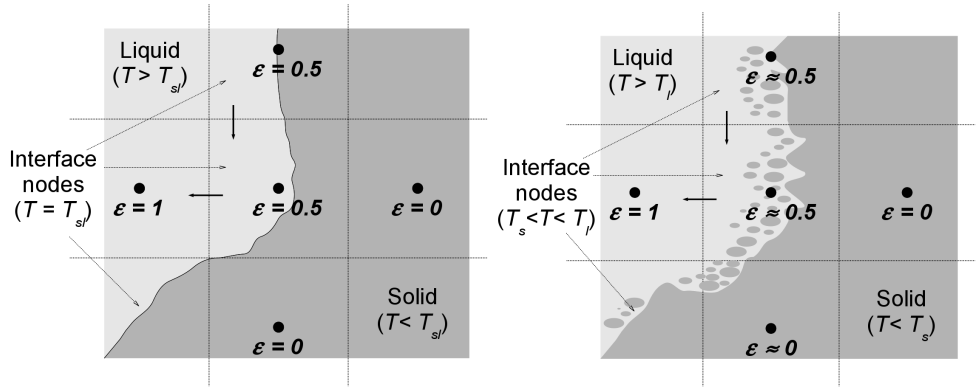

(a) Sharp interface (b) Mushy zone

Figure 2.2: Schemes showing control volumes containing both solid and liquid phases. Arrows at the control volume faces indicate liquid flowing to and from the control volume.

Regarding the energy equation, if we chose to evaluate the convective term taking the total specific enthalpy h (as defined by Eqs. (2.4) to (2.10)) as the transported property, then we would be transporting a variable that depends on the liquid fraction of the involved nodes (see Eq. (2.5)); i.e. we would be transporting a "mean value" of the enthalpy of the solid and liquid phases of the involved control volumes. This is not right, since only the liquid phase is transported from one node to the other (assuming that the solid is fixed with respect to the grid). Therefore, only the enthalpy of the liquid phase is advected. Due to the assumption of equal densities between solid and liquid phases (see section 2.2), there is no mass accumulation nor decrease in any cell, and mass fluxes entering any cell must equal the mass fluxes leaving it. With this in mind, it can be observed that the balance of transport of energy into any cell by advection equals the difference between the energy contents of the entering and leaving mass fluxes, resulting in a balance of sensible enthalpies of the referred fluxes (as the latent enthalpies get cancelled out). The effect of this discrepancy or "error" is studied next.

Convective term of equation (2.3) (using h_{liq} as the enthalpy of the liquid phase), integrated in an interface control volume, can be expressed as:

$$\int_V \nabla \cdot (\rho \vec{u} h_{liq}) \approx \sum_f \dot{m}_f (h_{liq})_f \tag{2.31}$$

while the convective term of Eq. (2.30) results in:

$$\begin{aligned}\int_V \nabla \cdot (\rho \vec{u} h) \approx \sum_f \dot{m}_f h_f &= \sum_f \dot{m}_f \left[(1-\epsilon)h_{sol} + \epsilon h_{liq}\right]_f \\ &= \sum_f \dot{m}_f \left[(h_{liq} - (1-\epsilon)(h_{liq} - h_{sol})\right]_f \\ &= \sum_f \dot{m}_f (h_{liq})_f - \sum_f \dot{m}_f \left[(1-\epsilon)(h_{liq} - h_{sol})\right]_f \end{aligned} \tag{2.32}$$

The first term of the right side of Eq. (2.32) is equal to the right side of Eq. (2.31); hence, the difference between both equations results in:

$$C_{liquid} - C_{total} = \sum_f \dot{m}_f \left[(1-\epsilon)(h_{liq} - h_{sol})\right]_f \tag{2.33}$$

where C_{liquid} and C_{total} represent the convective terms considering the liquid enthalpy and the total enthalpy, respectively.

To clarify the effects of this difference, above equations will be expressed for the center node of figure 2.2. The mentioned node has a liquid fraction (ϵ) of 0.5; receives a mass flux from the upper node, which also has a liquid fraction of 0.5; and has an outflow towards the left node, which has a liquid fraction of 1 (pure liquid).

Taking into consideration that due to the mass balance, the mass flux going through the upper face has to be equal to the one going through the left face ($\dot{m}_{left} = \dot{m}_{up}$); then, the convection term —using Eq. (2.31)— results in:

$$\begin{aligned} C_{liquid} &= \dot{m}_f (h_{liq,left} - h_{liq,up}) = \dot{m}_f C_p (T_{f,left} - T_{f,up}) \\ &= \dot{m}_f C_p \frac{T_L - T_U}{2} \end{aligned} \tag{2.34}$$

where sub-indexes L and U indicate the values of the left and upper nodes, respectively. Now, the difference between both approaches results in:

$$\begin{aligned} C_{liquid} - C_{total} &= \dot{m}_f \frac{(1-\epsilon)_L (h_{liq} - h_{sol})_L + (1-\epsilon)_P (h_{liq} - h_{sol})_P}{2} \\ &\quad - \dot{m}_f \frac{(1-\epsilon)_U (h_{liq} - h_{sol})_U + (1-\epsilon)_P (h_{liq} - h_{sol})_P}{2} \\ &= -\dot{m}_f \frac{(1-\epsilon)_U (h_{liq} - h_{sol})_U}{2} = -\dot{m}_f \frac{L}{4} \end{aligned} \tag{2.35}$$

where the facts that the liquid fraction of the left node is equal to 1 and that the difference between the enthalpies of the liquid and solid portions of node U is equal

to the latent heat of fusion, L (according to the model adopted here, Eq. (2.6) or (2.10)), have been considered.

Now, comparing Eqs. (2.34) and (2.35), it can be observed that:

$$\left|\frac{C_{liquid} - C_{total}}{C_{liquid}}\right| = \left|\frac{L}{2C_p(T_L - T_U)}\right|$$

Assuming that the temperature difference between left and upper nodes is not high (which is reasonable with a normal grid density) or that the Stefan number is sensibly smaller than 1 (very usual in phase change problems, where the latent heat of fusion is high compared to the maximum possible sensible enthalpy difference), then:

$$\left|C_p(T_L - T_U)\right| \ll L \Longrightarrow \left|C_{liquid} - C_{total}\right| \gg \left|C_{liquid}\right|$$

Therefore, for this particular node, the "error"in the expression of the discrete convective term is much higher than the convective term itself. This can cause high unphysical fluctuations in the enthalpy and liquid fractions of the referred node, if the mass flux $\dot{m}_f$ is not so small to make the convective term vanish.

Numerical tests have shown notable differences between the adoption of total or liquid sensible enthalpy in coarse grids, although they tend to vanish as the grid is refined.

It should be noted that these differences are produced by the discretization of the equations and by the fact that in one control volume both solid and liquid phases are present. This does not mean that Eq. (2.30) is wrong; it is a differential equation and so can only be strictly applied to infinitesimally small volumes. Thus, the error is introduced at the volume integration stage.

Voller et al. [6] state that only in the fixed temperature phase change case —where the interface is of infinitesimal width— the advection of ΔH (latent heat of fusion weighted by the porosity in the control volume) vanishes, and that it should be accounted for in a mushy region case. The argument presented in this section results in a different conclusion: even in a mushy region case, since only the liquid phase is advected, ΔH should not be included in the convection term.

However, the case of phase change of a mixture of substances (in a temperature range instead of a fixed temperature) is not so simple if the different properties of the different substances are considered. Probably, in these cases the difference of liquid enthalpy at different temperatures —inside the phase change temperature range—cannot be considered just as a difference in sensible enthalpy, since the liquid phase consists of different fractions of each substance at each temperature. In this case, a more detailed expression of the enthalpy-temperature relations should be adopted, and Eq. (2.3) should be written with the total liquid enthalpy in its convective term (as in Eq. (2.31)).

2.3.3 Pressure equation

Here, the pressure-velocity decoupling procedure for the equations corresponding to the liquid-containing cell nodes is detailed, where a special treatment of the solid boundary nodes (face nodes) is indicated. The matrix coefficients of the resulting linear system, as well as the vector of independent terms, are presented.

The integration of Eq. (2.23) results in:

$$\frac{1}{V}\int_V \Delta t\,\nabla\cdot\left(\frac{\nabla p_d^{n+1}}{1+\Delta t S}\right)\,dV = \frac{1}{V}\int_V \nabla\cdot(\vec{up})\,dV \tag{2.36}$$

Following the same line of reasoning that in previous sections, Eq. (2.36) becomes:

$$\frac{\Delta t}{V}\sum_f \left(\frac{\nabla p_d^{n+1}}{1+\Delta t S}\right)_f \cdot \hat{n}_f A_f = \frac{1}{V}\sum_f \left(\vec{up}\cdot\hat{n}\right)_f A_f \tag{2.37}$$

which defines a system of equations of pressure which needs to be solved using some linear solver. A further simplification of this system is carried out near solid boundaries.

At solid boundaries, the following Neumann condition is applied [19]:

$$(\nabla p_d\cdot\hat{n})_{sf} = \left[\left(Pr\nabla^2\vec{u} - RaPr\phi\hat{j}\right)\cdot\hat{n}\right]_{sf} \tag{2.38}$$

which is derived from momentum equation (Eq. (2.2)) and the velocity boundary condition:

$$\vec{u}_{sf} = 0 \Longrightarrow (\vec{u}\cdot\hat{n})_{sf} = 0 \tag{2.39}$$

In semi–discrete form, integrated in a surface element, this boundary condition for pressure results in:

$$\nabla p_d^{n+1}{}_{sf}\cdot\hat{n}_{sf} = \left[\frac{3}{2}R^n(\vec{u}) - \frac{1}{2}R^{n-1}(\vec{u}) - RaPr\phi^{n+1}\hat{j}\right]_{sf}\cdot\hat{n}_{sf}$$

where R contains not only the diffusive term appearing in Eq. (2.38) but also the convective term. This is not a problem, since convection through a solid boundary is zero (Eq. (2.39)).

Noting that u^n is also zero, then:

$$\Delta t\nabla p_d^{n+1}\cdot\hat{n}_{sf} = \left\{u^n + \Delta t\left[\frac{3}{2}R^n(\vec{u}) - \frac{1}{2}R^{n-1}(\vec{u}) - RaPr\phi^{n+1}\hat{j}\right]\right\}\cdot\hat{n}_{sf}$$

hence, dividing by $1 + \Delta tS$ and using Eq. (2.24):

$$\left(\frac{\Delta t \nabla p_d^{n+1}}{1 + \Delta tS} \cdot \hat{n}\right)_{sf} = \left(\vec{u^p} \cdot \hat{n}\right)_{sf} \tag{2.40}$$

Now, working with Eq. (2.36) for a boundary control volume (a cell with a face belonging to a solid boundary) and separating the solid face from the sums at both sides of the equation:

$$\Delta t \left[\sum_{f \neq sf} \left(\frac{\nabla p_d^{n+1}}{1 + \Delta tS} \cdot \hat{n}A\right)_f + \left(\frac{\nabla p_d^{n+1}}{1 + \Delta tS} \cdot \hat{n}A\right)_{sf}\right] = \sum_{f \neq sf} \left(\vec{u^p} \cdot \hat{n}A\right)_f + \left(\vec{u^p} \cdot \hat{n}A\right)_{sf} \tag{2.41}$$

Hence, combining Eq. (2.41) and (2.40) it results in:

$$\Delta t \left[\sum_{f \neq sf} \left(\frac{\nabla p_d^{n+1}}{1 + \Delta tS} \cdot \hat{n}A\right)_f\right] = \sum_{f \neq sf} \left(\vec{u^p} \cdot \hat{n}A\right)_f \tag{2.42}$$

and inner nodes adjacent to the solid boundaries are "decoupled" from solid boundary pressure nodes; i.e. instead of solving the system of pressure equations defined by Eq. (2.37), we solve the system defined by Eq. (2.42), where solid boundary pressure nodes are not included as variables neither as equations.

The term at the left side of Eq. (2.42) is very similar to the diffusive term and it is discretized similarly:

$$\sum_{f \neq sf} \left(\frac{\nabla p}{1 + \Delta tS}\right)_f \cdot \hat{n}_f A_f \approx \sum_{f \neq sf} \left[\left(\frac{p_{dF} - p_{dP}}{\overrightarrow{d_{PF}} \cdot \hat{n}}\right) \left(\frac{1}{1 + \Delta tS_P} + \frac{1}{1 + \Delta tS_F}\right) \frac{A}{2}\right]_f$$

while the term at the right side of Eq. (2.37) is very similar to the discretized mass balance equation:

$$\sum_{f \neq sf} \left(\vec{u^p} \cdot \hat{n}A\right)_f \approx \sum_{f \neq sf} \left(\frac{\vec{u^p}_P + \vec{u^p}_F}{2} \cdot \hat{n}A\right)_f \tag{2.43}$$

Therefore, a system of equations in pressure is obtained, with the following coefficients:

$$a_{\mathrm{P}} \tilde{p_d}_{\mathrm{P}}^{n+1} + \sum_{f \neq sf} a_{\mathrm{F}_f} \tilde{p_d}_{\mathrm{F}_f}^{n+1} = b_{\mathrm{P}} \tag{2.44}$$

where $\tilde{p_d} = \Delta t p_d$ and:

$$a_{\mathtt{F}_f} = \frac{A_f \left(\theta_{F_f} + \theta_P\right)}{2\overrightarrow{d_{PF_f}} \cdot \hat{n}}; \qquad a_{\mathtt{P}} = \sum_{f \neq sf} -a_{\mathtt{F}_f}$$

$$b_{\mathtt{P}} = \sum_{f \neq sf} \left(\frac{\vec{u^p}_P + \vec{u^p}_F}{2} \cdot \hat{n} A \right)_f$$

with:

$$\theta = \frac{1}{1 + \Delta t S}$$

where sub-index $\mathtt{F}_f$ (or F_f) indicate a value corresponding to a neighbor node of node P connected through face f and d_{PF_f} is the distance between both nodes.

The resulting symmetric system of equations has to be solved using some linear "solver".

Numerical implementation and resolution of the pressure system of equations including solid nodes

As the tensional state of the solid phase is not evaluated, the system of equations defined by Eq. (2.42) should only be written —a priori— for the nodes containing some liquid, i.e. those whose liquid fraction is higher than zero. However, if this approach were adopted, the system of equations would be of variable size, since —for example— as solid nodes change to interface or liquid nodes, the number of variables and equations would increase. This would mean that the linear solver used should be "updated" every time a node changes phase, which is not computationally simple.

Instead, a different approach is adopted. The size of the linear system of equations is maintained constant and equal to the maximum size (the total number of mesh nodes minus the nodes placed in solid boundaries) and the coefficients $a_{\mathtt{P}}$ and $a_{\mathtt{F}}$ are modified. Eq. (2.42) indicates that the pressure of liquid-containing cell nodes, located next to solid boundaries, is "decoupled" from the pressure at these boundary surfaces; therefore, between two cell nodes —one containing at least some liquid and the other one containing only solid— the same condition is applied. Hence, the coefficient $a_{\mathtt{F}}$ which relates both pressure nodes is set to zero.

For the solid nodes, an arbitrary form of the pressure equation can be defined, as its result is meaningless. Thus, in this work, trivial equations of the form:

$$a_{\mathtt{P}} p_{d\mathtt{P}} = b_{\mathtt{P}} \tag{2.45}$$

are adopted. For b_P any value can be chosen (e.g. zero) and a_P can take the value of 1 or any other, different from zero.

This way, a symmetric linear system of equations is obtained, of constant size, whose coefficients change at every time iteration. This system can be seen as two independent systems: one symmetric system consisting in the pseudo-Poisson equations (Eq. (2.42)) corresponding to all the liquid-contaning nodes; and another —trivial system— consisting in Eq. (2.45) corresponding to all the solid nodes. Both systems are independent from one another, since the coefficients "connecting" both groups of nodes are all zero.

Due to the changing nature of the system matrix, an iterative solver is used for its resolution. In this work, a Conjugate Gradient (CG) solver using a diagonal preconditioner, has been chosen.

An issue that has to be accounted for in the resolution of the pressure system of equations is the fact that Eq. (2.42) define a system with one degree of freedom, i.e. one can choose the value of the pressure in one of the liquid-containing nodes arbitrarily. Therefore, this system is not definite, and this is a problem for some solvers, such as CG. Thus, before each run of the pressure solver, a modification is made to the system of equations to transform it into a definite one: one of the diagonal coefficients a_P is modified multiplying it by some factor, e.g. 1.1. This way, the system of equations is transformed into definite without modifying its symmetry, which is another characteristic needed for the CG solver to run.

This coefficient modification has to be performed over an equation corresponding to a liquid-containing node. Therefore, at each time iteration, a check has to be carried out in order to assess that the equation being modified does not belong to a solid node, and if it does, another node (containing liquid) has to be chosen.

2.3.4 Different expressions of the momentum source term factor (S)

The final form of the source term coefficient (S) depends on the approximation adopted for the behavior of the flow in the "mushy zone" (where mixed solid and liquid states are present). In [6, 10], the expression for S was obtained assuming that the "mushy zone" should be treated as a porous material. However, in the case of constant phase change temperature, the solid-liquid interface should be of infinitesimal width (although it cannot be thinner than the width of one control volume in our simulations); therefore, the formulation used for the source term is not very important in a physical sense, as long as it manages to bring the velocity to zero in mostly solid control volumes and to vanish if the volume contains pure liquid (as already noticed by [10]).

The expression of S should depend on ϵ. A liquid fraction of zero ($\epsilon = 0$), means that the control volume is completely solid and therefore, the source term has to tend

to infinity in order to make the velocity tend to zero. On the other hand, a liquid fraction of 1 ($\epsilon = 1$) represents a control volume that is pure liquid; hence, S has to be zero and the momentum source term (due to presence of solid) vanishes.

References [6,10] propose an expression of S which intends to mimic the behaviour of fluid flowing through a porous medium. The resulting expression is the following:

$$S = \frac{C(1-\epsilon)^2}{\epsilon^3 + q} \tag{2.46}$$

where C is an arbitrary (big) constant and q is a very small value included to avoid division by zero.

This expression is mainly intended to be used when a "mushy region" is developed (e.g. when the phase change is produced in a temperature range), and the flow in this zone has to be modeled. According to [6], Eq. (2.46) forces the fluid in the mushy region to follow the Carman-Kozeny law, which has been experimentally validated for flow in a dendritic region.

However, as mentioned above, when the substance changes of phase at a fixed temperature there is no physical meaning for the momentum source term introduced here, as there is no mushy region. Since Eq. (2.46) is computationally costly (includes two power operations and one division), other easier-to-compute expressions can be used.

For example, reference [10] also proposes a linear expression:

$$S = C(1-\epsilon) \tag{2.47}$$

with C being, again, a very high value. It can be observed that in this case, when $\epsilon = 0$, $S = C$. If C is not chosen to be big enough, it is possible that the flux is not damped enough.

Another expression is used in this work, which intends to keep the property of tending to infinity with ϵ:

$$S = C\left(\frac{1}{\epsilon} - 1\right) \tag{2.48}$$

Observing Eq. (2.22), it is clear that the "damping effect" is produced by the factor $\frac{1}{1+\Delta t S}$. This factor is always between 0 and 1; in the pure liquid case it is exactly 1 and no damping is produced, while if some solid phase is present it lowers depending on the liquid fraction. In the pure solid case ($\epsilon = 0$) this factor should be equal to zero.

Figure 2.3 show curves of $\frac{1}{1+\Delta t S}$ as a function of ϵ, taking $\Delta t = 1 \times 10^{-3}$ and $C = 1 \times 10^2, 1 \times 10^3$and 1×10^4. It can be observed (fig. 2.3(a)) that a poor choice of parameter C can lead, for Eq. (2.47), to not producing enough damping effect at ϵ near zero. Eq. (2.46) is the least affected by the change in C. Expression defined by Eq. (2.48), introduced in this work, shows a better performance than Eq. (2.47) in the

sense of its damping effect with low ϵ although it is more affected by the variation of C than Eq. (2.46).

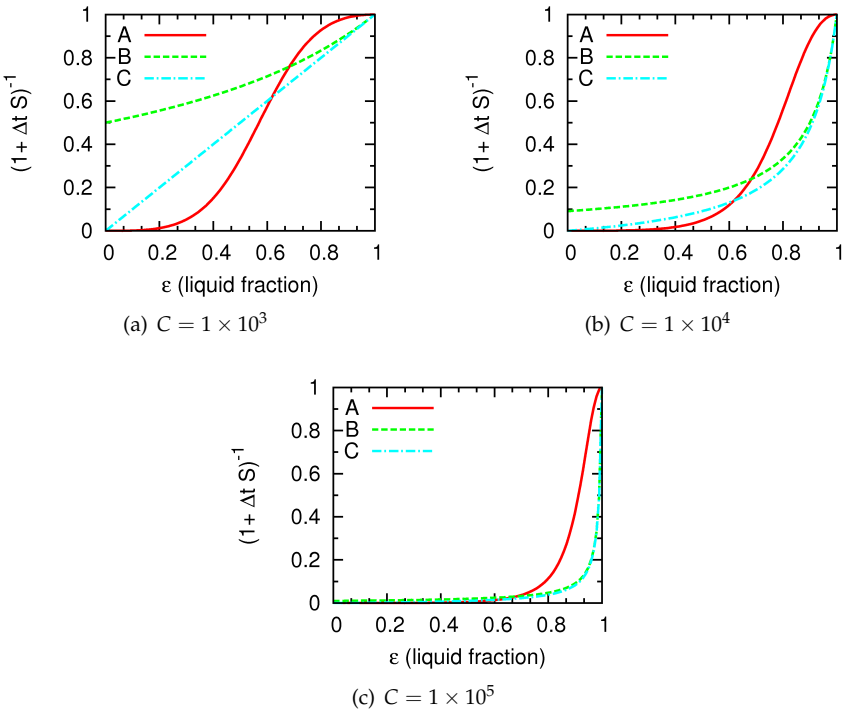

(a) $C = 1 \times 10^3$ (b) $C = 1 \times 10^4$

(c) $C = 1 \times 10^5$

Figure 2.3: Curves of $\frac{1}{1+\Delta t S}$ versus ϵ for different values of C, with $\Delta t = 1 \times 10^{-3}$. Curves A correspond to S evaluated using Eq. (2.46), while B and C correspond to Eqs. (2.47) and (2.48), respectively.

Therefore, it seems that Eq. (2.46) results in a smooth variation of the factor $\frac{1}{1+\Delta t S}$ for a wider range of values of C than Eqs. (2.47) and (2.48), which could be adopted in cases of fixed temperature phase change. Eq. (2.48) is safer than Eq. (2.47) in the sense of tending to zero for every choice of C, since when using Eq. (2.47) care should be taken at choosing a value of C which is high enough to make the factor $\frac{1}{1+\Delta t S}$ effectively tend to zero. Eqs. (2.47) and (2.48) could be used to save computing time in cases of fixed temperature phase change.

2.3.5 Algorithm overview

The above formulation of the governing equations is implemented in a computer code and solved according to the following (simplified) algorithm for each time step:

- Energy equation (Eq. (2.20)): new enthalpy, temperature and porosity fields are calculated
- Pseudo-predictor velocities u^p using previous velocity fields (Eq. (2.24))
- Pressure equation (Eq. (2.44)): calculation of the system coefficients: a_{P}, a_{F} and b_{P}
- Resolution of pressure equation using a linear solver (e.g. CG)
- New velocity field using predictor velocity and new pressure field (Eq. (2.25))

This is just an overview of the adopted algorithm; where pre and post-processes, as well as many details encompassed in each of the algorithm steps, are not indicated.

2.4 Numerical results

Numerical simulations of three different phase change problems have been performed. Results are compared against experimental and numerical results found in the bibliography.

2.4.1 Gallium melting

Firstly, a case of Gallium melting in a rectangular cavity [11,20,21] was simulated. The problem is 2D and consists of a rectangular cavity of aspect ratio $A_r = 0.5$ filled with Gallium in solid state. Top and bottom walls are adiabatic, while left and right walls are set to uniform temperatures. Initially, all the system is at a temperature slightly below the phase change. Suddenly, the left wall temperature is increased above the phase change and heat starts to enter the cavity, melting the Gallium. Natural convection is observed and the phase change interface starts to be deformed from its initial vertical-line shape.

The parameters of the problem are the following:

- Aspect ratio $A_r = 0.5$, $H(height) = 0.0445m$;
- $\rho = 6093\, kg\, m^{-3}$, $k = 32\, W\, m^{-1}\, K^{-1}$, $C_p = 381.5\, J\, kg^{-1}\, K^{-1}$;
- $Ra = 2.1E5$, $Pr = 0.0216$, $Ste = 0.0419$

- Initial temperature of 28.3°C, hot wall temperature of 38°Cand phase change temperature of 29.78°C.

Figures 2.4 and 2.5 show the interface position as well as temperature contours and fig. 2.6 shows a correlation between $NuRa^{-0.25}$ and dimensionless time τ as in [20]. Results obtained are very similar to previous numerical ones from [11] and very close to experimental ones, as it is shown in the above figures.

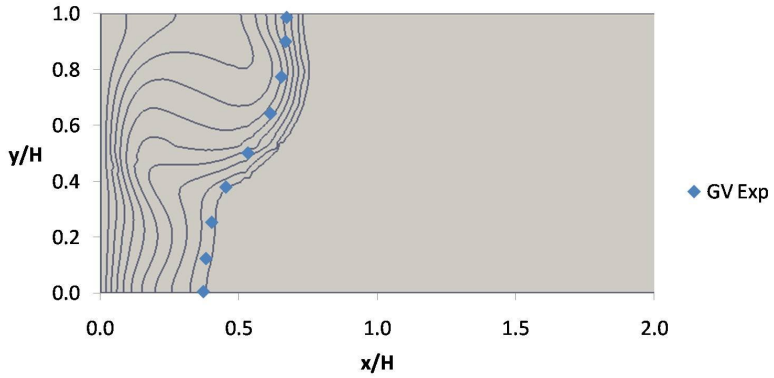

Figure 2.4: Temperature contours and solid-liquid interface position of the melting gallium in the rectangular cavity, at time t = 6 min. The dots indicate the location of the interface obtained experimentally by [20].

Results shown correspond to simulations using a 80x40 structured 2D grid. However, with this mesh, a true converged solution is not obtained. This is concluded by the fact that by further grid refinement, notable differences with the results obtained with the 80x40 grid — at the initial moments of the simulation— are observed. These differences consist in a multicellular behaviour of the fluid motion, not observed in the experimental results presented by [20]. This problem has been identified in previous works as [22] (although with another similar test case, also presented in [20]).

This aspect is taken into account in the next section, where the melting of pure tin is simulated using much finer meshes.

2.4.2 Melting of pure tin

This problem is very similar to the one of gallium melting and is based on the experimental work of Wolff and Viskanta [23]. A square cavity is filled with tin, initially at solid state at the phase change temperature. Suddenly, the left wall is heated to a uniform higher temperature and the tin starts to melt from the left to the

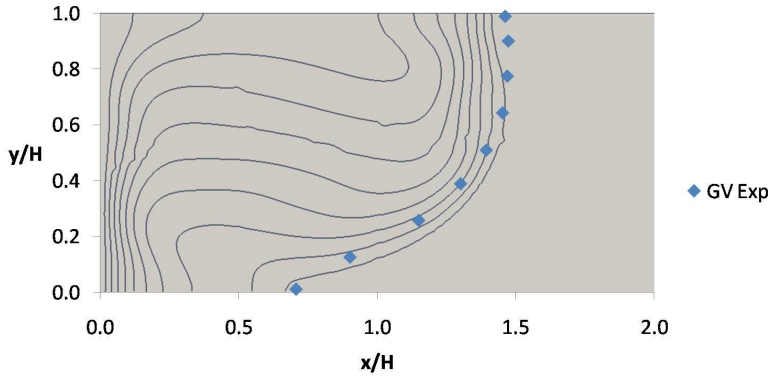

Figure 2.5: Temperature contours and solid-liquid interface position of the melting gallium in the rectangular cavity, at time t = 17 min. The dots indicate the location of the interface obtained experimentally by [20].

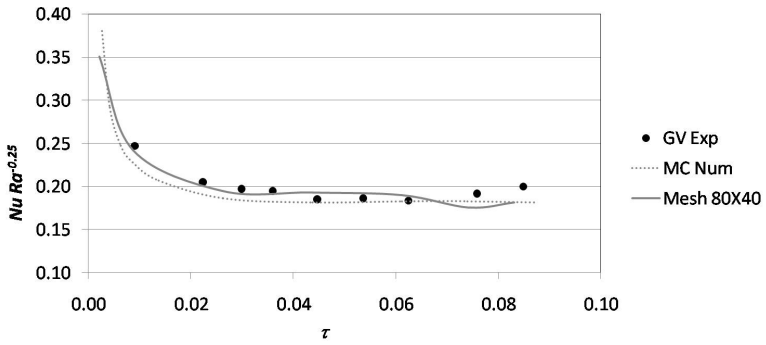

Figure 2.6: Evolution of $NuRa^{-0.25}$ with dimensionless time $\tau = FoSteA_\tau^2$ (as in [20]). GV Exp: experimental results from [20]. MC Num: Numerical results from [11].

right walls. Top and bottom walls are adiabatic, while the right wall stays at the phase change temperature.

As the solid temperature cannot rise above the phase change temperature and the right wall is maintained constant, the solid is isothermal at every moment. Taking advantage of this fact, the simulations are run only over a portion of the whole cavity, since the objective is not to simulate the entire melting process but only the first 1000 –2000 seconds.

The parameters of the problem —taken from [22]— are the following:

- Aspect ratio $A_r = 1$, $H(height) = 0.1m$;
- $\rho = 7500\, kg\, m^{-3}$, $k = 60\, W\, m^{-1}\, K^{-1}$, $C_p = 200\, J\, kg^{-1}\, K^{-1}$;
- $Ra = 2.25E5$, $Pr = 0.04$, $Ste = 0.01$
- Initial temperature of 505 K, hot wall temperature of 508 K and phase change temperature of 505 K.

Figure 2.7 show the results obtained after 200, 450 and 1000 seconds. Reference [22] presents several simulations of the problem using diverse numerical schemes (upwind, centered and hybrid) for mesh densities of 100x100, 200x200 and 400x400. Our results are very close the results obtained by [22] using a centered scheme, for all the mesh sizes.

However, as stated in [22], numerical solutions deviate considerably from experimental results obtained by [23], as in the latter, apparently there is no multicellular behaviour like in the former. They also observe that the numerical results obtained using coarser grids are closer to experimental than the grid-converged simulations. These observations are also valid for the gallium melting experiment performed by [20], which was used as a validation case in the previous section.

Evidently there is a problem, either with the mathematical model or with the experimental procedure not being able to meet the assumptions. An interesting approach to this problem has been carried out by [24], who state that the issue relies on the lack of modeling of the solid deformations. They include solid deformation modeling in their simulations and obtain results showing uni-cellular behaviour of the Gau-Viskanta experiment. However, quite coarse meshes are used in their simulations (the finest one being of 25 x 90 in the liquid phase) with results that are not grid-converged. Therefore, it would be interesting to perform further simulations with denser meshes in order to firmly conclude that solid deformation is the cause of the uni-cellular behaviour.

2.4.3 Spherical capsules filled with N-Octadecane

Another case study used to validate the CFD phase change model is the melting of N-octadecane encapsulated in a sphere, as in [12, 25]. A spherical capsule is filled with this material and taken to a temperature 1°C below the phase change. Suddenly, the capsule shell is heated and maintained at a constant temperature. Again, the phenomenon is assumed to be 2D. Parameters of the problem are:

- $D = 0.10166\, m$ (diameter of sphere);

(a) t = 200s

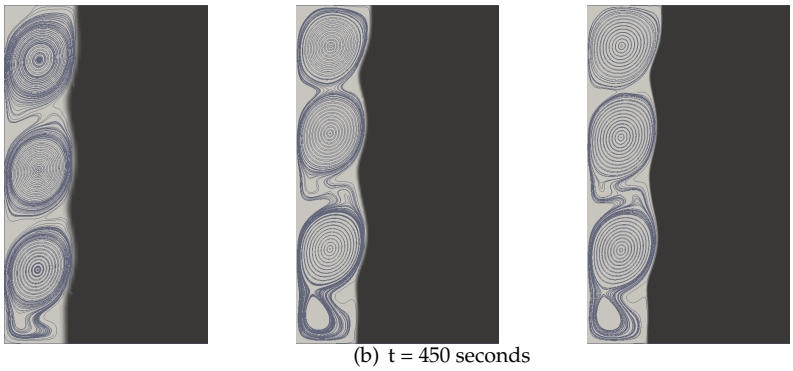

(b) t = 450 seconds

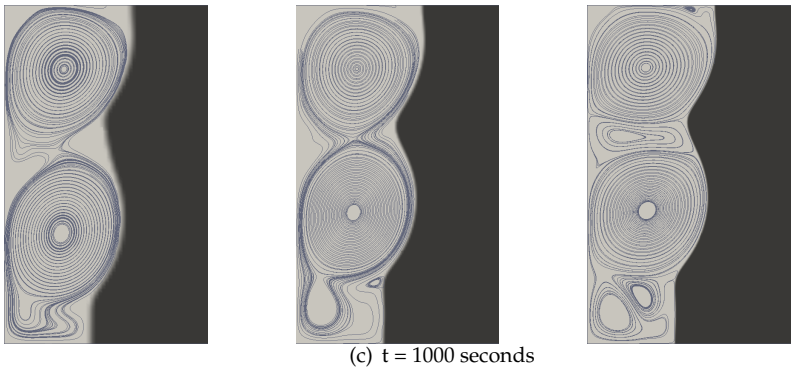

(c) t = 1000 seconds

Figure 2.7: Tin melting at different times using different grids: 100x100 (left column), 200x200 (center column) and 400x400 (right column). Clear region: liquid phase. Dark region: solid phase. Contours correspond to the streamlines. The images show portion of the total cavity of 0.06 m x 0.1 m.

- $\rho = 772\,kg\,m^{-3}$, $k = 0.1505\,W\,m^{-1}\,K^{-1}$, $C_p = 2330\,J\,kg^{-1}\,K^{-1}$;
- $Ra = 3.307E7$, $Pr = 59.76$, $Ste = 0.112913$
- Initial temperature of 27.2°C, and phase change temperature of 28.2°C.

The temperature boundary condition imposed in this work is convection between the thermal bath and the glass combined with thermal conduction thorugh the shell. Bath temperature is T = 40.0°C and the overall convection coefficient is 796 $W/m^{-1}K^{-1}$; which has been deduced from estimated values of glass width, glass thermal conductivity and convection coefficient of the thermal bath.

Fig. 2.8 shows two photographs of the experimental evolution of the phase change at different moments, extracted from [25] ; while fig. 2.9 shows some graphical results obtained by the present work. The mesh used in the simulations was designed to have similar quantity of nodes —between 7600 and 7700 cells— as the one used by [12] in their own numerical simulations. There is an agreement in the overall behavior of the system, although a faster melting is encountered in numerical results from both authors, compared to experimental. Numerical results presented here seem to be closer to experimental than those presented in [12].

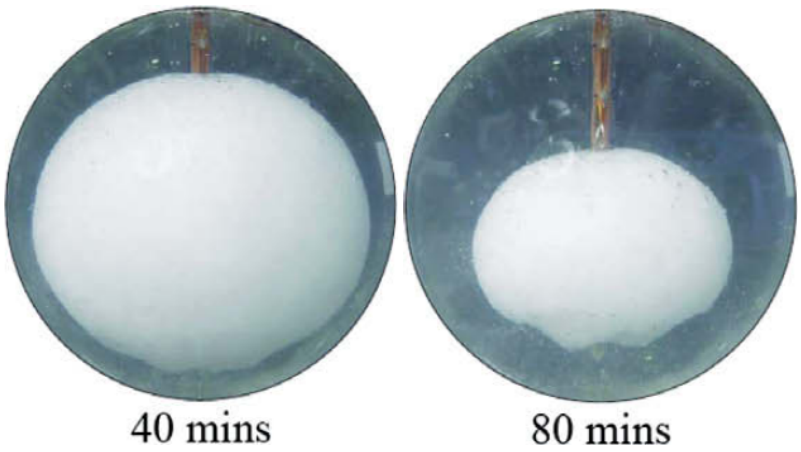

Figure 2.8: Experimental results of the melting N-Octadecane in a spherical capsule, at 40 and at 80 minutes. Reprinted from [12] with permission from Elsevier.

Different reasons could be causing the differences between numerical and experimental results, as in the previous test cases. Some of the most relevant could be:

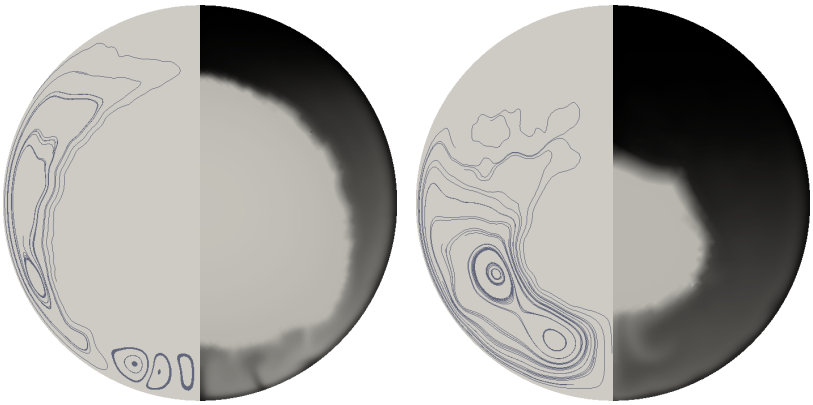

(a) t = 40 min (b) t = 80 min

Figure 2.9: Our results. Left half showing velocity streamlines and right half temperature maps (dark region: high temperature; clear region: low temperature).

- Constant density has been assumed, while the n-octadecane presents a variation of the density of around 14% respect to solid density. Furthermore, the real spherical container has an opening at the top, allowing the exit of fluid. Perfect spherical shape has been assumed in the simulations.
- Assumption of the convective heat transfer in the temperature boundary condition.
- Other thermophysical properties have also been considered constant.
- 2D behaviour has been assumed, neglecting possible 3D pattern.

2.5 Conclusions

Fixed-grid, enthalpy formulation for unstructured meshes using explicit time schemes is presented. The fluid is considered Newtonian and incompressible, and the density change between solid and liquid phases is not considered.

The form of the convective term of the energy equation is discussed. Taking into account that its volume integration is sometimes performed over two-phase-containing cells (interface cells), and observing that only the liquid phase is transported between different cells, it is concluded that only the liquid enthalpy should be considered in the convective term. Furthermore, as solid and liquid densities are assumed equal, there

is no mass accumulation in any cell and latent enthalpy get cancelled out, leaving only the sensible enthalpy of the liquid phase. The effect of considering total enthalpy in the convective term is analysed.

Pressure-velocity decoupling is presented in a somewhat detailed manner, indicating its treatment in solid boundaries. The resulting system of equations of pressure (with variable coefficients) is presented and its particular form in the solid nodes is pointed out.

Regarding the momentum source term introduced by the porosity model, it has been concluded that its time integration has to be performed using an implicit scheme due to stability issues. Furthermore, for the case of modeling a fixed temperature phase change, different expressions of the coefficient S are discussed, and an alternative to the expressions proposed by [6, 10] (Eq. (2.47)) is presented. It is concluded that the Darcian expression proposed by [6] (Eq. (2.46)) is the best behaved in terms of smoothness, while Eq. (2.48) proposed in this work should behave better than Eq. (2.47) being easier to compute than Eq. (2.46). It has also been pointed out that some care should be taken in choosing coefficient C in case of using Eq. (2.47), since a poor choice could produce an insufficient damping efect in almost-solid cells. This choice is not so critical in this aspect when some of the other two expressions is adopted, although it would indeed affect the smoothness of the produced damping effect.

Model implementation has been tested using three cases, and results have been compared against experimental and numerical results from the literature. Good agreement with numerical results has been observed. Overall behaviour of experiments is reproduced fairly well, although some differences are encountered, e.g. in the Tin melting case, where a multi-cellular behaviour —which has not been observed in the experiments— is obtained. These discrepancies are in accordance with results obtained by other authors.

Acknowledgements

This work has been financially supported by the *Ministerio de Economía y Competitividad, Secretaría de Estado de Investigación, Desarrollo e Innovación*, Spain (ENE-2011-28699), by Termo Fluids S.L., by the *Secretaria d'Universitats i Recerca (SUR) del Departament d'Economia i Coneixement (ECO) de la Generalitat de Catalunya* and by the European Social Fund.

References

[1] L. S. Yao and J. Prusa, *Advances in Heat Transfer. Melting and Freezing*, vol. 19. Elsevier, 1989.

[2] A. Gil, M. Medrano, I. Martorell, A. Lázaro, P. Dolado, B. Zalba, and L. F. Cabeza, "State of the art on high temperature thermal ebergy storage for power generation. part 1—Concepts, materials and modellization," *Renew. Sust. Energ. Rev.*, no. 14, pp. 31–55, 2010.

[3] B. Zalba, J. M. Marín, L. F. Cabeza, and H. Mehling, "Review on thermal energy storage with phase change: materials, heat transfer analysis and applications," *Appl. Therm. Eng.*, no. 23, pp. 251–283, 2003.

[4] J. Stefan, "Ueber die Theorie der Eisbildung, insbesondere ueber die Eisbildung im Polarmeere," *Ann. Physik Chemie*, vol. 42, pp. 269–286, 1891.

[5] `http://www.encyclopediaofmath.org/index.php?title=Stefan_problem&oldid=15955`. Encyclopedia of Mathematics, "Stefan Problem."

[6] V. Voller and C. Prakash, "A fixed grid numerical modelling methodology for convection-diffusion mushy region phase change problems," *Int. J. Heat Mass Tran.*, vol. 30, pp. 1709–1719, 1987.

[7] G. Beckett, J. A. Mackenzie, and R. M. L., "A moving mesh finite element method for the solution of two-dimensional stefan problems," *J. Comput. Phys.*, vol. 168, pp. 500–518, 2001.

[8] H. S. Udaykumar, R. Mittal, and W. Shyy, "Computation of solid-liquid phase fronts in the sharp interface limit on fixed grids," *J. Comput. Phys.*, vol. 153, pp. 535–574, 1999.

[9] R. Viswanath and Y. Jaluria, "A comparison of different solution methodologies for melting and solidification problems in enclosures," *Numer. Heat Tr. B-Fund.*, vol. 24, pp. 77–105, 1993.

[10] A. D. Brent, V. R. Voller, and K. J. Reid, "Enthalpy-porosity technique for modelling convection-diffusion phase change: Application to the melting of a pure metal," *Numer. Heat Transfer*, vol. 13, pp. 297–318, 1988.

[11] M. Costa, A. Oliva, C. D. Pérez-Segarra, and R. Alba, "Numerical simulation of solid-liquid phase change phenomena," *Comput. Method. Appl. M.*, vol. 91, no. 1-3, pp. 1123–1134, 1991.

[12] F. L. Tan, S. F. Hosseinizadeh, J. M. Khodadadi, and L. Fan, "Experimental and computational study of constrained melting of phase change materials (PCM) inside a spherical capsule," *Int. J. Heat Mass Tran.*, vol. 52, pp. 3464–3472, 2009.

[13] D. A. Nield and A. Bejan, *Convection in Porous Media, 3rd edition*. Springer, 2006.

[14] O. Lehmkuhl, C. D. Pérez-Segarra, R. Borrell, M. Soria, and A. Oliva, "TERMOFLUIDS: A new Parallel unstructured CFD code for the simulation of turbulent industrial problems on low cost PC Cluster," *Lect. Notes Comput. Sci. Eng.*, vol. 67, pp. 275–282, 2009.

[15] O. Lehmkuhl, *Numerical resolution of turbulent flows on complex geometries*. PhD thesis, Universitat Politècnica de Catalunya, 2012.

[16] R. W. C. P. Verstappen and A. E. P. Veldman, "Symmetry-preserving discretization of turbulent flow," *J. Eng. Math.*, vol. 187, no. 1, pp. 343–368, 2003.

[17] F. N. Felten and T. S. Lund, "Kinetic energy conservation issues associated with the collocated mesh scheme for incompressible flow," *J. Comput. Phys.*, vol. 215, no. 2, pp. 465–484, 2006.

[18] S. V. Patankar, *Numerical Heat Transfer and Fluid Flow*. Ch. 5, Hemisphere Publishing Corporation, 1980.

[19] P. M. Gresho and R. L. Sani, "On pressure boundary conditions for the incompressible navier-stokes equations," *Int. J. Numer. Meth. Fl.*, vol. 7, pp. 1111–1145, 1987.

[20] C. Gau and R. Viskanta, "Melting and solidification of a pure metal on a vertical wall," *J. Heat Trans.-T. ASME*, vol. 108, pp. 174–181, 1986.

[21] B. Vidal, *Modelización del cambio de fase sólido líquido. Aplicación a sistemas de acumulación de energia térmica.* PhD thesis, Universitat Politècnica de Catalunya, Spain, 2007.

[22] N. Hannoun, V. Alexiades, and Z. T. Mai, "Resolving the controversy over tin and gallium melting in a rectangular cavity heated from the side," *Numer. Heat Tr. B-Fund.*, vol. 44, pp. 253–276, 2003.

[23] F. Wolff and R. Viskanta, "Melting of a pure metal from a vertical wall," *Exp. Heat Transfer*, vol. 1, pp. 17–30, 1987.

[24] D. Mansutti and E. Bucchignani, "On the importance of solid deformations in convection-dominated liquid/solid phase change of pure materials," *Appl. Math.*, vol. 56, no. 1, pp. 117–136, 2011.

[25] F. L. Tan, "Constrained and unconstrained melting inside a sphere," *Int. Commun. Heat Mass*, vol. 35, pp. 466–475, 2008.

3

Fixed-grid modeling with variable thermo-physical properties. Melting of n-Octadecane inside a spherical capsule.

Contents of this chapter have been submitted for publication as:

P. A. Galione, O. Lehmkuhl, J. Rigola and A. Oliva, "Fixed-grid numerical modeling of melting and solidification using variable thermo-physical properties —Application to the melting of n-Octadecane inside a spherical capsule," submitted to *International Journal of Heat and Mass Transfer*, 2014.

Abstract

A fixed-grid enthalpy model for unstructured meshes and explicit time integration schemes [1] is here extended for taking into account the change in density and other thermo-physical properties with the temperature and phase. Thermal expansion and contraction associated to the phase change are taken into account in the conservation equations, and different strategies for the numerical treatment of the energy equation are discussed in detail. Further modifications to the original model are also presented.

The proposed model is used for simulating a case of melting of n-Octadecane inside a spherical capsule. Two and three-dimensional simulations are performed using constant and variable properties. A comprehensive examination of the thermophysical properties is performed, and the different values and correlations used are here presented and criticised. Differences in the flow patterns are encountered between two and three-dimensional simulations. The effects of considering constant or variable properties are discussed. Two different thermal boundary conditions are tested and the results are compared against experimental data obtained from the literature.

3.1 Introduction

Materials which undergo a phase transition at a temperature of interest for some application, are usually called phase change materials (PCMs). Due to the lower density changes involved, solid-liquid phase change is usually preferred over liquid-vapor. This change of phase can be exploited, for example, to store thermal energy. Taking advantage of both latent and sensible energy capacities of the materials result in devices with higher energy densities, and therefore, allow the reduction of both the storage weight and volume. One application of PCMs where extensive research is being carried out nowadays, is the thermal energy storage for for concentrated solar power stations (CSP), see for instance [2–4].

A common feature of many of the PCMs usually considered —such as paraffins, hydrated salts and salt mixtures—is their low thermal conductivity. For this reason, different strategies for increasing the heat transfer rate of devices using PCMs are considered [2, 5]. One of the most studied thermal enhancement options is the containment of the PCM in capsules, in order to obtain a high surface-to-volume ratio. Studies of storage systems consisting of packed beds of encapsulated PCM are abundant in the literature, e.g. [6–8].

It has been seen that natural convection effects in the melting of PCMs enclosed in different kind of cavities, play a significant role in the evolution of the melting rate and shape of the solid-liquid interface (see e.g. [9, 10]). Besides the dynamics and heat transfer phenomena involved within the fluid phase, simulations need to address the heat transfer within the solid phase and an accurate representation of the moving boundary between phases. Different modeling strategies have been adopted for the numerical simulation of this kind of moving boundary problems, such as adapting grid (e.g. [11]), fixed-grid enthalpy (e.g. [12]) and Eulerian-Lagrangian (e.g. [13]) models. Within these, fixed-grid enthalpy models have been used more extensively, due to their relative mathematical and computational simplicity and their possibility to address the “mushy zones”produced in materials whose phase-change occurs in a temperature range. Generally, fixed-grid models have been used along with implicit

time integration schemes [12, 14, 15].

Several works have studied the heat transfer in PCMs contained in spherical capsules. Tan et al. [15] presented an experimental and numerical study of the melting of n-Octadecane contained in a spherical capsule. A hollow tube was placed in the axis of the sphere in order to hold the thermocouples and the solid phase from sinking to the bottom due to gravitational force. A two-dimensional (2D) model was used for the numerical simulations, assuming axi-symmetry with respect to the vertical axis. Qualitative agreement with experimental results was achieved, but a higher melting rate was reported for the numerical simulations. Discrepancies were believed to be caused due to not taking into account accurately the convection and thermal stratification of the thermal bath in which the capsule was immersed. Assis et al. [16] performed a numerical and experimental study of the unconstrained melting of a phase change material inside a spherical capsule. Their numerical simulations were performed using the comercial CFD code ANSYS FLUENT 6.0 with an enthalpy-porosity model based on the works of Voller et al. [12], using variable thermo-physical properties and simulating the interface between air and PCM with a VOF technique. However, the numerical treatment of the change of density between solid and liquid phases is not clearly stated in their paper. Axi-symmetry was assumed in their simulations. Zhao et al. [17] performed transient 2D analysis of heat transfer in encapsulated PCMs, using both front-tracking and enthalpy-porosity methods. They validated their simulations with the enthalpy-porosity model using the constrained n-Octadecane melting case of Tan et al. [15], adopting constant thermo-physical properties. Results obtained showed a good agreement with the numerical results of Tan et al. [15], i.e. qualitative agreement with experimental results but a faster melting rate. Elmozughi et al. [18] conducted numerical simulations of melting and solidification in cylindrical and spherical capsules using the enthalpy-porosity method implemented in ANSYS FLUENT code. They used different properties for the liquid and solid phases of the PCM, but constant within each phase, and adopted a Boussinesq approximation in order to account for density differences in the liquid phase. However, the numerical treatment of the density differences between liquid and solid phases is not indicated in detail. Two and three-dimensional simulations of different cases were performed, although no particular 3D flow patterns were reported and axi-symmetry was observed.

No 3D simulations have been found in the literature for the case presented by [15], nor any 2D accounting for the variations of the properties with the temperature. Furthermore, no clarification about the numerical treatment of the flow produced by the expansion or contraction in the solid-liquid interface (if different from that with constant density) has been found in the previously mentioned works.

The present is a continuation of a previous work [1], which dealt with fixed-grid solid-liquid phase-change modeling using explicit time schemes, specially suited

for its combination with turbulence models for simulation of the fluid motion. That model was tested using different benchmark cases found in the literature. Here, several upgrades are introduced into the formulation presented in [1].

First, the way the pressure is solved in the solid-liquid interface is modified by adopting a simpler strategy more convenient for situations of variable density. Furthermore, the model is extended to take into account variations of the thermo-physical properties with the temperature, including the density differences between solid and liquid phases and also within the liquid phase. The resulting modifications on the treatment of the three conservation equations (mass, momentum and energy) are discussed in detail. The strategies for calculating the temperature and liquid fraction from the enthalpy are presented for both materials which change of phase at a fixed temperature and in a temperature range. Furthermore, a variation in the form of the source term is proposed and used in the simulations presented.

The improved numerical model is applied for simulating the melting of a phase-change material (PCM) contained in a spherical capsule, based on the work of Tan et al. [15]. Here, simulations of the case of Tan et al. [15] are presented with the proposed formulation, using two and three-dimensional (3D) unstructured meshes and taking into account the variation of properties with temperature and phase. Unlike several previous works [12, 14–18] a clear distinction between liquid and solid properties is performed in the equations, and more specifically, only the liquid phase is considered in the convective terms due to being the only transporting phase, as suggested in [1].

In order to perform accurate numerical simulations of the melting of n-Octadecane, a comprehensive examination of its physical properties has been performed. Correlations used are presented along with comments about their validity. Simulations have been run using with both constant and variable thermo-physical properties and their results compared. Results showing the development of the interface, as well as the evolution of the temperature at some selected positions, are presented and compared against the experimental results obtained from [15]. Results show that the 3D treatment allows to reproduce flow patterns that are not simulated with the 2D models and are in better agreement with experimental results.

3.2 Mathematical modeling

The equations presented in [1] for modelling solid-liquid phase change CFD are here used and extended to variable physical properties. Specifically, the density is allowed to vary between solid and liquid phases and within the liquid phase. This introduces an important modification to the model, since the traditional incompressibility condition ($\nabla \cdot \vec{u} = 0$) is not valid anymore.

Resulting governing equations (mass, momentum and energy balances) are:

$$\frac{\partial \rho_m}{\partial t} + \nabla \cdot (\rho_l \vec{u}) = 0 \tag{3.1}$$

$$\frac{\partial \rho_l \vec{u}}{\partial t} + \nabla \cdot \left(\rho_l \vec{u} \frac{\vec{u}^*}{\epsilon} \right) = -\nabla p + \nabla \cdot (\mu_l \nabla \vec{u}) + \rho_l \epsilon \vec{g} - S\vec{u} \tag{3.2}$$

$$\frac{\partial \rho_m h_m}{\partial t} + \nabla \cdot (\rho_l h_l \vec{u}) = \nabla \cdot (\lambda_m \nabla T) \tag{3.3}$$

where:

$$\rho_m = \epsilon \rho_l + (1 - \epsilon) \rho_s \tag{3.4}$$

$$\rho_m h_m = \epsilon \rho_l h_l + (1 - \epsilon) \rho_s h_s \tag{3.5}$$

Sub-indexes l and s indicate properties of the liquid and solid phases, respectivley; while m indicates a property of the mixture of solid and liquid phases (including the cases of pure liquid and solid). ϵ is the volumetric liquid fraction, which can take values between 0 (solid) and 1 (liquid). Velocity $\vec{u}$ corresponds to the seepage or Darcy velocity [19] in the presence of a mixture of solid and liquid phases. Enthalpy h include both liquid and sensible components.

Thermal conductivity λ_m is an effective conductivity, which can be either the conductivity of the pure phase —in the mesh cells where there is only one phase present— or a combination of the conductivities of both phases —in the cells where there is a mixture of solid and liquid (interface). If the interface zone is a "mushy" zone, this value could be calculated using some of the correlations used for the heat transfer in porous media [19, 20].

Equation (3.2) corresponds to the momentum equation for flow through a porous medium [21], where the momentum source term coefficient S has been simplified, only accounting for the Darcian part of the drag force induced by the presence of the solid phase, as in [22]. This equation is only useful in the liquid-containing domain.

It has been assumed that the solid phase has no motion, and therefore, the transport of properties is carried out by the liquid phase only. This is the reason for the advective terms only to include the properties of the liquid phase, as mentioned in [1].

If using constant physical properties, Boussinesq approximation is performed in order to account for the thermal expansion in the fluid.

3.2.1 Enthalpy - temperature relations

The energy conservation equation (3.3) is expressed in terms of enthalpy in its transient and convective terms. Therefore, relations between enthalpy and temperature

have to be used explicitly in order to be able to determine the thermodynamic state of the material. Since the aim is to be able to take into account the variation of the thermo-physical properties with the temperature, the variation of the specific heat (C_p) and density are considered.

Next, this task is discussed in some detail for cases of phase change occurring at a fixed temperature (for pure substances) or in a temperature range (for mixtures of substances).

Fixed phase-change temperature

In pure substances, the melting point is a fixed value. Therefore, the change in enthalpy in the phase change is only due to changes in the amount of substance that changes from liquid to solid, or viceversa. Hence, there is no function relating h and T but there is a function relating h and f (mass liquid fraction) instead.

For the liquid and solid phases, relations between h and T exist, being the usual relations for sensible enthalpy changes:

$$h_s - h_{ref} = \underbrace{\int_{T_{ref}}^{T} C_{p,s} dT}_{\text{sensible}} \qquad (T < T_{sl})$$

$$h_l - h_{ref} = \underbrace{\int_{T_{sl}}^{T} C_{p,l} dT}_{\text{sensible liquid}} + \underbrace{\int_{T_{ref}}^{T_{sl}} C_{p,s} dT}_{\text{sensible solid until m.p.}} + \underbrace{L}_{\text{latent}} \qquad (T > T_{sl})$$

For the interface ($T = T_{sl}$) the enthalpy can be calculated from:

$$h_m - h_{ref} = \underbrace{\int_{T_{ref}}^{T_{sl}} C_{p,s} dT}_{\text{sensible solid until m.p.}} + \underbrace{fL}_{\text{latent}}$$

with:

$$f = \frac{m_l}{m_l + m_s} = \frac{h_m - h_{s_{@T_{sl}}}}{h_{l_{@T_{sl}}} - h_{s_{@T_{sl}}}}$$

The "thermodynamic state" of the mixture is determined by the mass liquid fraction f, which is calculated from the enthalpy of the mixture h_m.

Depending on the values of C_p for both phases, the inversion of the relation $h - T$ can be more or less difficult. The easiest case is that with constant values of C_p for both phases, resulting in:

$$T = T_{ref} + \frac{h_s - h_{ref}}{C_{p,s}} \qquad (T < T_{sl})$$

$$T = T_{sl} + \frac{h_l - \left[h_{ref} + C_{p,s}(T_{sl} - T_{ref}) + L\right]}{C_{p,l}} \qquad (T > T_{sl})$$

However, more complicated expressions for $C_p(T)$ are usually found, which can make the work of inverting the $h - T$ relations very hard. A useful way of easing this task is to piecewise-linearize these expressions in some temperature ranges. Since the values of C_p for each phase generally do not change significantly in the working range of temperatures, a single interval of linearization might be sufficient (this is the approach that has been adopted in this work for the n-Octadecane). If this were the case, the values of C_p would be expressed as:

$$C_{p,s} = C_{p,s_{@T_{min}}} + \frac{C_{p,s_{@T_{sl}}} - C_{p,s_{@T_{min}}}}{T_{sl} - T_{min}}(T - T_{min}) \qquad (T_{min} < T < T_{sl})$$

$$C_{p,l} = C_{p,l_{@T_{sl}}} + \frac{C_{p,l@T_{max}} - C_{p,l_{@T_{sl}}}}{T_{max} - T_{sl}}(T - T_{sl}) \qquad (T_{sl} < T < T_{max})$$

or, expressed in a generic linear form:

$$C_p = C_{p0} + C_{p1}T$$

resulting in the following generic expression for h depending on T:

$$h - h_0 = C_{p0}(T - T_0) + 0.5C_{p1}(T^2 - T_0^2)$$

where the 0 represents either the melting point sl (for the liquid range) or the reference state ref (for the solid range). From here on, T is calculated as:

$$T = -C_{p0}/C_{p1} + \sqrt{2\left(\frac{h - h_0}{C_{p1}}\right) + \left(\frac{C_{p0}}{C_{p1}} + T_0\right)^2}$$

In the interface, instead of using the mass liquid fraction f it is useful to use the volumetric liquid fraction (or porosity) ϵ, since it is a variable that is explicitly used in the momentum equation. Hence, using Eq. (3.5), the following equation for ϵ can be obtained:

$$\epsilon = \frac{\rho_m h_m - \rho_s h_s}{\rho_l h_l - \rho_s h_s} \tag{3.6}$$

Furthermore, using Eq. (3.4), the following expression —which does not depend on ρ_m— is obtained:

$$\epsilon = \frac{\rho_s(h_m - h_s)}{\rho_l h_l - \rho_s h_s + (\rho_s - \rho_l)h_m} \tag{3.7}$$

Since ρ_l, ρ_s, h_l and h_s are all fixed and known values at $T = T_{sl}$, the porosity can be directly calculated from Eq. (3.7) having previously calculated h_m from the energy equation. It should be noted that Eq. (3.7) is not linear with h_m in the general case, since h_m is also present in the denominator. In the particular case of having equal solid and liquid densities, the expression results to be linear.

It should be noted that with equation (3.7), the porosity is calculated directly from the enthalpy (h_m) and not from the temperature, as is usually the case when an implicit time integration is used (e.g. [12, 14, 15]), avoiding the need for a numerical maneuver such as the definition of an artificial range of temperatures (small) in which the material is assumed to melt, in order to have an expression of ϵ as a function of T.

Phase-change in a temperature range

The mixture of two or more substances do not usually change of phase at a sharp melting point, but they have a range of temperatures in which both phases coexist. In these cases, there exist a region in which both phases are present, called "mushy" zone, and the interface is not a surface anymore.

Being T_s and T_l and $h_{s_{@T_s}}$ and $h_{l_{@T_l}}$ the solidus and liquidus temperatures and enthalpies, respectively; the enthalpies of the liquid and solid phases, h_l and h_s, could be defined as follows:

$$\begin{aligned}
h_l &= h_{l_{@T_l}} + \int_{T_l}^{T} C_{p,l}(T)dT && (T > T_s)\\
h_s &= h_{s_{@T_s}} - \int_{T}^{T_s} C_{p,s}(T)dT && (T < T_l)\\
\rho_l &= \mathrm{f}_1(T) && (T > T_s)\\
\rho_m &= \epsilon\rho_l + (1-\epsilon)\rho_s && (T_s < T < T_l)\\
\epsilon &= \frac{\rho_m h_m - \rho_s h_s}{\rho_l h_l - \rho_s h_s} && (T_s < T < T_l)
\end{aligned}$$

where ρ_s has been assumed to be constant over all the range $T < T_l$, ρ_l is some function of the temperature (f_1), and the last is Eq. (3.6). It should be noted that the equations of h_l, h_s and ρ_l have been assumed to be valid also in the whole phase

change range; and differently from what happened with a fixed melting point, these properties are not constant in the phase change range.

The first three equations are valid for the pure phases and the interface, while the other two are only for the interface. These, added to the energy equation (3.3), are six equations for determining seven unknowns ($h_l, h_s, h_m, \rho_l, \rho_m, \epsilon, T$). Therefore, an additional equation is necessary, which could be the relation between f and T (transformed to $\epsilon - T$) coming from the phase diagram of the mixture of substances.

Usually the $f - T$ relation is assumed as linear between the liquidus and solidus temperatures, but more accurate relations could be implemented, e.g. by using the lever rule in binary alloys.

To calculate all the properties, it is necessary to determine T and ϵ from h_m, since T is necessary for calculating h_l, h_s, ρ_l and ρ_s. This will probably result in an iterative procedure, unless the extra equation is the relation between h_m and T, which would allow to directly determine T and from there on, to calculate directly the rest of the properties.

3.3 Numerical implementation

The formulation presented above has been implemented into the CFD computer package TermoFluids [23], which is designed to work with unstructured meshes. Finite volume, collocated discretization and explicit time schemes have been used, with the time step dynamically adapted by estimating upper bounds for the eigenvalues of convective and diffusive operators [24]. The code is parallelized and can be run both on single computers as well as in computing clusters.

Figure 3.1 shows some sketches of unstructured meshes, where the geometrical notation has been introduced. For more information about the way the different terms of the conservation equations have been discretized, please refer to [1,25].

In order to better understand the modifications performed to the previous implementation (presented in [1]), a brief overview of the latter is presented in the first sub-section. Afterwards, the new treatment of mass and momentum equations, momentum source term coefficient, pressure in the interface zone and energy equations is described.

3.3.1 Overview of the previous implementation

For the non-dimensionalized problem, with constant thermo-physical properties, the time-discretization of governing equations (3.1)-(3.3), result in [1]:

$$\nabla \cdot \vec{u}^{n+1} = 0 \tag{3.8}$$

$$\frac{\vec{u}^{n+1} - \vec{u}^{n}}{\Delta t} = R^{n+\alpha}(\vec{u}) - \nabla p_d^{n+1} - S\vec{u}^{n+1} \tag{3.9}$$

$$\frac{h^{n+1} - h^{n}}{\Delta t} = R^{n+\alpha}(\phi) \tag{3.10}$$

Here, $R^{n+\alpha}$ represents the sum of convective, diffusive and buoyancy terms integrated between time steps n and $n+1$ using some time-integration scheme, S is the non-dimensional source term coefficient introduced by the porous medium treatment and ϕ is the non-dimensional temperature. As explained in [1], the momentum source term has to be treated implicitly due to stability reasons.

Decoupling of u^{n+1} and p_d^{n+1} is carried out applying divergence, imposing mass conservation [Eq. (3.8)] and rearranging terms:

$$\Delta t \nabla \cdot \left(\frac{\nabla p_d^{n+1}}{1 + \Delta t S} \right) = \nabla \cdot u^{p} \tag{3.11}$$

where:

$$u^{p} = \left\{ \frac{\vec{u}^{n} + \Delta t R^{n+\alpha}(\vec{u})}{1 + \Delta t S} \right\} \tag{3.12}$$

is a pseudo-predictor velocity, and thus:

$$u^{n+1} = u^{p} - \Delta t \left(\frac{\nabla p_d^{n+1}}{1 + \Delta t S} \right) \tag{3.13}$$

from where the new velocity field (u^{n+1}) is calculated. Equation (3.11) defines a linear system of equations of cell-node pressures, with variable coefficients depending on S, which needs to be solved using a linear solver.

The algorithm for the resolution of the equations is the following:

- Energy equation (3.10): new enthalpy, temperature and porosity fields are calculated.
- Pseudo-predictor velocities u^{p} using previous velocity fields [Eq. (3.12)].
- Pressure equations (3.11): calculation of the system coefficients and resolution using a linear solver (e.g. CG).
- New velocity field using predictor velocity and new pressure field [Eq. (3.13)].

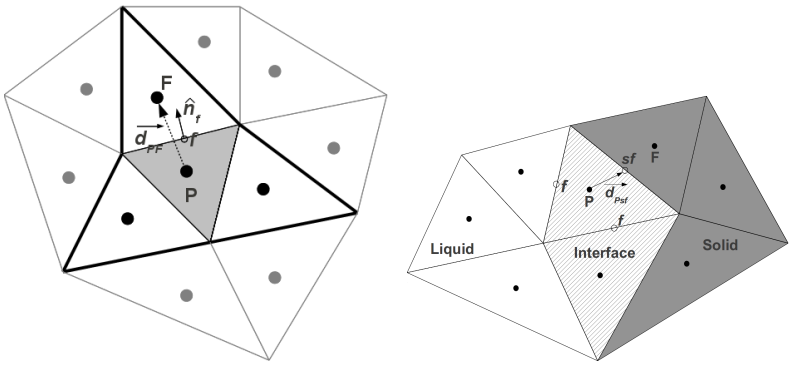

(a) Away from solid nodes.

(b) Near solid nodes. Diferent phases are indicated by the area filling.

Figure 3.1: Notation used for the position of the nodes in an unstructured mesh. Letter P indicates the node being calculated, F a neighbouring node, f the face shared by nodes P and F, $\hat{n}_f$ the vector normal to face f pointing outwards P, and $\vec{d_{PF}}$ the vector going from P to F. If node F contains solid, then the face connecting nodes P and F is denoted sf and the distance from P to this face $\vec{d_{Psf}}$.

3.3.2 Mass and momentum

Numerical implementation of the mass balance is modified by adding the effect of density variations:

$$\frac{\rho_m^{n+1} - \rho_m^n}{\Delta t} = -\nabla \cdot (\rho_l^{n+1} \vec{u}^{n+1}) \tag{3.14}$$

Resulting in a modified version of the Poisson-like equations from that presented in [1] [i.e. Eq. (3.11)]:

$$\Delta t \nabla \cdot \left(\frac{\nabla p^{n+1}}{1 + \Delta t S / \rho_l^{n+1}} \right) = \nabla \cdot \left(\frac{\rho_l u^p}{1 + \Delta t S / \rho_l^{n+1}} \right) + \frac{\rho_m^{n+1} - \rho_m^n}{\Delta t} \tag{3.15}$$

where, using Adams-Bashforth 2$^{\text{nd}}$ order time integration scheme (for simplicity):

$$\rho_l u^p = \rho_l \vec{u}^n + \Delta t \left[\frac{3}{2} R^n(\vec{u}) - \frac{1}{2} R^{n-1}(\vec{u}) \right] \tag{3.16}$$

is a pseudo-predictor velocity, and thus:

$$\rho_l u^{n+1} = \left(\frac{\rho_l u^p - \Delta t \nabla p^{n+1}}{1 + \Delta t S / \rho_l^{n+1}} \right) \tag{3.17}$$

from where the new velocity field (u^{n+1}) is calculated. R is the sum of convective, diffusive and buoyancy source terms.

The change in density is taken into account in the last term of the right hand side of Eq. (3.15). The new density (ρ_m^{n+1}) is assumed to be known at this point, since the energy equation is resolved before than momentum, and therefore, the new temperature field and thermo-physical properties are known.

In the case of a fixed melting point, Eq. (3.4) can be used to calculate the change in density in the interface cells:

$$\frac{\rho_m^{n+1} - \rho_m^n}{\Delta t} = \frac{\epsilon^{n+1} - \epsilon^n}{\Delta t} \left(\rho_l - \rho_s\right) \tag{3.18}$$

which could be plugged into Eq. (3.15); e.g. when ρ_l is considered constant and the Boussinesq approximation is used for taking into account the thermal expansion/contraction in the liquid phase.

It should be noted that u^p in Eq. (3.16) does not include the effect of the source term coefficient S. This effect is included afterwards, when the velocity is corrected by the effect of the pressure gradient, in Eq. (3.17). This approach is different from that chosen in [1], where the effect of the momentum source term was included in the predictor velocity already. The modification presented here results in an interpolation of the face velocities more consistent with that used in the pressure terms in [1], which do not include the effect of the source term until the moment of performing the integration of the pressure gradient [first term of Eq. (3.15)].

Integrating Eq. (3.15) in space over a mesh cell and discretizing, it remains:

$$\frac{\Delta t}{V_\mathrm{P}} \sum_f \underbrace{\left[\left(\frac{\nabla p^{n+1}}{1 + \Delta t S / \rho_l^{n+1}} \right)_f \cdot \hat{n}_f A_f \right]}_{\text{modified pressure gradient flux}} - \frac{1}{V_\mathrm{P}} \sum_f \underbrace{\left\{ \left[\frac{(\rho_l \vec{u})^p}{1 + \Delta t S / \rho_l^{n+1}} \right]_f \cdot \hat{n}_f A_f \right\}}_{\text{modified predictor velocity flux}} = \underbrace{\frac{\rho_{m,\mathrm{P}}^{n+1} - \rho_{m,\mathrm{P}}^n}{\Delta t}}_{\text{thermal expansion}}$$

which, in short, stands for mass conservation:

$$\frac{1}{V_\mathrm{P}} \sum_{f_\mathrm{P}} \dot{m}_f^{n+1} = \frac{\rho_{m,\mathrm{P}}^{n+1} - \rho_{m,\mathrm{P}}^n}{\Delta t} \tag{3.19}$$

where the outgoing mass fluxes through faces are calculated as:

$$\dot{m}_f^{n+1} = \frac{\dot{m}_f^p - \Delta t \nabla p^{n+1} \cdot \hat{n}_f A_f}{\left(1 + \Delta t S / \rho_l\right)_f} \tag{3.20}$$

The resulting system of pressure equations can be written as:

$$a_{\mathtt{P}}\tilde{p}_{\mathtt{P}}^{n+1} + \sum_{f_{\mathtt{P}}} a_{\mathtt{F}_f}\tilde{p}_{\mathtt{F}_f}^{n+1} = b_{\mathtt{P}} \tag{3.21}$$

where $\tilde{p} = \Delta t\, p$ and:

$$\begin{aligned}
a_{\mathtt{F}_f} &= \frac{A_f}{(\overrightarrow{d_{PF}}\cdot\hat{n})_f}\frac{\left(\theta_{F_f}+\theta_P\right)}{2}\\
a_{\mathtt{P}} &= \sum_{f_{\mathtt{P}}} -a_{\mathtt{F}_f}\\
b_{\mathtt{P}} &= \sum_{f_{\mathtt{P}}}\left[\dot{m}_f^p\frac{\left(\theta_{F_f}+\theta_P\right)}{2}\right] + V_{\mathtt{P}}\frac{\rho_{m,\mathtt{P}}^{n+1}-\rho_{m,\mathtt{P}}^{n}}{\Delta t}\\
\theta_i &= \frac{1}{1+\Delta t S_i/\rho_{l,i}^{n+1}} \qquad (i=\mathtt{F}_f,\mathtt{P})
\end{aligned}$$

Momentum source term coefficient (S)

It can be observed [Eq. (3.17)] that the source-term coefficient S produces a damping of the new velocity by a factor of

$$\frac{1}{1+\Delta t S/\rho_l} \tag{3.22}$$

In [1], different forms of the momentum source-term coefficient (S) were studied in terms of the "smoothness " of the associated velocity damping produced. In particular, the approach proposed by Voller et al. [12]

$$S = \frac{C(1-\epsilon)^2}{\epsilon^3+q} \tag{3.23}$$

where C is an arbitrary (big) constant and q is a very small value included to avoid division by zero, resulted to be the best of those studied, in terms of smoothness.

However, analyzing equations (3.22) and (3.23), it can be seen that the damping effect depends on the values of C, ρ_l and Δt. In the case of a porous medium, there are expressions to calculate the value of C from the thermo-physical properties of the fluid [19]. In the case of a change of phase in a temperature range, where a mushy zone is formed, some of these expressions should be used. On the other hand, as

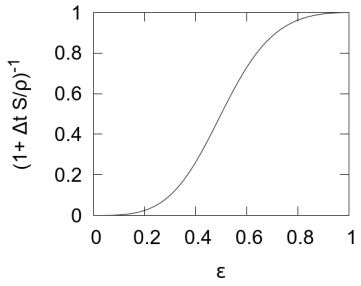

Figure 3.2: Damping factor vs. ϵ, with the proposed approach

stated in [14] and [1], in the case of a change of phase at a fixed temperature there is no mushy zone and the interface should be of infinitesimal width. Therefore, there is no physical meaning of the source term, and it is just intended to act as a velocity damper in the solid-containing cells.

With this in mind, a new strategy is followed for the choice of S. The idea is to retain the smoothness obtained with Eq. (3.23), with respect to the value of ϵ, with independence of the values of Δt and ρ. Hence, a damping of 0.5 is fixed for $\epsilon = 0.5$, resulting in:

$$S = \frac{\rho_l}{2\Delta t}\left[\frac{(1-\epsilon)^2}{\epsilon^3 + q}\right]$$

and (disregarding q):

$$\frac{1}{1 + \Delta t S/\rho_l} = \frac{2\epsilon^3}{2\epsilon^3 + (1-\epsilon)^2}$$

The resulting curve of the damping factor vs. ϵ is shown in figure 3.2.

Solid boundary conditions

Solid, no-slip, boundary conditions are treated in detail in this section; not only because they are extensively used in the study cases but also because they are related to the way the solid-liquid interface inside the domain have been treated in [1]. A modification to such strategy is the issue of the next section.

The velocity and mass flux in the solid boundaries are fixed to zero, the predictor velocity is not calculated since it is not needed (pressure of the boundary not included in the pressure system of equations, as in [1]):

$$\vec{u}_{sb} = 0; \quad \dot{m}_{sb} = 0$$

The pressure is needed for calculating the pressure gradient of the cell and is determined in order to give a pressure gradient such that the cell-centered velocity results parallel to the boundary:

$$\vec{u}_P \cdot \hat{n}_{sb} = 0 \tag{3.24}$$

thus, using Eq. (3.17):

$$\begin{aligned} \vec{\rho}_l u_P \cdot \hat{n}_{sb} &= \left(\frac{\rho_l \vec{u}^p - \Delta t \nabla p}{1 + \Delta t S/\rho_l} \right)\Big|_P \cdot \hat{n}_{sb} = 0 \\ &\Rightarrow (\rho_l \vec{u}^p - \Delta t \nabla p)_P \cdot \hat{n}_{sb} = 0 \end{aligned}$$

which, integrating and discretizing over the cell containing node P, gives:

$$\begin{aligned} &\frac{V \rho_l \vec{u}^p}{\Delta t}\bigg|_P \cdot \hat{n}_{sb} - \sum_{f_P} p_f \hat{n}_f A_f \cdot \hat{n}_{sb} = 0 \Rightarrow \\ p_{sb} A_{sb} &= \frac{V \rho_l \vec{u}^p}{\Delta t}\bigg|_P \cdot \hat{n}_{sb} - \sum_{f \neq sb} p_f \hat{n}_f A_f \cdot \hat{n}_{sb} \end{aligned} \tag{3.25}$$

from where the pressure of the solid boundary p_{sb} is calculated, after having determined the variables $\vec{u}^p$ and p in the cells.

This condition on pressure in fact arises from a 2$^{\text{nd}}$ order boundary condition for $\vec{u} \cdot \hat{n}_{sb}$, as is shown next. Due to mass conservation (neglecting the possible change in fluid density), the component of the velocity normal to the solid face should be zero:

$$\nabla \cdot \vec{u}_{sb} = 0 \Rightarrow \cancelto{0}{\frac{\partial u_{t_{1sb}}}{\partial x_{t_{1sb}}}} + \cancelto{0}{\frac{\partial u_{t_{2sb}}}{\partial x_{t_{2sb}}}} + \frac{\partial u_n}{\partial x_{n_{sb}}} = 0 \Rightarrow \frac{\partial u_n}{\partial x_n}\bigg|_{sb} = 0$$

where $\hat{t_1}_{sb}$ and $\hat{t_2}_{sb}$ are the two components tangent to the solid face, over which the velocity is zero in all the solid boundary. Therefore, the component of the cell-centered velocity normal to the solid boundary can be approximated as:

$$\begin{aligned} \vec{u_P} \cdot \hat{n}_{sb} &= \cancelto{0}{\vec{u}_{sb}} \cdot \hat{n}_{sb} + \cancelto{0}{\frac{\partial u_n}{\partial x_n}\bigg|_{sb}} \Delta x_n + O(\Delta x_n^2) \\ &\Rightarrow \vec{u_P} \cdot \hat{n}_{sb} = 0 + O(\Delta x_n^2) \end{aligned}$$

from where it can be seen that Eq. (3.24) results in a second order approximation.

It should be pointed out that this boundary condition for pressure is applied due to being using a collocated mesh scheme, where the velocities at the center of the cells are not the ones directly involved in the mass conservation. The pressure system of equations involves the mass fluxes through the cell faces, and therefore, the cell-centered pressure values are determined in order to enforce mass conservation of those mass fluxes. For this task, the pressure of the solid boundaries is not used nor needed (as seen in [1]), which is equivalent to adopting the usual boundary condition for pressure in solid faces ($\frac{\partial p}{\partial n} = 0$) in the poisson-like system of equations.

If $\frac{\partial p}{\partial n} = 0$ is used as the boundary condition for calculating the pressure in the solid faces, large normal velocities may result due to the effect of body forces (e.g. gravitational), which are not correctly counteracted by the resulting pressure gradient. This effect is mentioned in [26] and has been experienced by the authors.

However, the cell-centered velocities are calculated afterwards, and involve the calculation of the pressure gradient over the cell. This pressure gradient is the one using the value of the pressure in the solid boundary and is the one affected by the boundary condition imposed.

Furthermore, the boundary condition imposed by Eq. 3.25 ensures that the viscous stress normal to the solid boundary is zero as it should be [26], without needing to modify the diffusive term explicitly:

$$\nabla \cdot (\mu \nabla \vec{u}) \backsimeq \sum_f \mu_f \nabla \vec{u} \cdot \hat{n}_f =$$

$$\sum_{f \neq sb} \mu_f \nabla \vec{u} \cdot \hat{n}_f + \mu_{sb} \left(\cancelto{0}{\left.\frac{\partial u_n}{\partial x_n}\right|_{sb}} \hat{n}_{sb} + \frac{\partial u_{t_1}}{\partial x_n} \hat{f}_{1sb} + \frac{\partial u_{t_2}}{\partial x_n} \hat{f}_{2sb} \right)$$

Pressure equation - cells close to the solid phase

The pressure field effectively acts in the liquid domain, where it enforces mass conservation. In the solid domain it is not needed and it is required not to produce artificial "filtration" of flow through the interface into (or out from) the solid domain. This filtration effect could be produced due to the fact that between neighbouring liquid and solid cells, resulting from the solution of the system of equations, the pressure values will generally be different, and therefore, mass flows through the faces could be different from zero if calculated using Eq. (3.20).

As in [1], the strategy is to decouple liquid (or liquid-containing) and solid domains by modifying the pressure system of equations. In [1], this decoupling was

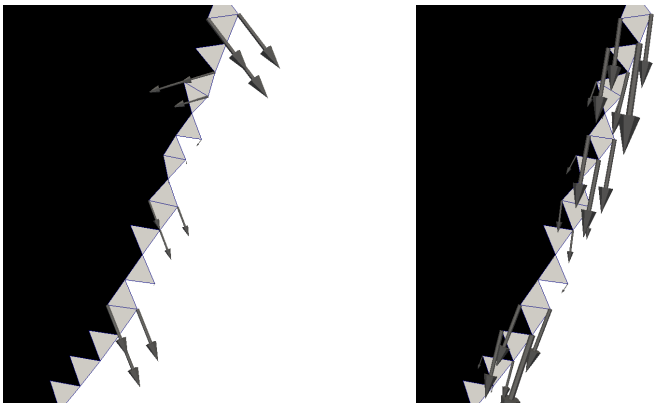

(a) Internal solid boundary approach. (b) Proposed approach.

Figure 3.3: Velocity vectors of liquid-containing cells close to solid cells. Dark zone corresponds to the solid phase.

performed treating the solid-cells faces as solid boundaries. This internal boundary condition was applied to the faces of the solid cells in the same way as for the solid boundaries of the domain, enforcing the cell-centered velocities to be parallel to these internal solid boundaries (see previous sub-section).

This strategy resulted in a fluid velocity field —near the solid phase— that changed direction following the shape of the solid cells, specially where totally liquid cells are in contact with totally solid ones. Since the interface is not exactly determined and its shape depends on the shape of the mesh cells, this "internal solid boundary" is usually highly irregular (this is particularly true in the case of a 3D unstructured mesh of a spherical capsule), and therefore, to enforce the velocity field to follow this artificial boundaries does not necessarily result in an accurate representation of the flow [see e.g. the sketch in figure 3.3(a)].

Moreover, the implementation of such internal boundary condition is quite complex in terms of program coding, since different possibilities have to be taken into account regarding the number of solid neighbors of a liquid-containing cell; i.e. if the cell has more than one solid neighbor its cell-centered velocity has to be parallel to all the non-parallel solid faces.

Furthermore, if the changes in density are to be taken into account, the condition on the cell-centered velocity normal to the solid faces has to be modified.

Due to these difficulties in the adoption of the internal solid boundary condition, another simpler approach is proposed in this work, which automatically adapts to the formulation with variable density. Here, the internal solid boundary condition for the

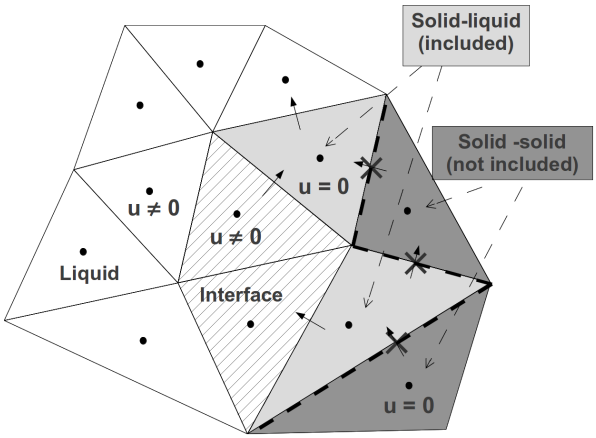

Figure 3.4: Sketch of unstructured mesh. White: liquid. Striped: interface. Light grey: solid-liquid cells (included in the non-trivial sub-system of pressure equations). Dark grey: solid-solid cells (trivial system of pressure equations).

pressure is "alleviated". Instead of directly imposing the solid boundary condition to the internal solid faces, the neighbor solid cell is used as a ghost cell for the pressure and introduced into the pressure system of equations.

Therefore, two categories of solid cells are defined: solid-solid and solid-liquid (see fig. 3.4). The former accounts for the solid cells whose neighbors are all also solid, while the latter contains the solid cells which have at least one liquid-containing neighbor cell. The solid-solid cells are the ones decoupled from the rest, enforcing zero filtration through their faces, while the solid-liquid cells are maintained in the system of pressure equations.

Therefore, the pressure equations for the solid-solid cells remain as those presented in [1]:

$$a_{\mathrm{P}} \tilde{p}_{\mathrm{P}}^{n+1} = b_{\mathrm{P}}$$

Since solid-liquid cells are maintained in the system of pressure equations, pressure is calculated in such cells as in the liquid-containing sub-system, enforcing mass conservation. The resulting pressure equations for these cells depend on the amount of liquid-containing neighbors. For example, for the solid-liquid cells with one and two neighbors, the equations remain:

One liquid neighbor:

$$\dot{m}_{f1}^{n+1} = \frac{\dot{m}_{f1}^{p} - \Delta t \nabla p^{n+1} \cdot \hat{n}_{f1} A_{f1}}{(1 + \Delta t S/\rho_l)_{f1}} = V_{\mathrm{P}} \frac{\rho_{m,\mathrm{P}}^{n+1} - \rho_{m,\mathrm{P}}^{n}}{\Delta t} \tag{3.26}$$
$$\Rightarrow a_{\mathrm{P}} \tilde{p}_{\mathrm{P}}^{n+1} + a_{\mathrm{F}_{f1}} \tilde{p}_{\mathrm{F}_{f1}}^{n+1} = b_{\mathrm{P}}$$

Two liquid neighbors:

$$\dot{m}_{f1}^{n+1} + \dot{m}_{f2}^{n+1} = \sum_{f=f1,f2} \frac{\dot{m}_{f}^{p}}{(1 + \Delta t S/\rho_l)_f} - \sum_{f=f1,f2} \frac{\Delta t \nabla p^{n+1} \cdot \hat{n}_f A_f}{(1 + \Delta t S/\rho_l)_f} = V_{\mathrm{P}} \frac{\rho_{m,\mathrm{P}}^{n+1} - \rho_{m,\mathrm{P}}^{n}}{\Delta t} \tag{3.27}$$
$$\Rightarrow a_{\mathrm{P}} \tilde{p}_{\mathrm{P}}^{n+1} + a_{\mathrm{F}_{f1}} \tilde{p}_{\mathrm{F}_{f1}}^{n+1} + a_{\mathrm{F}_{f2}} \tilde{p}_{\mathrm{F}_{f2}}^{n+1} = b_{\mathrm{P}}$$

It can be observed that, if there is no density change between consecutive time steps (i.e. the solid-liquid cell is solid in both), the mass flow through the cell face $f1$ —connecting the solid and liquid-containing cells—resulting from Eq. (3.26) is zero. This means that the resulting pressure in the solid-liquid cell must be such that the mass flow through $f1$ obtained by applying Eq. (3.20) is zero. On the other hand, if there is a change of density between successive time steps (e.g. a completely solid control volume starts to melt), the mass flow through the solid-liquid boundary is not zero anymore. Therefore, this internal boundary condition adapts itself automatically to the density variations.

In the cases of solid-liquid cells with two liquid-containing neighbors, Eq. (3.27) indicates that the mass fluxes through the solid-liquid faces $f1$ and $f2$ are not constrained to be strictly zero even if there is no variation of the density. Only their summation is required to be zero in such case, and therefore, it is possible for the liquid to "trespass" these solid-liquid cells. On the other hand, the cell-centered velocities in these special solid cells are explicitly set to zero, since no liquid is contained in them.

The proposed approach results in a "smoother" velocity field in the proximity of the solid cells, specially where completely liquid and solid cells are in direct contact (without an intermediate interface cell) in zones where the mesh resolution is not high. This can be seen in figure 3.3, showing the velocity vectors of the liquid-containing cells close to solid cells using both approaches, the one proposed in this work and the one imposing an internal solid boundary condition in the same way as in the mesh solid boundaries. It can be observed that in the latter case [fig. 3.3(a)] the velocity vectors are parallel to the faces of the solid cells, while in the former [fig. 3.3(b)] the fluid seems to go through them and the velocity field is less intricate.

Resolution of the linear system of pressure equations

The resulting system of pressure equations has variable coefficients, where two subsystems can be identified: one comprising all the liquid-containing and solid-liquid cells; and another, trivial one, with all the solid-solid cells where the value of pressure is not used.

Since the system of equations is symmetric, a preconditioned Conjugate Gradient (PCG) solver can be used. In order to lower the computations involved in the resolution of this system of equations, the PCG has been modified so as to perform matrix-vector multiplications only in the non-trivial sub-system, excluding the non-resolved solid-solid cells.

3.3.3 Energy

The conservative form (ρh as the calculated variable) of the energy equation is Eq. (3.3), which can be discretized in time as follows:

$$(\rho h)_m^{n+1} = (\rho h)_m^n + \Delta t \left[-\nabla \cdot (\rho_l h_l \vec{u}) + \nabla \cdot (\lambda_m \nabla T) \right]^{n+\alpha} \tag{3.28}$$

were the right hand side would be evaluated somehow depending on the time integration scheme.

It would be preferable to use this approach, since both density and enthalpy could be calculated at the same time. The key here is to be able to define the thermodynamic state from the value of $(\rho h)_m$, i.e. to calculate the rest of the properties (T, λ, etc.) using $(\rho h)_m$ as the independent variable.

However, the usual situation is to have correlations for the properties expressed in terms of T, and furthermore, to have separate correlations for ρ and h (see section 3.2.1). Thus, in order to be able to use ρh to find the rest of the properties, one would have to multiply both correlations and afterwards invert the resulting formula to obtain T from ρh. This is usually a hard task, since could result in having to invert complicated functions.

Therefore, it is useful to be able to calculate only h from the energy equation, while assuming ρ as known. This can be done using the non-conservative form of the energy equation.

Taking into account the conversion:

$$\frac{\partial \rho h_m}{\partial t} = h_m \frac{\partial \rho_m}{\partial t} + \rho_m \frac{\partial h_m}{\partial t}$$

the following non-conservative form is obtained (where the calculated variable is h) from Eq. (3.3):

$$\rho_m \frac{\partial h_m}{\partial t} + \nabla \cdot (\rho_l h_l \vec{u}) = \nabla \cdot (\lambda_m \nabla T) - h_m \frac{\partial \rho_m}{\partial t}$$

and using mass conservation equation (3.1) it results in:

$$\rho_m \frac{\partial h_m}{\partial t} + \nabla \cdot (\rho_l h_l \vec{u}) = \nabla \cdot (\lambda_m \nabla T) + h_m \nabla \cdot (\rho_l \vec{u}) \tag{3.29}$$

Discretizing Eq. (3.29) in time, the following expression is obtained:

$$h_m^{n+1} = h_m^n + \Delta t \left[\frac{-\nabla \cdot (\rho_l h_l \vec{u}) + \nabla \cdot (\lambda_m \nabla T) + h_m \nabla \cdot (\rho_l \vec{u})}{\rho_m} \right]^{n+\alpha} \tag{3.30}$$

Using this equation and those from section 3.2.1, the thermodynamic state of the material can be found.

If there is an interest in using T in the convective term instead of h_l, the conversion $dh = C_p dT$ can be used, which applied into the following non-conservative form of the energy equation:

$$\rho_m \frac{\partial h_m}{\partial t} + \nabla h_l \cdot \rho_l \vec{u} = \nabla \cdot (\lambda_m \nabla T) + (h_m - h_l) \nabla \cdot (\rho_l \vec{u})$$

results in:

$$\rho_m \frac{\partial h_m}{\partial t} + C_{p_l} \nabla T \cdot \rho_l \vec{u} = \nabla \cdot (\lambda_m \nabla T) + (h_m - h_l) \nabla \cdot (\rho_l \vec{u})$$

In order to express the convective term as a divergence, the following identity can be used:

$$C_{p_l} \nabla T \cdot (\rho_l \vec{u}) = C_{p_l} \nabla \cdot (\rho_l \vec{u} T) - C_{p_l} T \nabla \cdot (\rho_l \vec{u})$$

to obtain:

$$\rho_m \frac{\partial h_m}{\partial t} + C_{p_l} \nabla \cdot (\rho_l \vec{u} T) = \nabla \cdot (\lambda_m \nabla T) + (h_m - h_l + C_{p_l} T) \nabla \cdot (\rho_l \vec{u}) \tag{3.31}$$

where there is an extra term in the right hand side of the equation depending on the mass balance in the control volume (which, in general, will be different from zero due to the changes in the density), the total enthalpy and the difference between the liquid enthalpy and the liquid specific heat multiplied by the temperature.

Since h_l appears in the source term, it has to be calculated even if it is not appearing in the advective term. Therefore, not using h_l in the advective term would only be interesting if there is some advantage in terms of computational cost. It is possible that some advantage could be obtained if, for example, the calculation of convective

and diffusive terms is performed at the same time, and using a unique array/vector of values (T) could turn out faster —due to more efficient memory management— than needing two different arrays/vectors (T and h_l).

Discretizing Eq. (3.31) in time, the following expression is obtained:

$$h_m^{n+1} = h_m^n + \Delta t \left[\frac{-C_{p,l}\nabla \cdot (\rho_l \vec{u} T) + \nabla \cdot (\lambda_m \nabla T) + (h_m - h_l + C_{p_l} T)\nabla \cdot (\rho_l \vec{u})}{\rho_m} \right]^{n+\alpha} \tag{3.32}$$

3.4 Definition of the case study

The case study is based on the experimental and numerical results obtained by [15,27], where the melting of a PCM inside a spherical capsule is studied. Figure 3.5 depicts a sketch of the configuration of the case. A spherical glass capsule filled with n-Octadecane, initially in solid state, is immersed into a water bath at 40°C. Since the temperature of the water is higher than the melting point of the PCM, the material close to the capsule shell starts to melt forming a concentric solid-liquid interface. As the melting process evolves, the liquid layer grows and the temperature gradients in the fluid combined with buoyancy forces cause the liquid to move, producing the natural convection phenomenon. This form of heat transfer intensifies the heat transfer rate and modifies the concentrical heat transfer that was enforced by the thermal conduction. Hence, a deformation of the interface is produced, since its evolution is determined by the heat transfer rate.

In [27], experiments of constrained and unconconstrained melting are presented. In unconstrained melting, the solid phase, being denser than the liquid phase, sinks to the bottom of the sphere; while in constrained melting, the solid phase is restrained from sinking. Here, numerical simulations of constrained melting are presented, since the solid phase is assumed to have zero velocity.

Both two and three-dimensional meshes have been used, which were generated with ANSYS ICEM CFD package [28]. Table 3.1 shows the list of meshes used, where a code for each one has been assigned indicating if the mesh is two (2D) or three-dimensional (3D), if it includes or not the upper opening (NO/WO) and the approximate amount of cells. The upper opening was included in the meshes intended to be used for simulating cases with variable density, where the less dense fluid needs to be allowed to escape from the capsule.

In the case of 2D meshes, since a cartesian formulation is used, the geometry used is a slice of sphere with a very small azimuthal angle (see left half of figs. 3.6(a)-3.6(d)). It should be noted that the 2D meshes 2D-NO-7.7E3 and 2D-WO-9.3E3 (without counting the cells of the upper opening) have a similar amount of cells as that claimed

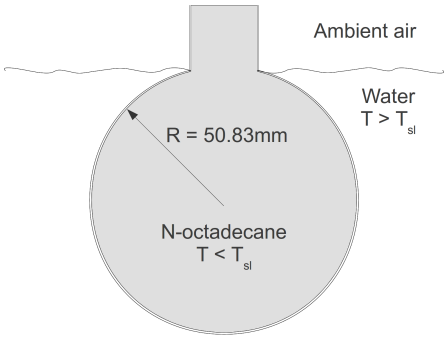

Figure 3.5: Sketch of the case under study

to be used by Tan et al. [15] in their simulations ($\sim$ 7000–8000), while meshes 2D-NO-31E3 and 2D-WO-31E3 have a density of around 4 times higher. 3D meshes 3D-NO-1.4E6 and 3D-WO-1.6E6 present a density of cells for a slice of sphere (similar to the geometry of the 2D meshes used) of around 5000 cells —somewhat lower than 2D-NO-7.7E3 and 2D-WO-9.3E3— while for mesh 3D-WO-5E6 (only used in case C) this value is around 12000.

Table 3.1: Meshes used

Code	Cells	Cells for opening	Prismatic layers	r_{eq}/R	
				Smallest[a]	Biggest[a]
2D-NO-7.7E3	7669	-	-	4.28E-3	3.91E-2
2D-NO-31E3	30670	-	-	2.03E-3	2.03E-2
2D-WO-9.3E3	9257	400	-	2.89E-3	2.03E-2
2D-WO-31E3	31445	400	-	8.56E-4	1.64E-2
3D-NO-1.4E6	1436919	-	10	3.91E-3	1.99E-2
3D-WO-1.6E6	1637607	12700	-	4.79E-3	2.22E-2
3D-WO-5E6	5272390	$\sim$ 40000	-	3.44E-3	9.42E-3

[a]Equivalent radius of the biggest and smallest cells. In 2D meshes, it is equal to the radius of the circle with the same area as the biggest/smallest cell; while in 3D meshes it is equal to the radius of the sphere with the same volume. All values are relative to the radius of the spherical capsule.

3.4.1 Spatial discretization schemes

A central difference scheme has been used for the diffusive terms of both momentum and energy equations. The convective term of momentum equation has been discretized with a symmetry-preserving scheme (SYMMPRES) [29]. This scheme

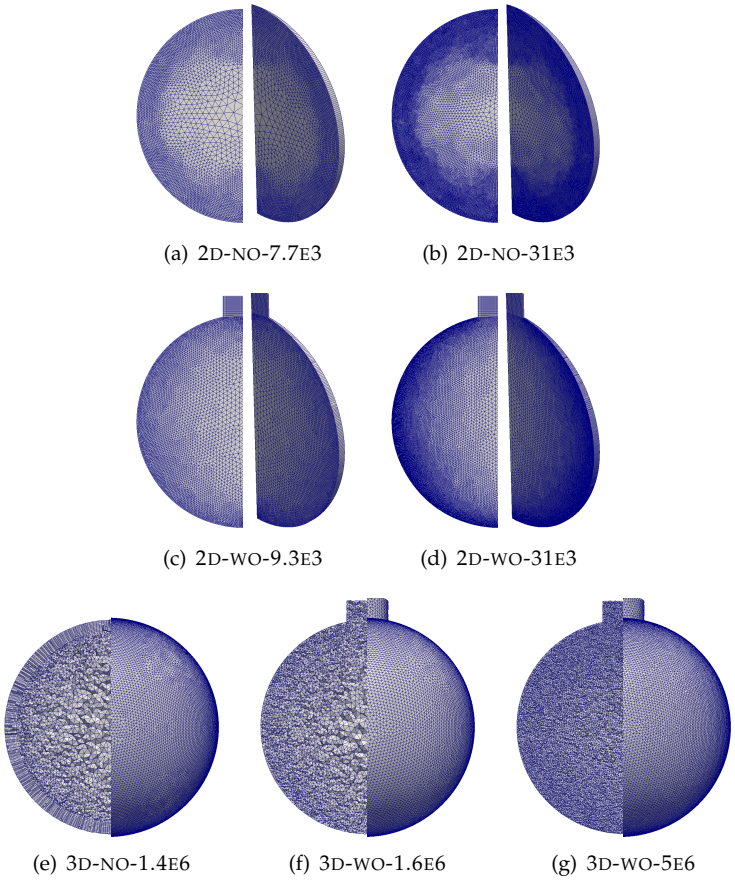

(a) 2D-NO-7.7E3 (b) 2D-NO-31E3

(c) 2D-WO-9.3E3 (d) 2D-WO-31E3

(e) 3D-NO-1.4E6 (f) 3D-WO-1.6E6 (g) 3D-WO-5E6

Figure 3.6: Meshes used. 2D: Left half of images show a front view, while right half show a tilted view. 3D: Left half of images show a front cut view, while right half show the external surface.

considers the scalars in the cell faces as the mean value between the scalars in the cell centers. In uniform meshes its accuracy is of second order, while in unstructured meshes, although locally first order, it has been observed to be of a higher order (between 1 and 2) globally [30].

For the convective term of the energy equation two schemes were tested, a first-order UPWIND and the symmetry preserving scheme. The former has the advantage of avoiding unbounded values of the temperature, while the latter has the property of

presenting a lower numerical diffusion. A comparison between the results obtained with both schemes is carried out in the results section.

3.4.2 Physical properties

Difficulties have been encountered in the search of the physical properties of n-Octadecane near the melting point. Specially for density of the solid phase and thermal conductivity of both phases, as well as for the fusion temperature. Little information, and sometimes, high disagreements between the different sources has been found.

Constant properties

As a first approximation, thermo-physical properties were taken from [15]. The significant quantitative difference between experimental and first numerical results led to the suspicion of being using wrong properties. Therefore, a thorough search for physical properties has been carried out. Very little information has been found for some of them, such as density and thermal conductivity of the solid phase.

Table 3.2 depicts the numerical properties obtained from [15] and those generated using the data found in the literature [31–38].

Table 3.2: Constant physical properties of n-Octadecane

	L $[J\,kg^{-1}]$	ρ $[kg\,m^{-3}]$	C_p $[J\,kg^{-1}\,K^{-1}]$	λ $[W\,m^{-1}\,K^{-1}]$	μ $[Pa\,s]$	β $[K^{-1}]$
From Tan et al. [15]	243500	772	2300	0.1505	3.86 E-3	9.1 E-4
From literature [31–38]	242454	774.5	2225	0.1505	3.57 E-3	9.42 E-4[a]
Proposed in this work (L modified)	270159	774.5	2225	0.1505	3.57 E-3	9.42 E-4[a]

[a] Calculated as $\frac{\rho_l(313.15K)-\rho_l(301.33K)}{774.5\,\frac{kg}{m^3}\,11.82K}$ using the correlation for liquid density from [34].

An important issue to point out is that the value of latent heat adopted in our simulations is not exactly the one found in [31], but a correction of that value considering the fact that the density of the liquid phase is being adopted for both phases. Thus, the value of L is augmented by the ratio between solid and liquid densities (ρ_s/ρ_l) in order to obtain the real latent heat inside each control volume. Therefore,

$$L_{mod} = 242454\frac{\rho_s}{\rho_l} = 270159\,\mathrm{J/kg}; \qquad \text{with: } \rho_s = 863\,\mathrm{kg/m^3} \tag{3.33}$$

If the original value of L were used together with a density equal to that of the liquid phase, less energy than that actually needed would be required to melt the solid contained in the same control volume, and therefore, a faster melting would be obtained. This issue has not been addressed by other authors (e.g. [15, 17]), and has probably been a source of error in their numerical simulations.

In this case, adopting the real latent heat or the modified one results in that around 10% more energy is needed to melt the n-Octadecane contained in the same control volume for the latter case. This is one possible cause for having melting rates higher than those registered in the experiment, by the numerical simulations of Tan et al. [15] and Zhao et al. [17].

Variable properties

In the pursue of accurate thermo-physical properties of n-Octadecane, several works have been consulted (several more than those referred in this work). Discrepancies have been found for some properties between different works. The correlations finally adopted are presented below, along with comments about their accuracy and some other related observations.

- *Melting temperature (T_{sl})*: taken from the experimental work of Messerly et al. [31]. A fixed value of 301.33 K (28.18°C) has been adopted. Several references [32, 39] indicate that n-Octadecane does not present disordered phases between the low temperature ordered solid phase and the liquid phase, resulting in a change of phase at a single temperature. There is some disagreement about this value, and melting points as low as 300.2 K have been reported [33]. Furthermore, it has been seen in the scientific literature (e.g. in [32]) that impurities could modifiy the behaviour of pure n-Octadecane resulting in a modification of the melting temperature and of the latent heat of fusion. It is believed, due to the experimental temperature curves presented in [15] that the material used in the experiments could present a melting temperature range within 27-29°C. This could definitely be a cause of differences between experimental and numerical results. With this in mind, numerical simulations using a melting point of 300.35 K (27.2°C) are also carried out in this work.

- *Latent heat of fusion (L)*: 242454 J/kg, calculated from the liquid and solid enthalpies at 301.33 K indicated in [31]. As mentioned above, this value could be modified by the presence of impurities.

- *Liquid density (ρ_l)*: correlation adopted from [34],

$$\rho_l = 1010.07 - 0.80587\,T + 0.00012463\,T^2$$

where ρ_l is expressed in kg/m^3 and the temperature is in K. The variation of this value in the working range of temperatures is around 1% using the above correlation.

Although the authors of the referred work define a range of validity of their correlation which do not include the temperature range between the melting point and the maximum temperature present in the experiment of Tan et al. [15], comparison with the experimental curve presented in [35] shows a fairly good agreement for this range of temperatures.

- *Liquid viscosity (μ_l)*: correlation adopted from [36],

$$log_{10}\,\mu_l = -11.5505 + \frac{1670.8}{T} + 0.015675\,T - 1.2341 \times 10^{-5}\,T^2$$

where μ_l is expressed in $Pa.s$ and the temperature is in K.

This correlation reproduce almost exactly the experimental values from [40] in the range of temperatures of interest. The variation of this property is not negligible in the working range of temperatures of the liquid phase ($\sim$30%).

- *Liquid thermal conductivity (λ_l)*: linearized correlation from [37],

$$\lambda_l = 0.156427 - 0.0001841779(T - 273.15)$$

where λ_l is expressed in $W/m.K$ and the temperature is in K. The variation of this property in the working range of temperatures, using the above expression, is less than 2%.

Differences of around 5% have been found with those values calculated using the correlation from [36], and higher with respect to [38]. In the latter work, a value of liquid thermal conductivity of 0.18 W/mK (20% higher than that obtained with the present correlation) has been reported at the melting point.

- *Liquid specific heat ($C_{p,l}$)*: linearized correlation from [37],

$$C_{p,l} = 2137.1456 + 2.7186(T - 273.15)$$

where $C_{p,l}$ is expressed in $J/kg.K$ and the temperature is in K. The variation of this property in the working range of temperatures, using the above expression, is less than 2%.

The present correlation agrees very well with the experimental data from [31]. Differences of up to 10% can be found with the values calculated with the correlation from [39], which is seen to underpredict the values in the temperature range between 300 - 320 K.

- *Solid density (ρ_s)*: a value of 863 kg/m^3 has been adopted. There is a high uncertainty in this value, as no exact information has been found. It has been very roughly approximated from the density curve presented in [35].

  There is a significant difference between the densities of the liquid and solid phases. With the values adopted in this work, at the melting point, this difference is of $\sim 11\%$ (with respect to the liquid density).

- *Solid thermal conductivity (λ_s)*: a fixed value of 0.3362 $W/m.K$ has been adopted, calculated from the ratio k_s/k_l presented in [38] and from k_l (at the melting point) determined using the previously indicated correlation. There is high uncertainty in this value as high dispersion has been found between different sources consulted. The authors believe that the ratio $k_s/k_l = 0.45$ is the most accurate value of those found in [38] due to the procedure used for its determination, which do not depend on the density of any of the phases. However, it is believed that there is a somewhat linear variation of this property with the temperature, as seen for other n-alkanes [41]. Unfortunately, no correlation has been found for the n-Octadecane.

  In any case, there is a significant difference between the thermal conductivities of the liquid and solid phases, which could be a source of error in the numerical simulations if not properly taken into account.

- *Solid specific heat ($C_{p,s}$)*: linearized experimental data from [31],

$$C_{p,s} = 1652.9056 + 10.2673(T - 273.15)$$

  The above expression results in a variation of less than 1% of this property in the working range of temperatures for the solid phase. However, there is a significant difference between the specific heats of the solid and liquid phases, which is around 13%.

  The correlation presented in [39] has not been adopted here due to not being very accurate in the temperature range near the melting point, as indicated by the authors.

3.4.3 Initial and boundary conditions

Initial conditions

Initially, all the PCM is in its solid state. However, in order to avoid the formation of liquid cells completely surrounded by solid cells —which would cause divergence, due to the impossibility of the less dense fluid to leave these cells— a liquid film close to the shell has been included in the initial conditions. The width of this layer is around 3% of the radius of the capsule (∼1.5 mm), resulting in an initial total liquid fraction of ∼8.5%, depending on the mesh. Therefore, all numerical simulations in this work are assumed to start in a state corresponding to that of the experiment at t = 12 minutes, which seems to be the time at which liquid fraction is around ∼8.5%, according to the figures presented by [15].

For the liquid film, a temperature equal to the melting point has been adopted. For the solid phase, a uniform temperature of 26.5°C has been assumed, estimated from the experimental temperature curves presented in [15].

Boundary conditions

- *Capsule shell*

  In the numerical results reported by Tan et al. [15], the melting rate was over-predicted when compared to the experimental data. They justified the sources for such discrepancy in the consideration of a constant temperature for the external surface of the capsule shell, when the presence of the base supporting the capsule could be avoiding a good heat transfer in this zone, and furthermore, a thermal stratification could have developed in the water bath. With this in mind, instead of adopting a constant temperature for the outer surface of the capsule, a convection coefficient acting between the water bath and the shell is assumed. In fact, two values of this coefficient are tested, one considering a high heat transfer rate between the water bath and the capsule and another one with a low heat transfer rate.

  Therefore, the capsule shell is represented as a solid, no-slip boundary (see section 3.3.2), with a fixed external temperature (40°C) and an equivalent resistance to the heat transfer (h_{eq}) encompassing thermal convection between the bath and the outer surface and conduction through the glass, respectively. A heat flux into the cell adjacent to the capsule is enforced as:

$$\dot{q}_{sb} = A_{sb} \frac{(T_{wb} - T_P)}{\frac{A_{sb}}{A_{ext} h_{eq}} + \frac{\vec{d_{P,sb}} \cdot \hat{n}_{sb}}{k_f}}$$

where the thermal resistance has been indicated as a sum of external (bath + shell) plus internal (portion of fluid between cell center and solid face) heat transfer resistance. The two values of h_{eq} here adopted are $796\,W/(m^2K)$ and $237\,W/m^2\,K$. The former corresponds to a convective heat transfer between bath and shell of around $3000\,W/m^2\,K$, while the latter corresponds to a convective coefficient of around $300\,W/m^2\,K$. The thickness of the glass capsule shell is 1.5 mm.

Actually, what is really imposed as a thermal boundary condition is the temperature of the boundary face, which is determined in order to give the previous heat flux into the cell, as follows:

$$T_{sb} = \frac{\frac{A_{ext}h_{eq}}{A_{sb}}T_{wb} + \frac{k_f}{\vec{d_{P,sb}}\cdot\hat{n}_{sb}}T_P}{\frac{A_{ext}h_{eq}}{A_{sb}} + \frac{k_f}{\vec{d_{P,sb}}\cdot\hat{n}_{sb}}}$$

- *Upper opening (variable density cases)*

  Fluid flow is allowed to go out from (or into) the capsule through this upper opening. For this, a condition on pressure is applied, resembling a Bernoulli equation, in the form:

$$p_{fb} = p_\infty - \gamma\frac{\rho u^2}{2}$$

  where γ is a coefficient controlling the loss of kinetic energy, which can take values from 0 to 1. In the cases presented, values of $p_\infty = 0$ and $\gamma = 0.5$ have been used. The velocities of the boundary faces are assumed to be equal to those of the corresponding cell nodes.

  For the temperature, in the boundary faces through which the flow goes out from the capsule, a zero derivative has been assumed, taking the value of the cell. For the boundary faces through which the flow comes into the capsule, the temperature of the incoming flow has been assumed to be the mean value (weighted by the mass flow) of the temperature corresponding to the flow going out from the capsule. This results in a zero overall transport of thermal energy through the opening.

  For the lateral surface of the upper opening —which is part of the capsule shell— the same heat flux condition is used as for the rest of the shell, in 2D cases. However, in 3D cases, a further improvement has been introduced by modeling the fact that this part of the shell is in contact with the outer air instead of with the water bath, as it is apparent in the pictures of the experiments presented

in [27]. For this zone, in 3D cases, a value of 5.1 W/m^2 has been adopted for h_{eq} and 25°C for the external (air) temperature.

- *Periodic faces (2D)*

  For carrying out 2D simulations, where axi-symmetry is assumed, the faces of the sphere slices (see 2D meshes from fig. 3.6) should not affect the solution in any way. Therefore, zero derivative has been adopted for all the variables, as well as zero mass flux through the faces. No contribution of these boundary faces is produced over the diffusive, convective or source terms of all the equations.

3.5 Results

Several simulations have been run using the different meshes designed, for two and three-dimensional analyses, as well as using constant and variable thermo-physical set of properties. Since the thermal boundary conditions are not exactly known, two different values have been tested for the equivalent heat transfer coefficient between the water thermal bath and the internal surface of the capsule shell ($h_{eq} = 796\,W/m^2\,K$ and $h_{eq} = 237\,W/m^2\,K$). Furthermore, since the experimental temperature curves observed in [15] indicate that the onset of the phase change may be occurring at a temperature of around 27°C, simulations assuming a melting point of 27.2°C have also been run. Three combinations of thermal boundary condition and melting point are codified as cases A, B and C, as depicted in Table 3.3.

Table 3.3: Cases run using different combinations of boundary conditions and melting point

Code	h_{eq} ($W/m^2\,K$)	T_{sl} (°C)
A	796	28.18
B	237	28.18
C	237	27.2

Comparison is performed between simulations using UPWIND and SYMMPRES convective schemes, two and three-dimensional meshes and constant and variable properties. Agreement with experimental results is also addressed.

3.5.1 Convective scheme and grid convergence

As indicated in section 3.4.1, two schemes have been adopted for the discretization of the convective term of the energy equation, first-order UPWIND and SYMMPRES.

Figure 3.7 show results of evolution of global liquid fraction for the different cases using each convective scheme. A better match with experimental results is observed in the results using the symmetry preserving scheme. Furthermore, the discrepancy between results with different meshes is higher in the cases using the UPWIND scheme, indicating a worse grid convergence. The differences between results using constant and variable properties are also higher in the cases where the UPWIND scheme was adopted.

All these observations indicate that the numerical diffusion is affecting the cases were the UPWIND scheme was used and that the symmetry preserving scheme seem to give more accurate results. Unbounded values of temperature has been observed at some specific locations in the SYMMPRES cases, but this problem do not seem to affect the results as much as the numerical diffusion produced by the UPWIND scheme. For this reason, the results presented in the following sections correspond to the simulations using the SYMMPRES scheme.

As the mesh density is increased, the melting rate tends to decrease. This behavior is observed for all the combinations of properties and boundary conditions tested. With the meshes used, it cannot be stated that grid convergence has been reached, although the results obtained with the SYMMPRES cases show a quite low disparity between them.

3.5.2 Thermo-physical properties

As indicated in section 3.4.2, when defining the constant thermo-physical properties used representative of the material in the working conditions, a modification to the latent heat was performed in order to correct the error in total energy; which comes from the fact of not considering the difference in density between liquid and solid phases.

Figure 3.8 shows the difference in liquid fraction evolution between three 2D simulations of case A, using different set of properties. For the first, constant properties shown in Table 3.2, without the modification of L, were adopted. In the second, constant properties with the modified L were used. In the third, different densities and specific heats for liquid and solid phases are adopted (and therefore a mesh with the upper opening is used for allowing fluid escaping from the shell) but with the rest of the properties constant. $\rho = 863\,kg/m^3$ and $C_p = 1940 J/kgK^{-1}$ were used for the solid phase. Both simulations using constant properties were run with the same mesh, while for the other a mesh with a similar amount of cells was adopted.

It can be observed how the melting rate in the case with the unmodified L is

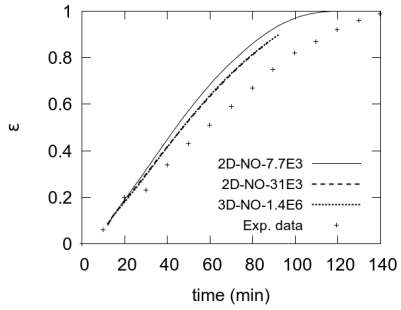

(a) Case A. Constant properties. UPWIND.

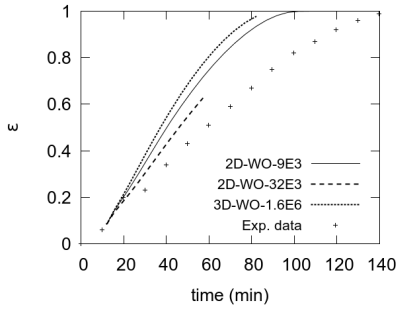

(b) Case A. Variable properties. UPWIND.

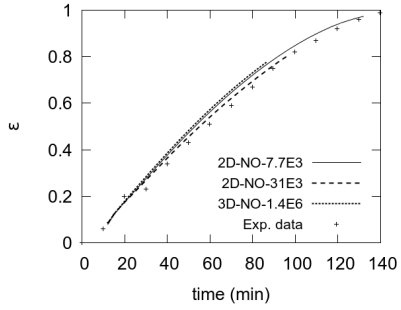

(c) Case A. Constant properties. SYMMPRES.

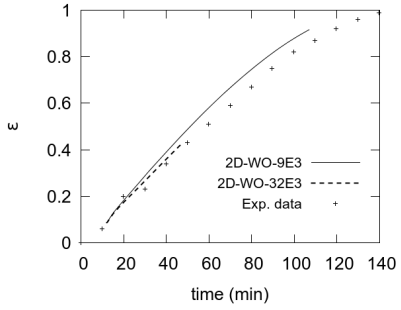

(d) Case A. Variable properties. SYMMPRES.

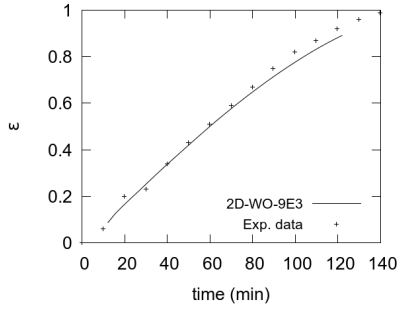

(e) Case B. Variable properties. SYMMPRES.

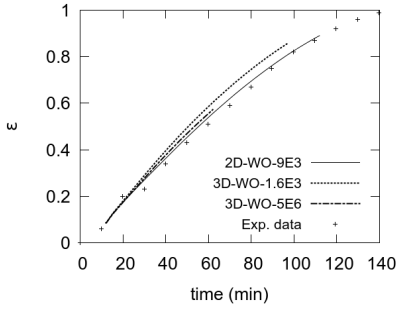

(f) Case C. Variable properties. SYMMPRES.

Figure 3.7: Global volumetric liquid fraction vs. time for the different cases with 2D and 3D meshes, using upwind or symmetry preserving schemes.

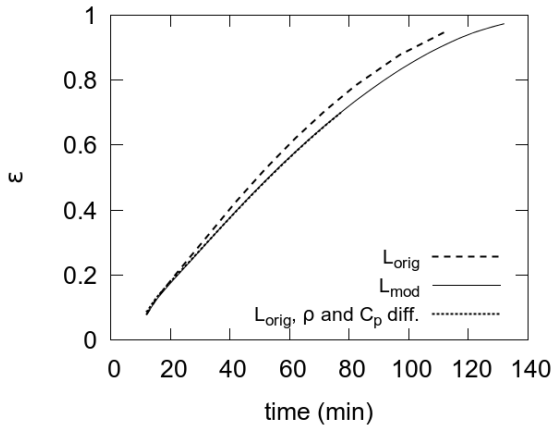

Figure 3.8: Numerical results of the evolution of global ϵ with time for case A. L_{orig}: constant properties, unmodified value of L; mesh: 2D-NO-7.7E3. L_{mod}: constant properties, modified value of L; mesh: 2D-NO-7.7E3. L_{orig}, ρ and C_p diff.: different densities and specific heats for liquid and solid phases with the rest of the properties constant; mesh: 2D-WO-9E3.

higher than for the other two cases. The case with constant properties and modified L evolves almost exactly as the one where the differences in ρ and C_p are considered. These observations indicate that the density scaling of L compensates the fact of using the liquid density for both phases, and that the effect of the expansion in the melting is not very significant for this case.

Furthermore, plots of the evolution of the global liquid fraction of two 2D simulations, one using constant properties and another taking full account of the properties variations with temperature, are depicted in figure 3.9. It is observed that considering the change of properties with temperature result in a slight increase of the melting rate. Further analysis, after running several simulations changing the property for which the variations with temperature are accounted for, seem to indicate that the property whose variation is affecting the melting rate the most is the thermal conductivity, and specially that of the liquid phase.

3.5.3 2D vs. 3D

Figures 3.10 and 3.11 show the temperature and liquid fraction maps, as well as the streamlines of 2D and 3D simulations for two different moments corresponding to the experiment after t$\sim$22 and t$\sim$47 minutes, respectively. Results shown correspond to

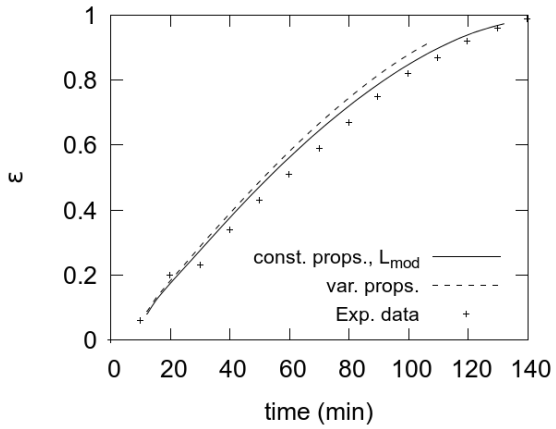

Figure 3.9: Numerical results of the evolution of global ϵ with time for case A using constant and variable properties. Simulation with constant, modified, properties (solid line) was run using mesh 2D-NO-7.7E3, while the one with variable properties (dashed line) was run with mesh 2D-WO-9E3.

meshes with a similar density (comparing the 2D mesh with a slice of the 3D mesh) in order to evaluate only the effect of assuming (or not) the hypothesis of axi-symmetric behaviour.

The common feature in two and three-dimensional results is the upgoing hot flow close to the shell and downgoing cold flow close to the solid, produced by the gravity force in combination with a decrease of density in the liquid as its temperature increases. However, there are differences between the flow patterns encountered in 2D and 3D cases.

In the bottom, due to the unstable thermal layer (hot shell below cold solid), the flow has a highly 3D behaviour. While in 2D cases the fluid eddies formed at the bottom are "trapped" by the fluid eddies located at the top/middle of the capsule (see 2D streamlines in figs. 3.10 and 3.11), in 3D cases the high velocity flows generated at the bottom "find their way" to the top flowing close to the shell (where the temperature is higher), through some periodically arranged azimuthal angles which alternate with those angles through which the cold fluid flows downwards (closer to the solid, cold, phase). Therefore, upward and downward flows show higher and lower velocities in alternate azimuthal angles, as seen in Fig. 3.12. Also in this figure it can be observed how the interface is modified due to this phenomenon. Figure 3.13 shows some temperature maps of the capsule shell, seen from below, where the alternating zones of higher and lower temperatures can be observed. This

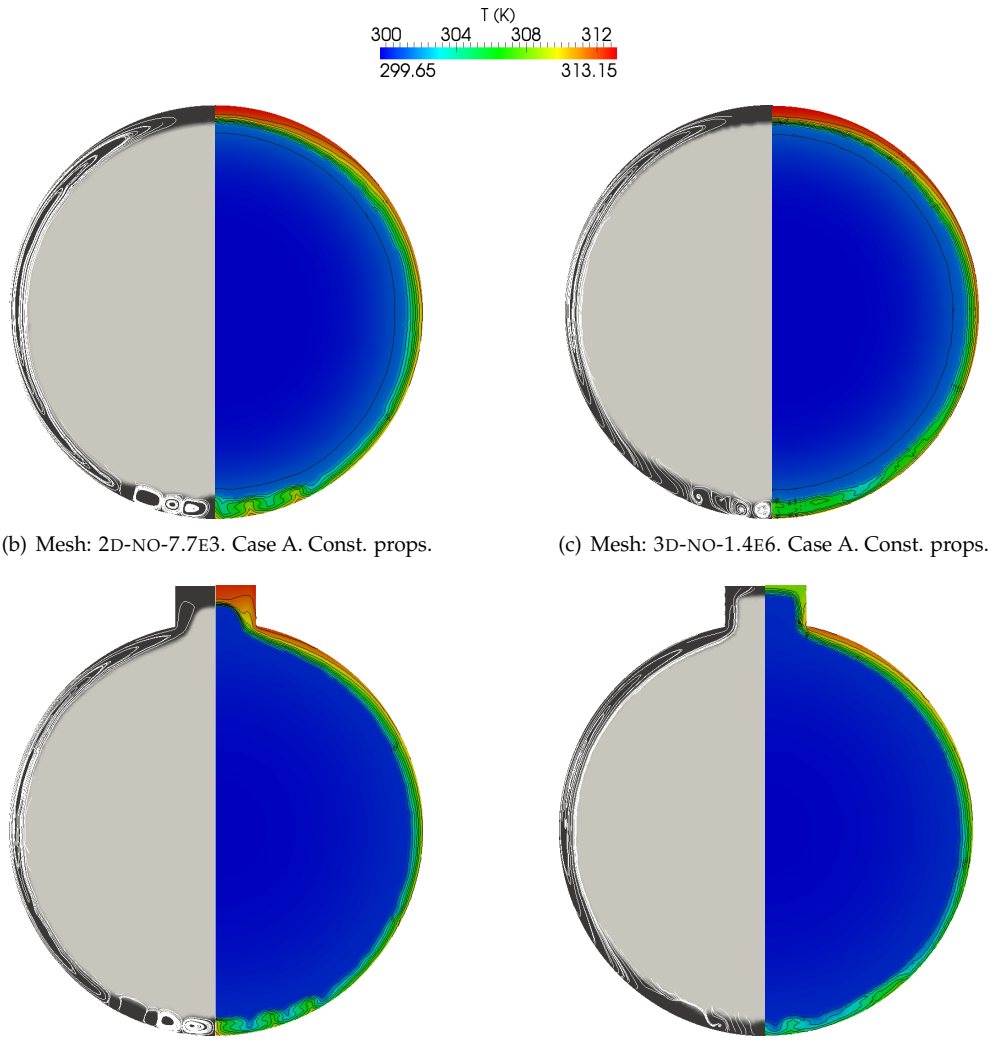

(b) Mesh: 2D-NO-7.7E3. Case A. Const. props.

(c) Mesh: 3D-NO-1.4E6. Case A. Const. props.

(d) Mesh: 2D-WO-9.3E3. Case C. Var. props.

(e) Mesh: 3D-WO-5E6. Case C. Var. props.

Figure 3.10: Vertical cross view of numerical results for 10 min of simulation (t∼22 min in the experiment). The left half of each picture shows a map of liquid fraction (light: solid; dark: liquid) with the flow streamlines, while the right half shows temperature map and contours. The density of the 3D mesh slices and 2D meshes shown are similar.

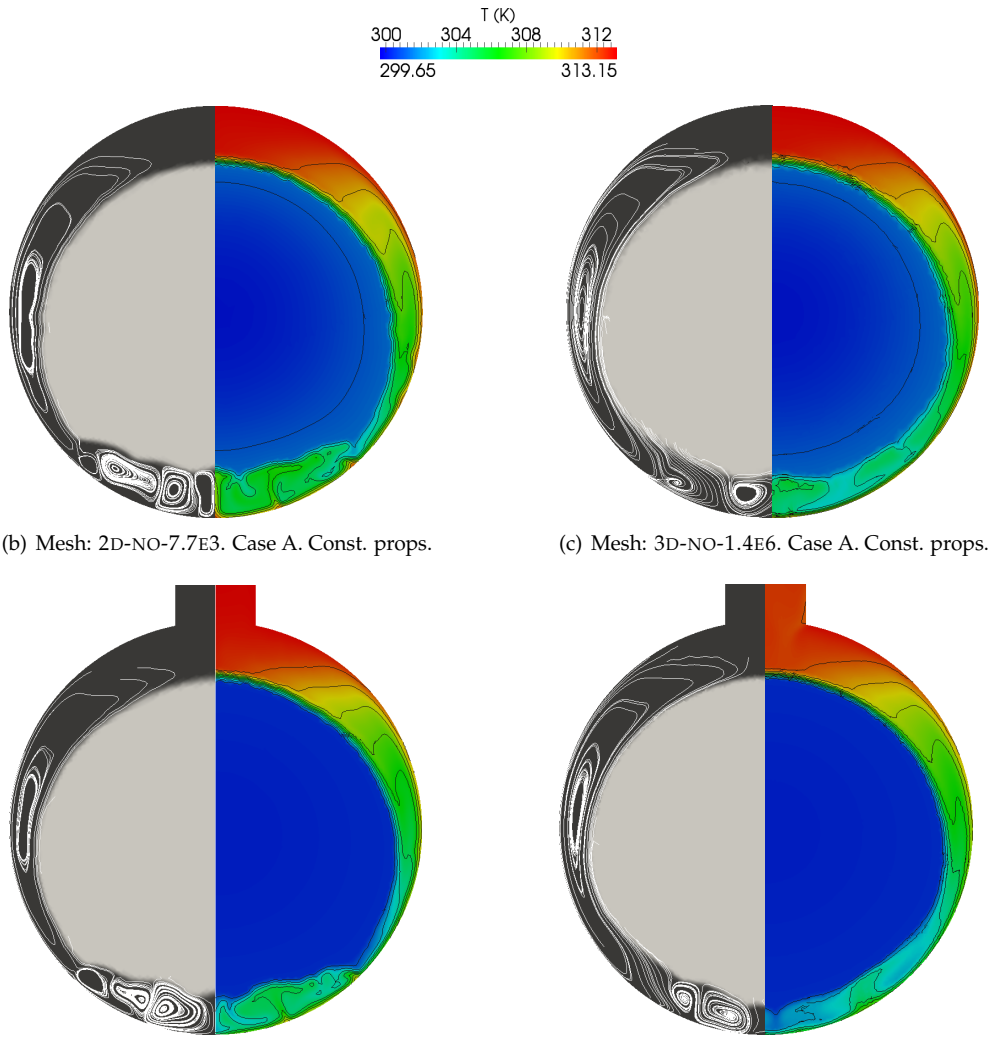

(b) Mesh: 2D-NO-7.7E3. Case A. Const. props.

(c) Mesh: 3D-NO-1.4E6. Case A. Const. props.

(d) Mesh: 2D-WO-9.3E3. Case C. Var. props.

(e) Mesh: 3D-WO-5E6. Case C. Var. props.

Figure 3.11: Vertical cross view of numerical results for $t_{exp} \sim 47$ min. The left half of each picture shows a map of liquid fraction (light: solid; dark: liquid) with the flow streamlines, while the right half shows temperature map and contours. The density of the 3D mesh slices and 2D meshes shown are similar.

effect is present at the bottom of the capsule but not at the top, where a thermal stratification is seen (nearly horizontally uniform temperature distribution) and the velocities are lower. In this figure it can also be noted that in case A the shell is hotter than in case C, due to the higher heat transfer rate assumed for the former.

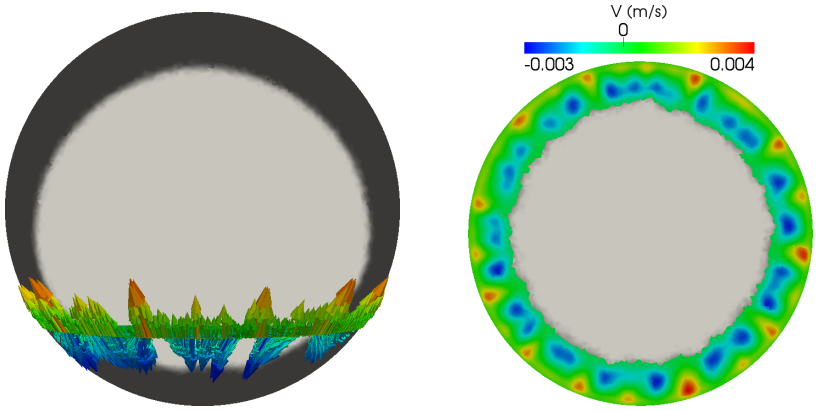

(a) Front view (b) Top view

Figure 3.12: Different views of slice cuts run with mesh 3D-NO-1.4E6 at $t_{exp} \sim 47$ minutes (case A, const. props.). The horizontal cut is at 3 cm below the center of the sphere. Velocity vectors are shown in the front view, while a vertical velocity map is depicted in the top view of the horizontal cut. The greyscale indicates the phase (dark: liquid; light: solid), while the colors indicate the magnitude of the vertical component of the velocity.

A consequence of the "artificial" trapping of the eddies in the 2D cases is that the lower part melts faster in these than in the 3D cases. This can be observed, not only by comparing the shapes of the interface, but also the evolution of the temperature at different axial positions, as shown in figs. 3.14-3.15. In the experimental results of Tan et al. [15], the thermocouple located at point G ($y = 2.5\,cm$ above the center) detects that melting there starts before than at point B ($y = 3.75\,cm$ below the center). In all 2D numerical results reported in this work, as well as in those published by [15] (numerical, 2D), point B starts melting long before point G. However, in 3D cases, melting of point B is much delayed, resulting in a better agreement with experimental data.

Regarding the evolution of global liquid fraction, it is not clear if 3D simulations result in different melting rates. Results using the SYMMPRES scheme (Figs. 3.7(c) and 3.7(f)) seem to indicate that 3D simulations present slightly higher melting rates, but the discrepancies with 2D results are so small that could be due to differences in

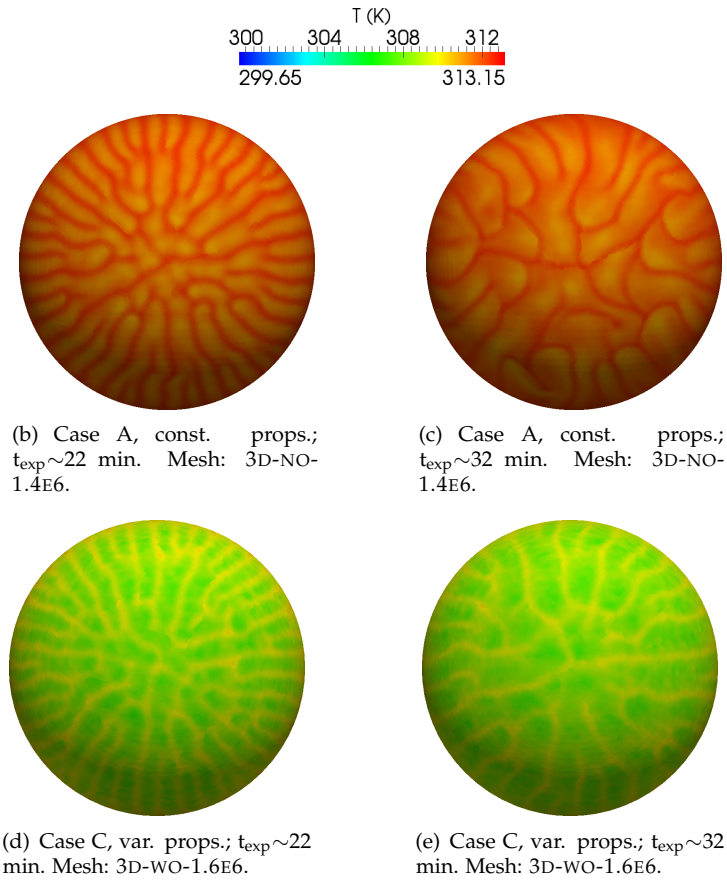

(b) Case A, const. props.; t_{exp}∼22 min. Mesh: 3D-NO-1.4E6.

(c) Case A, const. props.; t_{exp}∼32 min. Mesh: 3D-NO-1.4E6.

(d) Case C, var. props.; t_{exp}∼22 min. Mesh: 3D-WO-1.6E6.

(e) Case C, var. props.; t_{exp}∼32 min. Mesh: 3D-WO-1.6E6.

Figure 3.13: Bottom view of temperature maps in the shell, for 3D simulations.

the used meshes.

3.5.4 Agreement between experimental and numerical results

All the numerical results reproduce very well the qualitative behavior observed in the experiment. Furthermore, a very good accordance in the evolution of the melting rate is obtained for the numerical results with both 2D and 3D meshes using the SYMMPRES scheme.

Figures 3.14-3.16 show higher temperature oscillations at locations below the center of the sphere for the numerical results, than those observed in the experimental

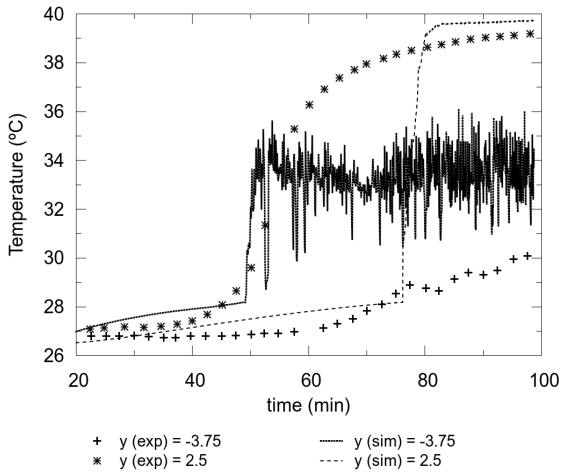

(a) Mesh: 2D-NO-31E3

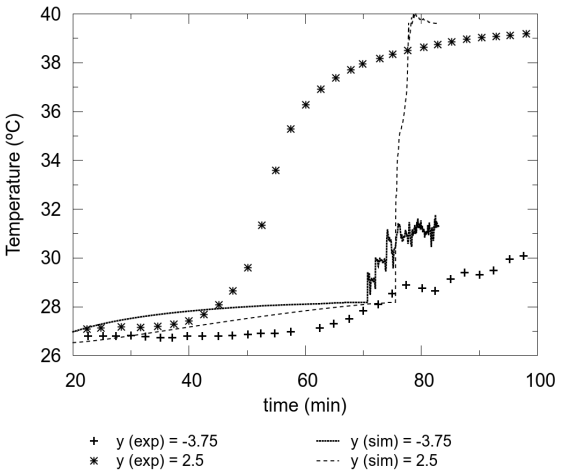

(b) Mesh: 3D-NO-1.4E6

Figure 3.14: Evolution of T vs. time, for numerical and experimental results (extracted from [15]), at two different locations of the vertical axis (indicated in cm, with $y = 0$ being the center of the capsule). Case A, using constant properties.

data. This is possibly indicating that velocities higher than those of the experiment

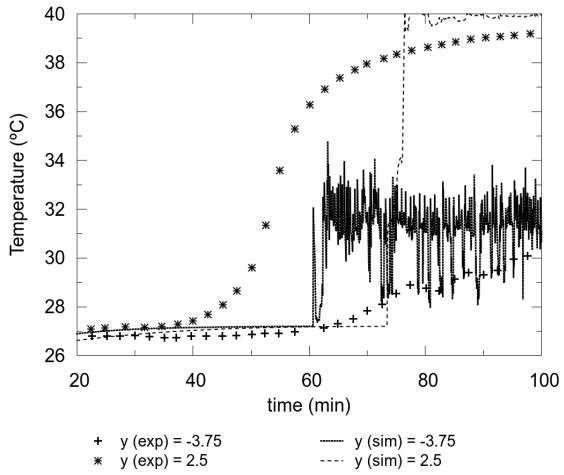

(a) Mesh: 2D-WO-9E3

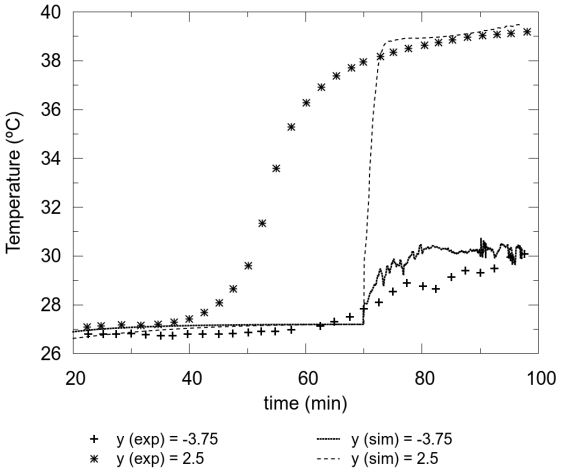

(b) Mesh: 3D-WO-1.6E6

Figure 3.15: Evolution of T vs. time, for numerical and experimental results (extracted from [15]), at two different locations of the vertical axis (indicated in cm, with $y = 0$ being the center of the capsule). Case C, using variable properties.

may be being predicted in the simulations. This is specially true for 2D cases, where

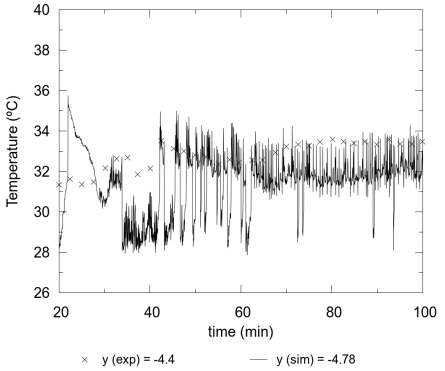

(a) Mesh: 2D-WO-9E3

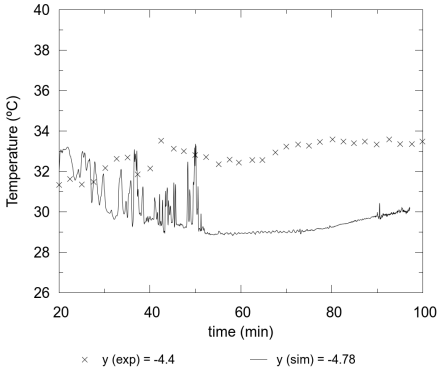

(b) Mesh: 3D-WO-1.6E6

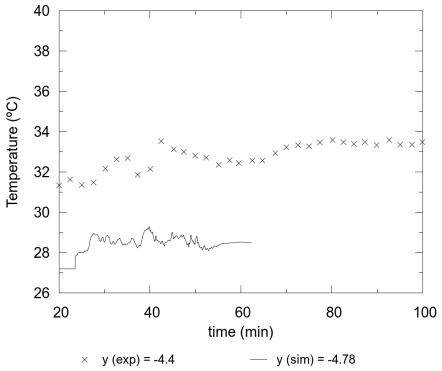

(c) Mesh: 3D-WO-5E6

Figure 3.16: Evolution of T vs. time, for numerical and experimental results (extracted from [15]), at a location in the axis close to the bottom of the capsule. Case C, using variable properties.

the high velocity flows generated at the bottom cannot escape to the top of the capsule, causing higher thermal oscillations in this zone. Furthermore, it is believed that the onset of the phase change in the experiment is produced at a lower temperature than that found in the literature (28.18°C), and may be occurring in a temperature range of around 27-29°C. This would explain that the experimental temperature curves stay nearly horizontal around 27°C and rise more "smoothly" than in the numerical results. By adopting a melting point of 27.2°C (case C), the temperature evolution of the solid phase is better predicted, but the increase after melting is still much higher

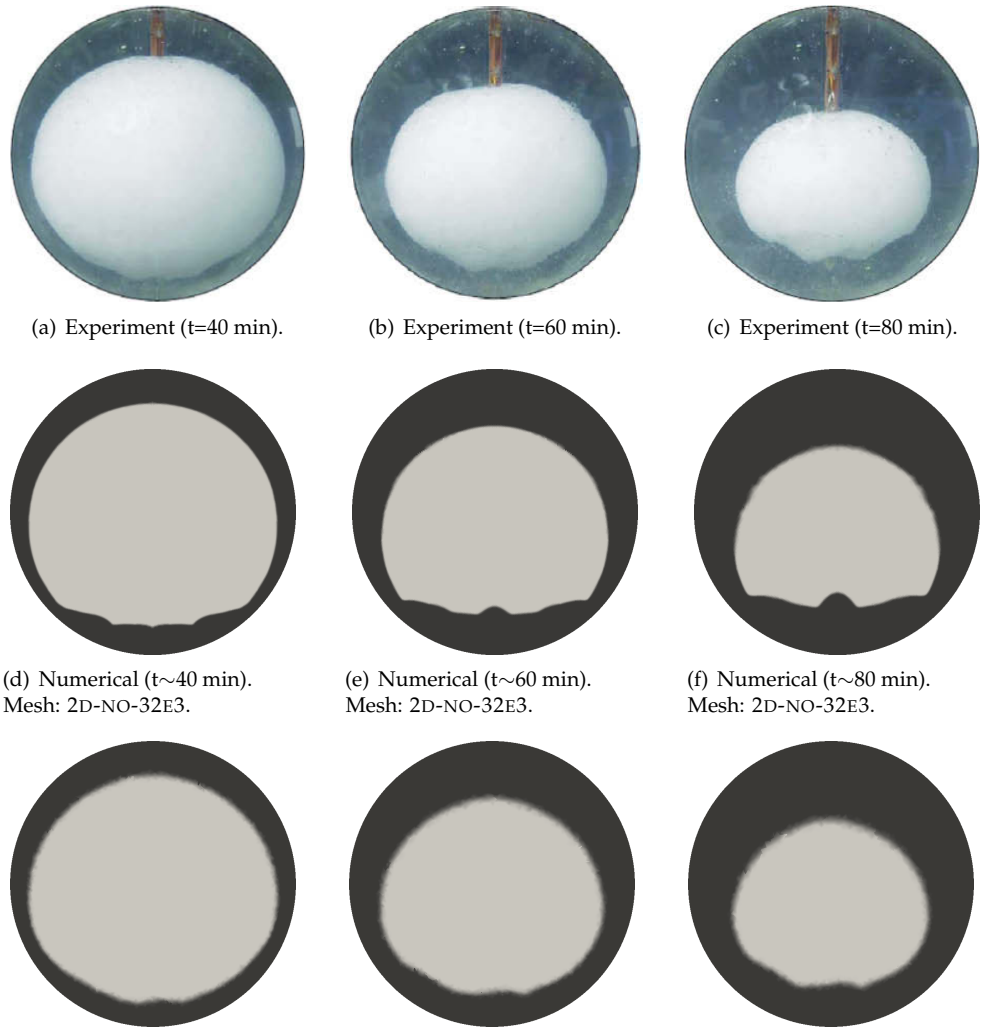

(a) Experiment (t=40 min). (b) Experiment (t=60 min). (c) Experiment (t=80 min).

(d) Numerical (t∼40 min). Mesh: 2D-NO-32E3. (e) Numerical (t∼60 min). Mesh: 2D-NO-32E3. (f) Numerical (t∼80 min). Mesh: 2D-NO-32E3.

(g) Numerical (t∼40 min). Mesh: 3D-NO-1.4E6. (h) Numerical (t∼60 min). Mesh: 3D-NO-1.4E6. (i) Numerical (t∼80 min). Mesh: 3D-NO-1.4E6.

Figure 3.17: Experimental photographs at $t_{exp} = 40$, 60 and 80 minutes (Reprinted from [15] with permission from Elsevier) and our numerical results for case A, using constant properties, with 2D and 3D meshes. Liquid fraction map (dark: liquid; light: solid) is shown for the numerical results.

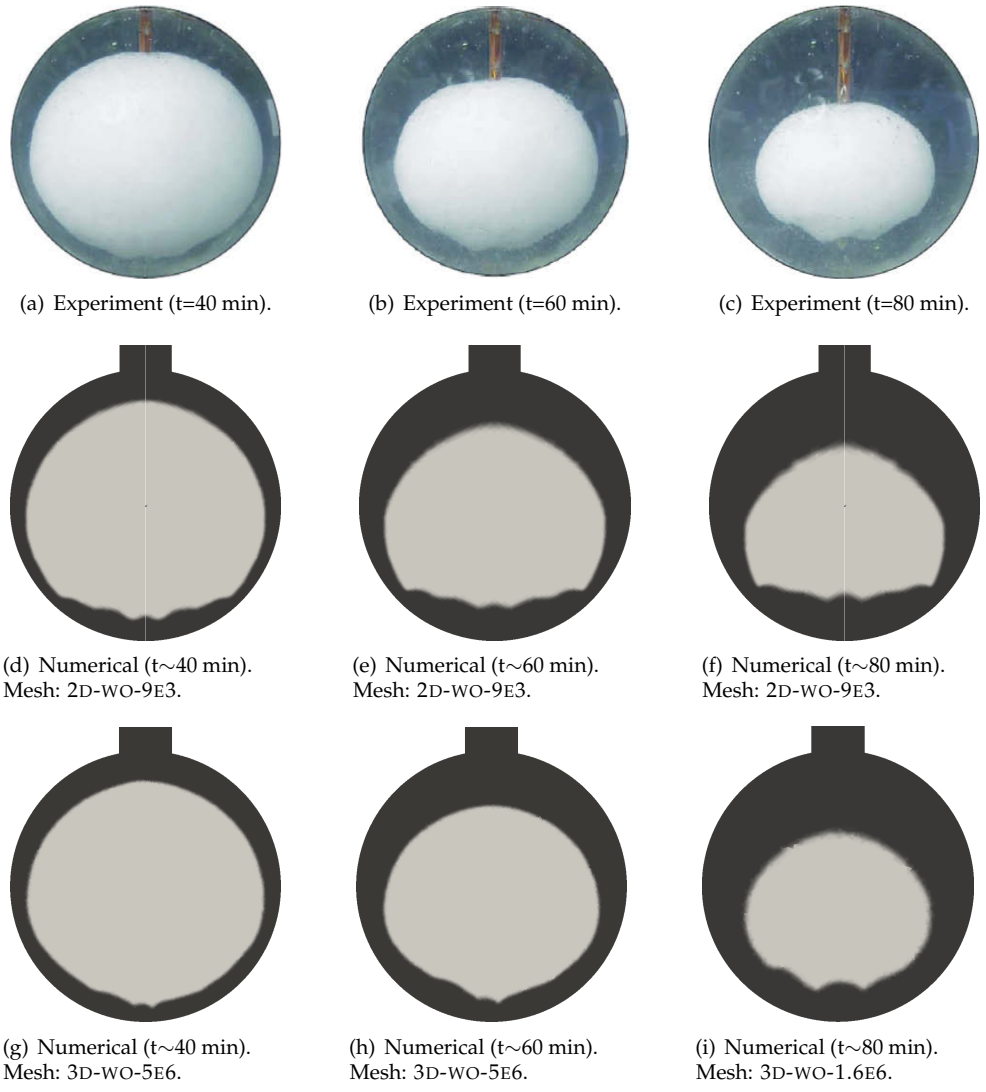

(a) Experiment (t=40 min). (b) Experiment (t=60 min). (c) Experiment (t=80 min).

(d) Numerical (t∼40 min). Mesh: 2D-WO-9E3. (e) Numerical (t∼60 min). Mesh: 2D-WO-9E3. (f) Numerical (t∼80 min). Mesh: 2D-WO-9E3.

(g) Numerical (t∼40 min). Mesh: 3D-WO-5E6. (h) Numerical (t∼60 min). Mesh: 3D-WO-5E6. (i) Numerical (t∼80 min). Mesh: 3D-WO-1.6E6.

Figure 3.18: Experimental photographs at $t_{exp} = 40$, 60 and 80 minutes (Reprinted from [15] with permission from Elsevier) and our numerical results for case C, using variable properties, with 2D and 3D meshes. Liquid fraction map (dark: liquid; light: solid) is shown for the numerical results.

than in the experiment. In 3D results of case C with the densest mesh (3D-WO-5E6, Fig. 3.16(c)), the amplitude of the temperature oscillations at position A is very similar to the observed in the experimental data, and lower than the obtained with the coarser 3D mesh (3D-WO-5E6, Fig. 3.16(b)). However, the predicted mean value is somewhat lower in both cases, which may be another indication of the presence of solid phase at a temperature higher than the assumed melting point.

In figures 3.17 and 3.18, the interface shapes at different instants for both experimental and numerical results are presented. A very good agreement with the experiment is observed in general for the 3D simulations, specially for those using variable properties; while the effect of eddy trapping (mentioned above) produce a higher disagreement in 2D cases.

Regarding the thermal boundary condition, it is difficult to draw clear conclusions about which of both values of h_{eq} is more accurate. Observing global liquid fraction curves for case A ($h_{eq} = 796\,W/m^2\,K$ and $T_{sl} = 28.2$°C) with both constant and variable properties, and comparing the results obtained with 2D meshes of similar amount of cells (2D-NO-7.7E3 and 2D-WO-9E3), it is apparent that the melting rate is overpredicted with respect to the experimental data, specially if the variation of the thermo-physical properties is taken into account. However, in simulations using denser 2D meshes, it is observed that for both constant and variable properties the melting rate obtained is very close to that of the experiment (Figs. 3.7(c) and 3.7(d)). On the other hand, for a melting point of 28.2°C, the value of $h_{eq} = 237W/m^2\,K$ (case B) underpredict the real melting rate (see 3.7(e)).

For 3D simulations of case C (with the lower melting point, variable properties and $h_{eq} = 237\,W/m^2\,K$), the predicted melting rate is still somewhat higher than experimental, even for the densest mesh (3D-WO-5E6). Here, the higher difference between the water bath temperature and the melting point is expected to result in stronger convection than in case A, and thus, in higher melting rates for the same value of h_{eq}. This could explain the very good results obtained with the lower h_{eq}.

In the belief that the material used in the experiment undergoes a phase change at a temperature range, it is possible that the solid phase is still present at temperatures higher than 28°C. Therefore, it is possible that the convection is not as strong as that resulting from the phase transition at a fixed melting point of 27.2°C, and thus, the higher value of h_{eq} is believed to be more accurate. Nevertheless, when comparing the melting rates of cases A and B with the same mesh 2D-WO-9E3, a difference of around 15-20% is obtained, which is not much, considering that h_{eq} for case A is three times higher than for case B.

With the use of an accurate melting temperature range, as well as more accurate boundary conditions, three-dimensional numerical simulations would most probably be even closer to experimental results. Regarding thermo-physical properties, of special importance in this case is to have a more accurate value of the solid phase

density, since it affects the total amount of latent energy initially contained in the capsule. It also affects the expansion in the melting, although this phenomenon has not been seen to influence the melting rate significantly in this case.

3.6 Conclusions

A fixed-grid enthalpy model for unstructured grids using explicit time integration where the thermo-physical properties are variable and dependent on the temperature, has been developed and implemented in a numerical code. The formulation and algorithms for determining the temperature and liquid fraction (or porosity) from the total enthalpy, for phase change occurring at a fixed temperature or in a temperature range, have been described. Modifications of the model presented in [1], regarding different aspects such as the treatment of the conservation equations taking into account the thermal expansion/contraction, the approach for decoupling the pressure of solid and liquid-containing domains and the determination of the source term coefficient introduced by the porous medium approach, have been detailed. Furthermore, different possibilities for the discretization of the energy equation have been discussed.

With the intention of accurately simulating the case of melting of n-Octadecane inside a spherical capsule taking into consideration both accurate constant properties as well as their variation with the temperature, a thorough search for thermo-physical properties has been performed. The correlations used have been presented, indicating their origin and accuracy (either quantitatively or qualitatively). Furthermore, it is indicated how in cases where the density differences between liquid and solid phases is not accounted for, the latent heat should be modified in order to obtain the same amount of total enthalpy inside the same control volume.

Several two and three-dimensional simulations of the case study have been performed. The discretization of the convective scheme of the energy equation has been observed to affect considerably the results, for which the symmetry preserving scheme seem to give more accurate results than the first-order UPWIND scheme. From the comparison between 2D and 3D results, significant differences have been encountered in the flow patterns developed, originated in the unstable thermal zone in the bottom of the capsule. These different flow structures result in different melting rates in the bottom zone near the axis of symmetry, although the evolution of global liquid fraction does not appear to be significantly different between 2D and 3D simulations. Comparison against experimental results allow to state that the agreement obtained with the 3D simulations is higher than with those assuming axi-symmetry (2D).

Regarding the thermo-physical properties used, it has been shown that when using the liquid density for both phases, scaling the latent heat with the density ratio

(solid/liquid) compensate for the error in the total energy per unit volume needed for producing the melting, and more accurate results of the evolution of global liquid fraction are obtained. Furthermore, it is observed that accounting for the full variation of the properties with the temperature results in slightly higher convective fluxes and overall faster melting, which has been seen to be mostly due to the change in the thermal conductivity.

On the other hand, it is apparent from the experimental curves of temperature evolution at some locations, that the material undergoes a phase-change in a range of temperatures instead of at a fixed melting point, which can be a cause of discrepancy between experimental and numerical results.

Another source of discrepancy is the thermal boundary condition in the capsule shell, which in this work has been treated as an equivalent heat transfer coefficient between the thermal bath and the internal surface of the shell and a fixed temperature for the thermal bath. Two different values for this coefficient have been tested. The highest of both resulted in melting rates closer to the experiment in the cases where a melting point of 28.2°C was assumed, while the lowest resulted in better agreement for the cases with a melting point of 27.2°C. Since it is apparent that the solid phase may still be present at temperatures higher than 28.2°C, it is believed that simulations considering the phase change temperature range, may be closer to the experimental results if a heat transfer coefficient closer to the highest of both is used. Nevertheless, it is observed that the difference in the melting rates obtained with one or another value for the same mesh, are much less significant than the difference between them.

Overall, a good agreement between experiment and numerical results is observed, specially for 3D simulations taking into account the variation of thermo-physical properties with the temperature. Results obtained in the present work are closer to the experimental results than those presented by other authors [15, 17].

Acknowledgements

This work has been financially supported by the *Ministerio de Economía y Competitividad, Secretaría de Estado de Investigación, Desarrollo e Innovación*, Spain (ENE-2011-28699), by Termo Fluids S.L., by the Secretaria d'Universitats i Recerca (SUR) del Departament d'Economia i Coneixement (ECO) de la Generalitat de Catalunya and by the European Social Fund.

References

[1] P. Galione, O. Lehmkuhl, J. Rigola, and A. Oliva, "Fixed-grid modeling of solid-liquid phase change in unstructured meshes using explicit time schemes," *Numer.*

Heat Tr. B-Fund., vol. 65, pp. 27–52, 2014.

[2] M. Liu, W. Saman, and F. Bruno, "Review on storage materials and thermal performance enhancement techniques for high temperature phase change thermal storage systems," *Renew. Sust. Energ. Rev.*, vol. 16, pp. 2118–2132, 2012.

[3] W. Steinmann and R. Tamme, "Latent heat storage for solar steam systems," *J. Sol. Energ.-T. ASME*, vol. 130, pp. 011004–1–011004–5, 2008.

[4] H. Michels and R. Pitz-Paal, "Cascaded latent heat storage for parabolic trough solar power plants," *Sol. Energy*, vol. 81, pp. 829–837, 2007.

[5] S. Jegadheeswaran and S. D. Pohekar, "Performance enhancement in latent heat thermal storage system: A review," *Renew. Sust. Energ. Rev.*, vol. 13, pp. 2225–2244, 2009.

[6] K. A. R. Ismail and R. Stuginsky Jr., "A parametric study on possible fixed bed models for pcm and sensible heat storage," *Appl. Therm. Eng.*, vol. 19, pp. 757–788, 1999.

[7] J. P. Bédécarrats, J. Castaing-Lasvignottes, F. Strub, and J. P. Dumas, "Study of a phase change energy storage using spherical capsules. Part II: Numerical modelling," *Energ. Convers. Manage.*, vol. 50, pp. 2537–2546, 2009.

[8] S. M. Flueckiger and S. V. Garimella, "Latent heat augmentation of thermocline energy storage for concentrating solar power —A system-level assessment," *Appl. Energ.*, vol. 116, pp. 278–287, 2014.

[9] C. J. Ho and V. R., "Heat transfer during melting from an isothermal vertical wall," *J. Heat Trans.-T. ASME*, vol. 106, pp. 12–19, 1984.

[10] F. Wolff and R. Viskanta, "Melting of a pure metal from a vertical wall," *Exp. Heat Transfer*, vol. 1, pp. 17–30, 1987.

[11] R. Viswanath and Y. Jaluria, "A comparison of different solution methodologies for melting and solidification problems in enclosures," *Numer. Heat Tr. B-Fund.*, vol. 24, pp. 77–105, 1993.

[12] V. Voller and C. Prakash, "A fixed grid numerical modelling methodology for convection-diffusion mushy region phase change problems," *Int. J. Heat Mass Tran.*, vol. 30, pp. 1709–1719, 1987.

[13] H. S. Udaykumar, R. Mittal, and W. Shyy, "Computation of solid-liquid phase fronts in the sharp interface limit on fixed grids," *J. Comput. Phys.*, vol. 153, pp. 535–574, 1999.

[14] A. D. Brent, V. R. Voller, and K. J. Reid, "Enthalpy-porosity technique for modelling convection-diffusion phase change: Application to the melting of a pure metal," *Numer. Heat Transfer*, vol. 13, pp. 297–318, 1988.

[15] F. L. Tan, S. F. Hosseinizadeh, J. M. Khodadadi, and L. Fan, "Experimental and computational study of constrained melting of phase change materials (PCM) inside a spherical capsule," *Int. J. Heat Mass Tran.*, vol. 52, pp. 3464–3472, 2009.

[16] E. Assis, L. Katsman, G. Ziskind, and R. Letan, "Numerical and experimental study of melting in a spherical shell," *Int. J. Heat Mass Tran.*, vol. 50, pp. 1790–1804, 2007.

[17] W. Zhao, Elmozughi, A.F., A. Oztekin, and S. Neti, "Heat transfer analysis of encapsulated phase change material for thermal energy storage," *Int. J. Heat Mass Tran.*, no. 63, pp. 323–335, 2013.

[18] A. Elmozughi, L. Solomon, A. Oztekin, and S. Neti, "Encapsulated phase change material for high temperature thermal energy storage â Heat transfer analysis," *Int. J. Heat Mass Tran.*, vol. 215, no. 2, pp. 465–484, 2006.

[19] D. A. Nield and A. Bejan, *Convection in Porous Media*, ch. 1. Springer, 3 ed., 2006.

[20] W. Rohsenow, J. Hartnett, and Y. Cho, *Handbook of Heat Transfer*, ch. 9. 1998.

[21] C. Hsu and P. Cheng, "Thermal dispersion in a porous medium," *Int. J. Heat Mass Tran.*, vol. 33, pp. 1587–1597, 1990.

[22] P. Galione, Lehmkuhl, O., J. Rigola, A. Oliva, and R. I, "Numerical simulations of energy storage with encapsulated phase change materials. Special emphasis on solid-liquid phase change CFD modelling," in *Proc. 12th Int. Conf. Energy Storage (INNOSTOCK)*, no. INNO-SP-56, 2012.

[23] O. Lehmkuhl, C. D. Pérez-Segarra, R. Borrell, M. Soria, and A. Oliva, "TERMOFLUIDS: A new Parallel unstructured CFD code for the simulation of turbulent industrial problems on low cost PC Cluster," *Lect. Notes Comput. Sci. Eng.*, vol. 67, pp. 275–282, 2009.

[24] F. X. Trias and O. Lehmkuhl, "A self-adaptive strategy for the time integration of Navier-Stokes equations," *Numer. Heat Tr. B-Fund.*, vol. 60, no. 2, pp. 116–134, 2011.

[25] O. Lehmkuhl, *Numerical resolution of turbulent flows on complex geometries*. PhD thesis, Universitat Politècnica de Catalunya, 2012.

[26] J. Ferziger and M. Perić, *Computational Methods for Fluid Dynamics*, ch. 7. Springer, 2002.

[27] F. L. Tan, "Constrained and unconstrained melting inside a sphere," *Int. Commun. Heat Mass*, vol. 35, pp. 466–475, 2008.

[28] `http://www.ansys.com/Products/Other+Products/ANSYS+ICEM+CFD`. ANSYS ICEM CFD.

[29] R. W. C. P. Verstappen and A. E. P. Veldman, "Symmetry-preserving discretization of turbulent flow," *J. Eng. Math.*, vol. 187, no. 1, pp. 343–368, 2003.

[30] L. Jofre, O. Lehmkuhl, J. Ventosa, F. X. Trias, and A. Oliva, "Conservation properties of unstructured finite-volume mesh schemes for the Navier-Stokes equations," *Numer. Heat Tr. B-Fund.*, vol. 65, no. 1, pp. 53–79, 2014.

[31] J. Messerly, G. Guthrie, S. Todd, and H. Finke, "Low-temperature thermal data for n-Pentane, n-Heptadecane and n-Octadecane," *J. Chem. Eng. Data*, vol. 12, pp. 338–346, 1967.

[32] M. Broadhurst, "An analysis of the solid phase behavior of the normal paraffins," *J. Res. Nat. Bur. Stand., A: Phys. Chem.*, vol. 66, pp. 241–249, 1962.

[33] A. Briard, M. Bouroukba, Petitjean, D., N. Hubert, and M. Dirand, "Experimental enthalpy increments from the solid phases to the liquid phase of homologous n-alkane series (C18 to C38 and C41, C44, C46, C50, C60)," *J. Chem. Eng. Data*, vol. 48, pp. 497–513, 2003.

[34] D. Caudwell, J. Trusler, V. Vesovic, and W. Wakeham, "The viscosity and density of n-Dodecane and n-Octadecane at pressures up to 200MPa and temperatures up to 473K," *Int. J. Thermophys.*, vol. 25, pp. 1339–1352, 2004.

[35] W. Seyer, R. Patterson, and J. Keays, "The density and transition points of the n-paraffin hydrocarbons," *J. Am. Chem. Soc.*, vol. 66, pp. 179–182, 1944.

[36] C. Yaws, *Transport Properties of Chemicals and Hydrocarbons*, ch. 3. William Andrew, 2009.

[37] J. Marano and G. Holder, "A general equation for correlating the thermophysical properties of n-paraffins, n-olefins, and other homologous series. 3. Asymptotic behavior correlations for thermal and transport properties.," *Ind. Eng. Chem. Res.*, vol. 36, pp. 2399–2408, 1997.

[38] R. Holmen, M. Lamvik, and O. Melhus, "Measurements of the thermal conductivities of solid and liquid unbranched alkanes in the C16-to-C19 range during phase transition," *Int. J. Thermophys.*, vol. 23, pp. 27–39, 2002.

[39] A. Briard, M. Bouroukba, Petitjean, and M. Dirand, "Models for estimation of pure n-alkanesâ thermodynamic properties as a function of carbon chain length," *J. Chem. Eng. Data*, vol. 48, pp. 1508–1516, 2003.

[40] D. Ducoulombier, H. Zhou, C. Boned, J. Peyrelasse, H. Saint-Guirons, and P. Xans, "Pressure (1-1000 bars) and temperature (20-100°C) dependence of the viscosity of liquid hydrocarbons," *J. Phys. Chem.*, vol. 90, pp. 1692–1700, 1986.

[41] H. Forsman and P. Andersson, "Thermal conductivity at high pressure of solid odd-numbered n-alkanes ranging from C9H20 to C19H40," *J. Chem. Phys.*, vol. 80, pp. 2804–2807, 1984.

4

Numerical modeling and proposal of a multi-layered solid-PCM thermocline thermal storage concept for CSP.

Contents of this chapter are presently under revision for their publication as:

P. A. Galione, C.D. Pérez-Segarra, I. Rodríguez and A. Oliva, "Multi-layered solid-PCM thermocline thermal storage concept for CSP plants. Numerical analysis and perspectives.", submitted to *Applied Energy*, 2014.

Abstract

Thermocline storage concept has been considered for more than a decade as a possible solution to reduce the huge cost of the storage system in concentrated solar power (CSP) plants. However, one of the drawbacks of this concept is the decrease in its performance throughout the time. The objective of this paper is to present a new thermocline-like storage concept, which aims at circumventing this issue. The proposed concept consists of a storage tank filled with a combination of solid material and encapsulated PCMs, forming a multi-layered packed bed, with molten salt as the

heat transfer fluid. The performance evaluation of each of the prototypes proposed is virtually tested by means of a detailed numerical methodology which considers the heat transfer and fluid dynamics phenomena present in these devices. The virtual tests carried out are designed so as to take into account several charging and discharging cycles until periodic state is achieved, i.e. when the same amount of energy is stored/released in consecutive charging/discharging cycles. As a result, the dependence of the storage capacity on the PCMs' melting points, the total energy and exergy stored/released, as well as the efficiencies of the storing process are compared for the different thermocline, single PCM, cascaded PCM and the proposed multi-layered solid-PCM (MLSPCM) configurations. The analysis shows that the multi-layered solid-PCM concept is a promising alternative for thermal storage in CSP plants.

NOMENCLATURE

A	Surface area
A_t	Transversal area of tank
A_w	Internal surface area of tank's lateral wall
C_p	Specific heat at constant pressure
d_p	Diameter of filler PCM capsule/solid particle
e_{cap}	Capsule's shell width
ex	Exergy
f	Mass liquid fraction (PCM)
g	Gravity acceleration
h	Specific total enthalpy
h_{conv}	Convection coefficient
k	Thermal conductivity
k_{eff}	Effective thermal conductivity
L	specific latent enthalpy
$m, \dot{m}$	Mass and mass flux
n_{fm}	Number of filler particles/capsules in tank section
Nu	Nusselt number
N_r	Number of control volumes of one filler particle/capsule
N_x	Number of tank sections
p	Pressure
Pe	Péclet number
Pr	Prandtl number
r	Radial direction
R_{cond}	Thermal conduction resistance of capsule shell
R_{conv}	Convection resistance between fluid and capsule/solid filler
Re	Reynolds number
t	Time
T	Temperature
U_{amb}	Global heat transfer convection coefficient between the fluid and the ambient
v	Velocity (seepage velocity in packed bed)
V	Volume
Δt	Time step
Δx	Tank section height
ϵ	Volume liquid fraction (porosity)
μ	Dynamic viscosity
ρ	Density

Superscripts and subscripts:

amb	ambient
cap	PCM capsule shell
f	fluid flow
fm	filler material (PCM or solid)
i	Index of tank section/control volume
$i \pm 1/2$	Index of tank section's face limiting i and $i \pm 1$
in	Tank inlet
j	Index of capsule/solid filler control volume
$j \pm 1/2$	Index of filler control volume's face limiting j and $j \pm 1$
l, liq	Liquid phase
out	Tank outlet
s, sol	Solid phase

Abbreviations:

CFL	Courant, Friedrich, Lewy condition
CSP	Concentrated Solar Power
HTF	Heat Transfer Fluid
LCOE	Levelized Cost of Electricity
MLSPCM	Multi-Layered Solid-PCM
PCM	Phase Change Material
TES	Thermal Energy Storage

4.1 Introduction

Thermal energy storage (TES) systems are an essential feature to make a major profit of solar energy. These systems allow using the thermal energy stored in hours of high solar radiation in times of lower radiation and higher energy demands, reducing the mismatch between the supply and demand. In solar power generation stations, the incorporation of TES systems produce an increase in system reliability and generation capacity, and a decrease of the levelized cost of electricity (LCOE) [1, 2].

For concentrated solar power plants (CSP) the current standard for thermal energy storage is the two-tank molten salt system [3, 4], which make profit of the sensible energy changes of a heat transfer fluid (molten salt) under a temperature difference. In the search for investment costs reduction, different designs which result in lower container volumes or in the use of less and/or cheaper storage media have been proposed as alternatives. Some of these, making use of the materials sensible energy capacity, are the thermocline tanks [5, 6] and the concrete storage designs [7].

Thermocline storage system consists of a single tank, with a volume somewhat higher than one of the two-tank system, filled with a solid material forming a porous packed bed through which the heat transfer fluid (HTF) flows. Most of the tank volume is occupied by the solid, which acts as a sensible energy storage medium,

and therefore less of the more costly HTF is needed when compared to an equivalent two-tank system. Different solid materials have been considered, such as quartzite rocks, granite, sand [5], asbestos-containing wastes [8], etc.

Thermocline tanks rely on the principle of thermal stratification, which occurs in a fluid having temperature gradients under the action of the gravitational force. The hot fluid, having a lower density than the cold fluid, is pushed upwards by the buoyancy force while the low temperature fluid is displaced downwards. Therefore, the hot fluid is placed in the upper part of a tank, while the colder fluid stays at the bottom. As a consequence, a vertical temperature gradient is formed which is called "thermocline". The filler material helps in maintaining the thermal gradient, preventing possible mixing flows that may be present due to effects such as cooling through the walls (see for instance [9, 10]) or strong inlet flow currents [11].

Phase change materials (PCM) can also be used to store energy, using less storage material than would be used with a sensible energy storage medium, taking advantage of the latent energy changes during a phase change. The resulting storage device should be more compact, and hopefully cheaper, than one that only makes use of the sensible energy changes. Thermal storage devices using encapsulated PCMs have been studied as a form of thermal storage devices for CSP applications by several authors. Liu et al. [12] perform an extensive review of PCMs suitable to be used in TES for CSP plants and of heat transfer enhancement methods. Michels and Pitz-Paal [13] studied, experimentally and numerically, the performance of storage systems using vertical shell and tube heat exchangers with different PCMs enclosed between the shell and the tubes, with different melting points (cascaded PCM), for parabolic trough plants. Shabgard et al. [14] studied cascaded latent heat storage with gravity-assisted heat pipes for CSP. They performed numerical simulations using a thermal network model and evaluated thermal performance of the different designs after a single charge/discharge cycle. Nithyanandam et al. [15] numerically analyzed packed bed thermal storage with single encapsulated PCMs by studying their performance after a single charging/discharging cycles and after a periodic cyclic state is reached. Parametric studies were performed and guidelines for designing latent thermocline storage systems for CSP were established. Flueckiger et al. [16] studied thermocline storage for solar power stations augmented with latent heat. They integrated their numerical model of the thermocline into a system-level model for the CSP plant and evaluated the effect of the increase of the storage capacity with latent heat. When compared against solid-filled thermocline, limitations in the thermal performance of designs including a single PCM were observed, while some improvement was obtained with some of the cascaded PCM configurations.

Moreover, combination of latent and sensible storage devices has been studied for CSP plants with direct steam generation (DSG) [17], where a PCM storage unit is intended for vapor generation (evaporation) and the sensible energy units for

absorbing the sensible energy of the heat transfer fluid (preheating and superheating).

One of the configurations that have received the most attention is that of packed beds. Many numerical investigations of thermal storage in packed beds can be found in the literature. Ismail and Stuginsky [18] performed a comparative analysis of different packed bed models used for sensible and latent heat storage. Flueckiger et al. [19] reviewed different experimental and numerical studies on thermocline tanks for solar thermal storage. On one hand, models for packed beds of solid materials [6,19–21] usually disregard the temperature gradients inside the particles. On the other hand, if the bed consists of PCM capsules [15,16,22,23], thermal gradients inside them may be significant and are generally, but not always, taken into account. Karthikeyan and Velraj [24] performed a comparison of three one-dimensional models for packed beds of PCM spherical capsules, where the effect of considering the radial variation of temperature inside the capsules was tested. All these models are based on discretizing the conservation equations for the heat transfer fluid and the filler bed, and usually, several simplifying assumptions are made. Depending on the scope of the numerical code, one- , two- or three-dimensional simulations can be performed. However, due to the significantly higher computational costs associated with two- (e.g. [6, 20]) and three-dimensional (none found in the literature) models, one-dimensional analysis is usually chosen for studying several working cycles of TES systems [15, 16, 22–24].

In this work, a new concept of thermocline-like storage system is proposed, consisting in combining low-cost solid and PCM filler materials, appropriately chosen and placed inside the tank in a multi-layered manner. This concept, initially presented in a congress paper [25], is referred as Multi-Layered Solid-PCM (MLSPCM). The main idea behind MLSPCM configurations is the inclusion of high and low melting-point PCMs as filler materials at the ends of the tank, close to the inlet/outlet ports. In [25], the thermal performance of different MLSPCM designs was tested by means of a simplified numerical model. Preliminary results indicated that MLSPCM configurations may reduce the thermocline degradation occurring in the single-solid filled tanks and thus achieve a higher efficiency in the use of the storage capacity.

Zanganeh et al. [26] recently studied a similar configuration using air as the heat transfer fluid, in which a single thin PCM layer of high melting point was placed at the top of a packed bed of rocks. They concluded that the PCM layer contributed to the stabilization of the outflow temperature but did not have an effect on the thermal efficiency of the system. The evaluation was performed after several charge/discharge cycles of the same duration.

In this work, a numerical model for evaluating the thermal behavior and optimizing the design of packed bed systems is presented. The model considers axial thermal conduction within the heat transfer fluid and a special treatment for the convective term of the energy equation, diminishing the artificial numerical diffusion. Since the

intention is to test both solid and PCM filler materials, radial variation of temperature within particles/capsules is taken into account. Numerical experiments are carried out in order to compare the thermal performance of the MLSPCM prototypes against different existent thermocline-like designs, such as solid-filled thermocline, single encapsulated PCM and cascaded PCM concepts. Several configurations are here analyzed and the results are discussed in detail. Thermal performance is evaluated after running several charge/discharge cycles, until a periodic state is reached. Time operation of the processes (charge and discharge) are not fixed beforehand but depend on the temperature of the fluid coming out of the TES, which is limited by some temperature thresholds. The intention with this is to mimic the operating conditions of a real CSP plant, where the solar receivers and power block impose certain limits to the temperature of the HTF. Thermal evaluation is mainly based on terms of total energy storage, efficiency in the use total storage capacity, proportion of PCM effectively changing phase and exergy outputs.

4.2 Mathematical modeling and numerical implementation

Mass, momentum and energy conservation equations have to be solved in order to be able to simulate the thermal behavior of a thermocline-like tank. Some simplifying assumptions are made and empirical correlations are used. The most relevant assumptions are:

1. One-dimensional fluid flow and temperature distribution (in the flow direction).
2. One-dimensional heat transfer in filler particles/capsules (radial direction).
3. Spherical shape of filler particles/capsules.
4. Constant density of both fluid and filler bed materials (solid and PCM).
5. Natural convection and contact melting inside the PCM capsules are neglected.
6. Heat conduction between different filler material particles/capsules is not considered.
7. Negligible radiation heat transfer.

The energy conservation equations are discretized using the Finite Volume Method (FVM). The tank is divided in N_x transversal cylindrical sections of height Δx (see Fig. 4.2). In each tank section, a single representative particle/capsule needs to be simulated, as all are affected by the same fluid temperature due to the one-dimensionality

assumption. This filler particle/capsule, assumed as spherical, is discretized in the radial direction in N_r control volumes, as shown in Fig. 4.2.

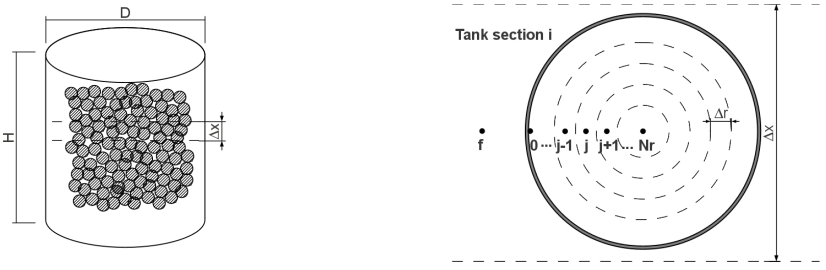

(a) Sketch representing the cylindrical container with the PCM capsules packed in a random fashion

(b) Discretization details of the tank and of a representative particle/capsule, indicating the sub-indices used for tank sections (i) and capsule control volumes (j)

Figure 4.1: Domain and discretization

4.2.1 Energy

Heat transfer fluid (HTF)

The semi-discrete energy conservation equation of the fluid in the i$^{\text{th}}$ tank section ($i = 1...N_x$) results in:

$$\rho_f \epsilon_i V_i C_{p,f} \frac{\partial T_{f,i}}{\partial t} = A_t \left(k_{eff} \frac{\partial T_f}{\partial x} \right) \Bigg|_{i-1/2}^{i+1/2} - \dot{m} C_{p,f} (T_{f,i+1/2} - T_{f,i-1/2}) - n_{fm,i} \frac{T_{f,i} - T_{i,0}}{R_{conv,i} + R_{cond,i}} - U_{amb} A_{w,i} (T_{f,i} - T_{amb}) \tag{4.1}$$

where $T_{i,0}$ is the temperature of the internal surface of the particles/capsules (boundary node in fig. 4.2). In the advective term (second in the right hand side) the fluid is assumed to be coming from section $i-1$ and going to section $i+1$. R_{cond} stands for the thermal resistance in the PCM capsules due to the capsule shell. The mass of the shell is disregarded here and is not considered to add any thermal inertia. The calculation of the thermal resistance due to convection between the HTF and the filler material (R_{conv}) requires the fluid-to-bed Nusselt number, which is calculated using the following correlation, obtained from [27]:

$$Nu = 2.0 + 1.1Re^{0.6}Pr^{1/3} \qquad \text{where } Re = \frac{\rho_f v_f d_p}{\mu_f} \tag{4.2}$$

As stated in [27], the correct use of (4.2) should take into account the effects of solid-phase conduction and thermal dispersion in the diffusive term [first term on the right hand side of (4.1)] and not only molecular diffusion. Therefore, the effective thermal conductivity is evaluated as follows:

$$k_{eff} = k^0_{eff} + k^{disp}_{eff}$$

where the stagnant effective thermal conductivity (k^0_{eff}) is determined here as in [28]:

$$k^0_{eff} = \left(\frac{k_{fm}}{k_f}\right)^{0.280-0.757\log_{10}(\epsilon)-0.057\log_{10}(k_{fm}/k_f)} \tag{4.3}$$

and the effective conductivity due to thermal dispersion (k^{disp}_{eff}) is determined according to the following correlation [29]:

$$\frac{k^{disp}_{eff}}{k_f} = 0.00232Pe^2 \qquad \text{where } Pe = RePr$$

In this work, some of the studied cases include one or several PCMs as filler materials. Since solid and liquid phases may have different thermal conductivities, a criterion is needed to determine the value of k_{fm} used in (4.3). The criterion adopted here consists in using the thermal conductivity calculated at the radius of capsule that divides the sphere in two parts of the same volume.

Filler material

The energy balance for the inner nodes ($j = 1...N_r$) of the filler material remains:

$$\rho_f V_{i,j}\frac{\partial h_{i,j}}{\partial t} = \left(k_{fm}A\frac{\partial T}{\partial r}\right)_{i,j-1/2} - \left(k_{fm}A\frac{\partial T}{\partial r}\right)_{i,j+1/2} \tag{4.4a}$$

while for the boundary node ($j = 0$), in contact with the heat transfer fluid, results in:

$$\rho_f V_{i,0}\frac{\partial h_{i,0}}{\partial t} = \frac{T_{f,i} - T_{i,0}}{R_{conv,i} + R_{cond,i}} - \left(k_{fm}A\frac{\partial T}{\partial r}\right)_{i,1/2} \tag{4.4b}$$

In order to solve these equations it is necessary to define a relation between the enthalpy and the temperature of the filler materials. Considering constant specific heats for each phase, these relations are:

$$\begin{aligned}
h - h_0 &= C_{p,s}(T - T_0), && T \leq T_s \\
h - h_0 &= C_{p,s}(T - T_0) + fL, && T_s < T \leq T_{sl} \\
h - h_0 &= C_{p,l}(T - T_{sl}) + C_{p,s}(T_{sl} - T_0) + fL, && T_{sl} < T \leq T_l \\
h - h_0 &= C_{p,l}(T - T_{sl}) + C_{p,s}(T_{sl} - T_0) + L, && T_l < T
\end{aligned}$$

T_{sl} indicates the temperature in the phase change range chosen as the transition temperature for the specific energy from solid to liquid, or vice versa. Mass liquid fraction (f) values range from 0 (pure solid) to 1 (pure liquid), which, in this work, are calculated as a linear function of temperature in the phase change interval:

$$f = \frac{T - T_s}{T_l - T_s} \tag{4.5}$$

By taking a very narrow temperature range ($T_l - T_s$), fixed melting point PCMs can also be modeled with this approach. Hence, a unique value of h exists for each value of T, and the energy balance [(4.4)] may be expressed with T as the only variable. It should be noted that, since the location of the solid-liquid interface is implicitly determined by values of f, explicit tracking of interface is avoided with this strategy.

4.2.2 Momentum

To determine the pressure drop in the packed bed, the following momentum equation is solved:

$$\left.\frac{\delta p}{\delta x}\right|_i = \pm \left(\frac{5}{Re_{1,i}} + \frac{0.4}{Re_{1,i}^{0.1}} \right) \frac{6\rho_f v_f^2 (1 - \epsilon_i)}{d_{p,i}\epsilon_i^3} - \rho_f g \tag{4.6}$$

$$\text{where } Re_{1,i} = \frac{\rho_f v_f d_{p,i}}{6(1 - \epsilon_i)\mu_f} \text{ (spherical particles) and } v_f = \frac{\dot{m}}{\rho_f A_t}$$

(4.6) is the Carman correlation for packed beds, which is generally used for solid objects forming a bed [30]. In this equation x increases from the bottom to the top, and therefore, the positive sign is used in the discharge of the tank while in the charge process the negative sign is used. The last term accounts for the pressure reduction/increase due to the gravitational action.

4.2.3 Exergy

For evaluating the power generating potential of the energy delivered by the thermal storage, the exergy global balance of the heat transfer fluid is calculated in the following manner:

$$\dot{m}(ex_{out} - ex_{in}) = \dot{m}C_{p,f}(T_{out} - T_{in} - T_{ref} ln \frac{T_{out}}{T_{in}}) \tag{4.7}$$

where T_{ref} is the temperature corresponding to the dead state, which in this work has been taken as 45°C due to being a reasonable value for the temperature at which the vapor is condensed in the power generation block. The resulting exergy flow is the difference between the exergy exiting and entering the tank with the fluid.

4.2.4 Discretization details

Fully implicit schemes, such as that previously adopted in [25], may suffer from numerical diffusion in some degree. Since an accurate modeling of the temperature gradient is needed to evaluate the thermocline tank performance, a different method, similar to that presented by Oppel et al., [31], is used.

An upwind scheme with a first order explicit time integration has been adopted for the advective term, combined with the choice of a time step such that CFL=1 ($\Delta t = \epsilon \Delta x / v_f$). Therefore, each tank section is "filled" completely in each time step by the fluid coming from the upstream section with a temperature equal to the obtained in the previous time step. With this, if no damping is present (e.g. heat transfer to the filler material), a sharp temperature front is exactly transported from the inlet to the outlet with the velocity of the fluid flow. In cases where different porosities are present throughout the packed bed, different CFL numbers result for the same Δt. Here, CFL=1 has been enforced for the most restrictive zone (with the lowest porosity), and thus in the rest of the domain it has been maintained between 0 and 1, where some numerical diffusion is present. The physical diffusion in the HTF is modeled by the diffusive term in (4.1). A central difference spatial discretization and an explicit time integration have been adopted (although if the error in this term is significant, more than one iteration per time step is performed, which results in an approximation to an implicit time integration). To avoid instabilities and for accuracy reasons, the restriction in the time step by the diffusive term is: $\Delta t = 0.3(\epsilon \rho C_p \Delta x^2 / 2k_{eff})$. If the refinement of the grid is high, this limitation may be more restrictive than that of the convective term, and therefore, the CFL=1 condition is not applied anymore. For the diffusive terms of the filler energy equations [(4.4)], central differencing and fully implicit time integration have been adopted.

The algorithm used is similar to that indicated in [25], except that more than one iteration through the tank sections has been necessary at times, especially at the

beginning of each process, in order to calculate more accurately the diffusive term. In each tank section (i), fluid and filler material temperatures have to be solved. The final matrix of coefficients derived from the system of equations in each container section has a tri-diagonal pattern. This allows the usage of a TDMA algorithm to solve the linear system.

4.2.5 Model validation

The first case used to validate the model is that coming from the experimental work of Pacheco et al. [5]. There, a thermocline tank filled with quartzite rock and sand was tested, using molten salt as the heat transfer fluid. This case has been adopted as the validation case in several works on thermocline numerical modeling with solid and encapsulated PCM filler materials, see for instance [15, 16, 19–21].

The thermo-physical properties of the molten salt and of the mixture of quartzite rock and sand are indicated in Table 4.2. The HTF mass flow, which has been calculated following the same strategy as in [32], is set to 5.852 kg/s. The porosity is 0.22 and the effective particle diameter is 0.015 m. The initial state adopted in the simulations is the temperature map obtained from the experimental measures at time 11:30 [5]. Filler material and fluid inside the tank have been assumed to be at thermal equilibrium at this initial state.

The part of the tank containing solid filler material, of 5.2 m height, has been discretized axially in 208 sections ($\Delta x = 2.5$ cm), while each simulated filler particle has been divided radially in 10 control volumes and the time step was set to $\Delta t \sim 12.45$ s (CFL = 1). These parameters have been verified in the sense of producing grid independent results (a difference of $\sim 0.1\%$ has been calculated against a case with 416 sections). Ambient losses have been neglected.

Simulation results are presented in Fig. 4.2. It can be observed that the thermal gradient is well reproduced and that it moves towards the top as the discharge proceeds. Good agreement between experimental and numerical results is obtained. The small discrepancies observed may be due to several causes, such as: uncertainties of the experimental measurements, unavailability of all the parameters from the original work of Pacheco et al. [5] and simplifications of the mathematical model.

The second validation case corresponds to the charging of a tank filled with encapsulated PCM, from the experimental work of Nallusamy et al. [33]. All the configuration parameters and properties have been adopted from that work.

Figure 4.3 shows the results of evolution of temperature of the HTF (water) and PCM (paraffin melting at 60±1°C), measured at $x/L = 0.5$, where x is the axial position and L is the total height. In [33], the position inside the capsule at which the temperature is measured is not indicated. Numerical results of PCM temperatures shown in figure 4.3 are those obtained at the radius that divides the sphere in two

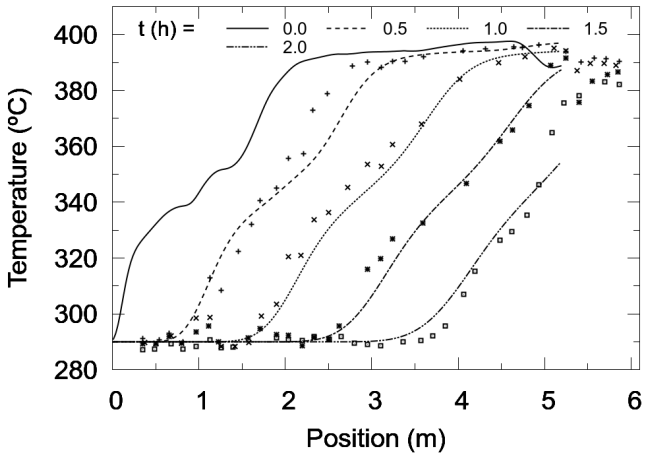

Figure 4.2: Validation. Solid lines correspond to the numerical results, while dots indicate the experimental results from Pacheco et al. [5]. The chronological order of the curves is from left to right.

parts of equal volume. Grid resolution for this case is $N_x = 92$ and $N_r = 55$, which has been checked for grid independence.

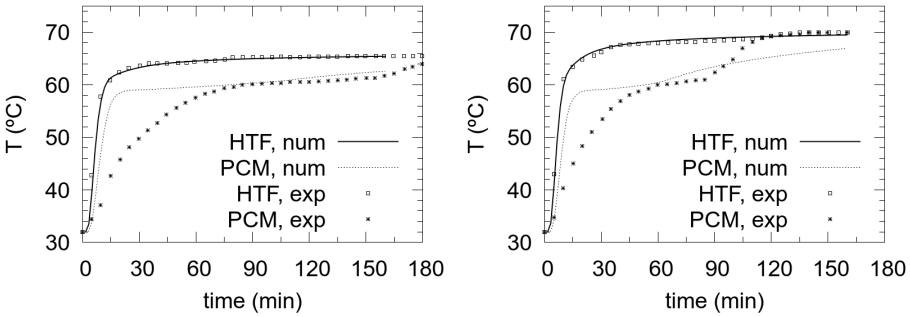

(a) Inlet fluid temperature = 66°C

(b) Inlet fluid temperature = 70°C

Figure 4.3: Temperature evolution at $x/L = 0.5$ of HTF and PCM. Experimental results, indicated by symbols, were extracted from [33]. Numerical results of PCM temperature are taken at the radius that divides the sphere in two parts of equal volume.

A good agreement is observed between experimental results (obtained from [33])

and numerical simulations, specially for the HTF. Some discrepancies are observed in the PCM temperatures. This is probably due to several reasons, such as not accounting for natural convection and contact melting, differences between real thermo-physical properties and those used (paraffins have been observed to present high phase-change temperature ranges, as in [24], and thus melting probably starts at a lower temperature than that assumed) and uncertainty about the exact position of the temperature sensor. However, these discrepancies do not reflect significantly in the HTF temperature, for which the agreement is very good.

4.3 Evaluation of different solutions

This section is devoted to the evaluation of thermocline tanks as thermal storage systems for CSP applications. The thermocline prototype tested by Pacheco et al. [5], is adopted as a reference case from which the operating conditions and tank global dimensions are taken.

Usually, in a CSP plant, the outlet temperature in the discharge process is limited by the minimum temperature that is admissible for the fluid feeding the power block. Similarly, for the charging process, the outlet temperature is limited by the restriction in the temperature of the fluid coming into the solar receivers. Therefore, both the operating time and the stored energy are determined by the level of temperatures attained by the outlet fluid in the charge and discharge processes.

Since the main objective is the evaluation of the performance of single thermocline-like tanks as storage devices in the context of a CSP plant, which is intended to be operated in charge/discharge cycles (one per day) during several years, this evaluation should not rely on values of energy (and exergy) stored or released in a single charge/discharge cycle. As the performance in a single charge (or discharge) process is highly dependent on the initial temperature distribution inside the tank, numerical experiments are carried out for several cycles until a periodic state —independent of the initial conditions of the first cycle— is achieved. Final performance values are determined at this state.

Furthermore, the substitution of all or part of the solid filler material by encapsulated PCM is considered. Therefore, tanks exclusively filled with an encapsulated PCM are tested, where the melting point has been taken as a parameter. Results obtained by the different choices of the melting point lead to the proposal of different combinations of âhybridâ thermocline configurations, in which both solid and encapsulated PCM filler materials are included. This new concept of thermocline-like storage system is herein called Multi-Layered Solid-PCM (MLSPCM). Fig. 4.4 shows a sketch of a MLSPCM configuration with 3 layers. Furthermore, cascaded PCM configurations are also tested and compared.

The same spatial discretization has been used for all the present cases, with 416

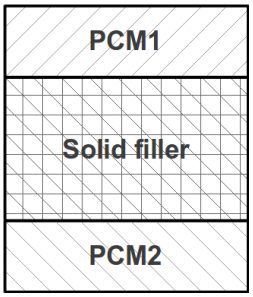

Figure 4.4: Sketch of a 3-layered MLSPCM configuration. PCM1 and PCM2 have high and low melting points, respectively.

axial tank sections sections and 10 filler capsules/particles nodes. The difference with a coarser grid having 208 axial sections is less than 5% in all the cases, and therefore, the accuracy obtained is assumed to be good enough.

4.3.1 Study cases

The following operating conditions are assumed:

- The geometry of the tank and operating conditions are the same for all the cases. Diameter of the filler particles/capsules is 15 mm. The porosity of the packed bed depends on the filler material and it is assumed to be 0.22 for the solid filler material and 0.34 for the encapsulated PCM. Moreover, a shell thickness of 0.4 mm is assumed for the PCM capsules.
- The operation time is not fixed. Instead, outlet temperature limits are imposed, which force the end of each process (charge or discharge) if the outflow temperature is not within these limits. These temperature intervals will be referred to as "admissible" temperature ranges. Here, both admissible ranges have been assumed to be 15% of the maximum temperature interval (100°C); i.e. in the charging phase, the outlet fluid temperature is allowed to be between 290°C and 305°C, while in the discharge it must be between 375°C and 390°C.
- Molten salt flow is fixed to 5.852 kg/s for both processes.
- Ambient losses are neglected [$U_{amb} = 0$ in (4.1)].
- Several consecutive charge/discharge cycles are simulated until a periodic thermal state is reached, i.e. when there is no variation of stored/released energy between consecutive cycles. Since ambient losses are neglected, in the

periodic state the same energy that is stored in the charge must be released in the discharge.

As the admissible temperature intervals for both charge and discharge processes are quite narrow, outlet fluid temperatures for all the cases here studied are very similar. Therefore, a higher operation time is directly related to a higher stored (or released) energy.

In Table 4.1, a code for each case/configuration is defined. The presented cases can be classified according to the filler material/s used as: single-solid thermocline (A); single PCM (B); multi-layered solid-PCM (C and D); and cascaded PCM (F). Percentages between brackets indicate the portion of total height occupied by each filler material. It should be noted that the chosen PCMs are fictitious, having the same thermal properties as those of potassium hydroxide (KOH) but with different fusion temperatures. The exception to this is case B1, where KOH is considered with its actual melting point (360°C according to [13]). This procedure has been adopted in order to account for the variations in performance exclusively due to the change in the fusion temperature of the PCMs. Figure 4.5 depicts sketches of some of the prototypes tested.

Table 4.1: Codification of cases.

Filler material[a]	Code
Quartzite rock & sand (Qu) (100%)	A
KOH (100%)	B1
KOH380 (100%)	B2
KOH300 (100%)	B3
MLSPCM: KOH380-Qu-KOH300 (20%-60%20%)	C1
MLSPCM: KOH380-Qu-KOH300 (40%-20%40%)	C2
MLSPCM: KOH380-Qu-KOH300 (10%-80%10%)	C4
MLSPCM: KOH380-Qu-KOH340-Qu-KOH300 (20%-20%-20%-20%-20%)	D1
MLSPCM: KOH380-Qu-KOH340-Qu-KOH300 (20%-25%-10%-25%-20%)	D2
KOH380-KOH370-KOH340-KOH310-KOH300 (32%-15%-6%-15%-32%)	F1
KOH380-KOH370-KOH340-KOH310-KOH300 (32%-9%-18%-9%-32%)	F2

[a]Materials KOHXXX (where XXX is a 3 digit number) are fictitious PCMs with fusion temperatures indicated by the number XXX (e.g. 300°C), whose thermal properties are equal to those of KOH (melting point = 360°C). The order in which the materials are indicated is the one in which they are placed inside the tank, from the top to the bottom. Between brackets, the proportion of the tank height occupied by each filler layer is indicated.

Table 4.2 shows the physical properties used in the simulations. Table 4.3 shows the mass of solid filler material, PCM and HTF contained. Due to the higher porosity

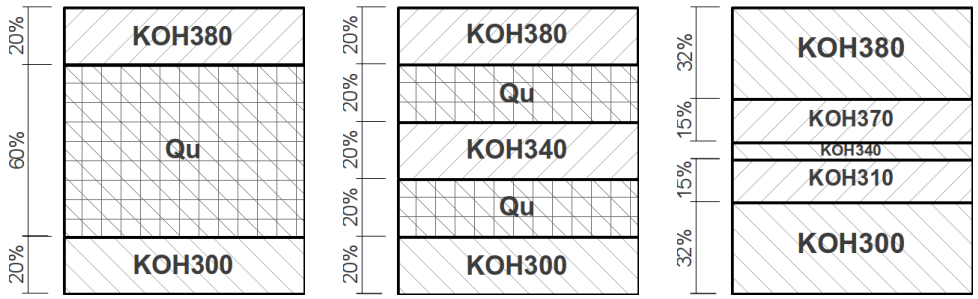

(a) Prototype C1 (b) Prototype D1 (c) Prototype F1

Figure 4.5: Sketches of some of the different filler configurations tested.

Table 4.2: Thermo-physical properties.

	Quartzite rock & sand (Qu) [20]	PCM (KOHXXX) [13]	Molten Salt (HTF) [34]
$\rho\ (kg/m^3)$	2500	2040	1873.8
$C_{p,s}$ $(J/kg\,K)$	830	1340	-
$C_{p,l}$ $(J/kg\,K)$	-	1340	1501.5
k_s $(W/m\,K)$	5.69	0.5	-
k_l $(W/m\,K)$	-	0.5	$0.443 + 1.9 \times 10^{-4} T(^{\circ}\mathrm{C})$
$\mu\ (Pa\,s)$	-	-	$22.714 \times 10^{-3} - 0.12 \times 10^{-3} T + 2.281 \times 10^{-7} T^2 - 1.474 \times 10^{-10} T^3$
$L\ (J/kg)$	-	1.34×10^5	-

of the PCM layers, more confined heat transfer fluid is contained in the configurations including encapsulated PCMs. Furthermore, as the solid filler material is denser than the PCM, prototypes including more of the former contain a higher total mass. The same table also presents data of the storage capacity for each configuration, i.e. the maximum amount of energy that could be stored taking into account both sensible and latent energy contributions, with a temperature jump equal to the difference between the hot and cold inlet fluid temperatures of charge and discharge processes,

respectively. Here, the maximum temperature difference is 100°C(290°C- 390°C). It can be observed that, even in the cases where the filler material is only encapsulated PCM (cases B1-3 and F1-2), the sensible energy capacity is higher than the latent one. This is due basically to two reasons: first, the temperature jump is relatively high, making the sensible energy capacity of the PCMs to be equal to their latent energy capacity ($C_p \Delta T = L$); and second, the HTF confined inside the tank contributes with an extra sensible energy capacity.

Table 4.3: Mass confined inside the tank and storage capacity.

Mass data (ton)	A	B1	B2	B3	C1	C2	C4	D1	D2	F1	F2
Mass of PCM	0.0	42.0	42.0	42.0	17.0	33.9	8.5	25.0	21.0	42.0	42.0
Mass of solid filler material	71.7	0.0	0.0	0.0	42.7	13.8	57.2	28.9	35.8	0.0	0.0
Mass of confined HTF	15.2	23.4	23.4	23.4	18.5	21.8	16.8	20.1	19.3	23.4	23.4
Total mass	86.8	65.4	65.4	65.4	78.2	69.5	82.5	74.1	76.1	65.4	65.4
Storage Capacity											
Filler material (MWh)	1.65	3.13	3.13	3.13	2.25	2.84	1.95	2.53	2.39	3.13	3.13
Confined HTF (MWh)	0.63	0.98	0.98	0.98	0.77	0.91	0.70	0.84	0.80	0.98	0.98
Total (filler + HTF) (MWh)	2.28	4.10	4.10	4.10	3.02	3.75	2.65	3.37	3.19	4.10	4.10
Total sensible energy (%)	100.0	61.9	61.9	61.9	79.1	66.4	88.1	72.3	75.5	61.9	61.9
Total latent energy (%)	0.0	38.1	38.1	38.1	20.9	33.6	11.9	27.7	24.5	38.1	38.1

4.3.2 Results and discussion

Case A: Solid filler material

Table 4.4 shows the thermal performance results for each case. Case A (single-solid thermocline) is shown to behave quite poorly in terms of stored energy when compared against the rest of the cases (with exception of case B1). The stored energy at thermal equilibrium is 1.45 MWh,which is around 63% of the storage capacity. This somewhat low efficiency is due to the thermocline degradation throughout the several charging-discharging cycles, enforced by the assumed temperature thresholds.

Figure 4.6 shows the temperature maps obtained for case A, of charge and discharge processes at various instants for the first two cycles and the periodic state. The degradation of the thermocline can be clearly observed by comparing the 1^{st} and last cycles. The initial condition in the first charge process is a uniform cold temperature throughout the tank. For the 2^{nd} cycle, the initial condition of the filler material and HTF is not anymore a uniform temperature curve, but one with the temperature gradient resulting from the last discharge process. This change in the initial conditions is inevitable due to the requirements imposed on the outgoing fluid temperature, which enforce it to lie inside the admissible range. Since the difference between the incoming fluid temperature and that of the filler material is lower than in the 1^{st} charge process, the heat transfer rate, and thus the thermal gradient (in absolute value), are also lower in the 2^{nd} charging.

Therefore, during the consecutive charging/discharging cycles, the thermal gradient tends to get "flattened" until a periodic unsteady state is reached. Due to this thermocline degradation, the stored/released energy in this periodic state is lower than those of the previous cycles, and so is the operation time, since outlet thresholds are reached earlier.

A useful way of estimating the stored/released energy in each process is to calculate the area between the initial temperature map and the last one, since sensible energy differences are proportional to the temperature jumps. From the comparison between figures 4.3.2 and 4.3.2, a clear difference can be observed in the area between initial and last temperature maps of the charge processes.

Once the periodic state is reached, symmetry between processes can be observed; and therefore, the energy which is stored in the charge is later delivered in the discharge. This is due to having disregarded the thermal losses to the ambient.

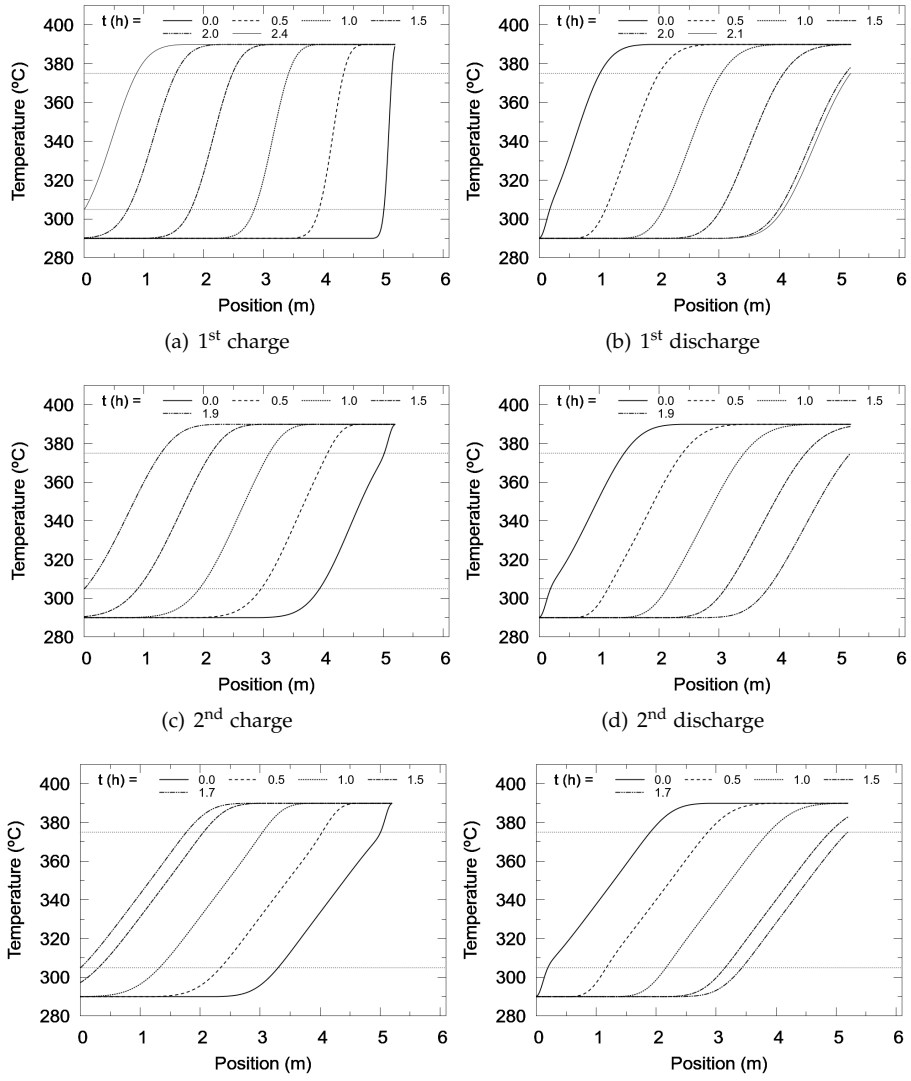

(a) 1st charge

(b) 1st discharge

(c) 2nd charge

(d) 2nd discharge

(e) Periodic state charge

(f) Periodic state discharge

Figure 4.6: Case A. Temperature maps at various instants for the first two cycles and the periodic state. The chronological order of the curves is from left to right in the charge and from right to left in the discharge.

Table 4.4: Performance results for each configuration.

Results	A	B1	B2	B3	C1	C2	C4	D1	D2	F1	F2
Operation time (h)[a]	1.67	1.16	2.61	2.62	2.86	2.99	2.68	1.82	3.00	3.28	2.03
Stored Energy in Filler material (MWh)	1.05	0.63	1.42	1.43	1.72	1.71	1.65	1.11	1.83	2.00	1.25
Stored Energy (Filler + confined HTF) (MWh)	1.45	1.00	2.19	2.20	2.32	2.42	2.22	1.48	2.43	2.66	1.64
Stored Energy / Storage capacity (%)	63.4	24.5	53.4	53.5	76.9	64.5	83.7	43.8	76.2	64.9	40.0
Sensible energy stored / Total stored (%)	100.0	96.3	90.7	90.7	80.0	80.0	86.7	69.8	73.7	64.0	60.6
Latent energy stored / Total stored (%)	0.0	3.7	9.3	9.3	20.0	20.0	13.3	30.2	26.3	36.0	39.4
Effective mass of PCM changing phase (%)	-	2.4	13.1	13.1	73.6	38.4	93.2	47.9	81.7	61.3	41.4
Exergy difference at charge (MWh)	-0.70	-0.48	-1.05	-1.06	-1.12	-1.17	-1.07	-0.71	-1.18	-1.29	-0.79
Exergy difference at discharge (MWh)	0.69	0.48	1.04	1.05	1.11	1.15	1.06	0.70	1.16	1.27	0.78
Pressure losses due to filler bed (Pa)	< 400	< 100	< 100	< 100	< 250	< 150	< 350	< 200	< 250	< 100	< 100

[a] In cases where the charge and discharge operation times are different, (e.g. B2 and B3) the mean value between processes is shown.

Cases B1-3: Encapsulated PCM

A first look into the storage capacity values of Table 4.3 can induce the reader to think that a storage tank filled with an encapsulated PCM should store more energy than the same tank filled with a solid filler material. However, results shown in Table 4.4 reveal a different situation.

Prototype of case B1 is filled with a single encapsulated PCM with a fusion temperature of 360°C (KOH), which is well between the operating temperatures of the storage system.

The temperature maps of the HTF inside the tank at various instants for the first two and periodic state cycles, are plotted in figure 4.7. A clear picture of the problem results from their observation. In the first charge, with an initially cold tank, the outlet temperature threshold is reached in a moment where only part of the contained PCM capsules have melted. The position inside the tank where the phase-changing capsules are located, can be identified by the location where there is a steep temperature gradient ranging from 390°C to 360°C, which for the final state is located at a distance of around 3.6 m from the bottom. Therefore, only a portion of the available latent heat has been used. Moreover, the sensible energy capacity of both the PCM and HTF is much less harnessed than in case A. Thus, the initial condition for the subsequent discharge is one where only a part of both the latent and sensible energy capacity can be exploited.

An important observation is that the melting point of KOH lies outside the admissible temperature ranges for both charging and discharging processes. In the figure it can be observed how the temperature of the HTF passing through the phase-changing PCM capsules is kept close to their melting point. Therefore, in the charging phase, the filler material located downstream of the phase-changing capsules receive the HTF with a temperature equal to the melting point, not being able to melt. Since the threshold temperature is lower than the melting point, the charging process ends before all the PCM has melted, when the capsules located at the outlet (top) cannot bring the HTF temperature below the threshold, with the use of their sensible energy capacity alone.

At the periodic state, the area between the initial and last temperature curves is somewhat higher than those corresponding to the initial cycles (except from the 1^{st} charge). Furthermore, the location of the phase-changing layers has been shifted slightly to the center of the tank.

Cases B2 and B3 have the common feature of using PCMs whose melting points lie inside each of the admissible temperature ranges. In B2 a melting point of 380°C has been chosen, which is inside the admissible range for the outlet fluid temperature of the discharging process (375°C- 390°C); while a melting point of 300°C has been chosen for case B3, lying inside the admissible range of the charging process (290°C-305°C).

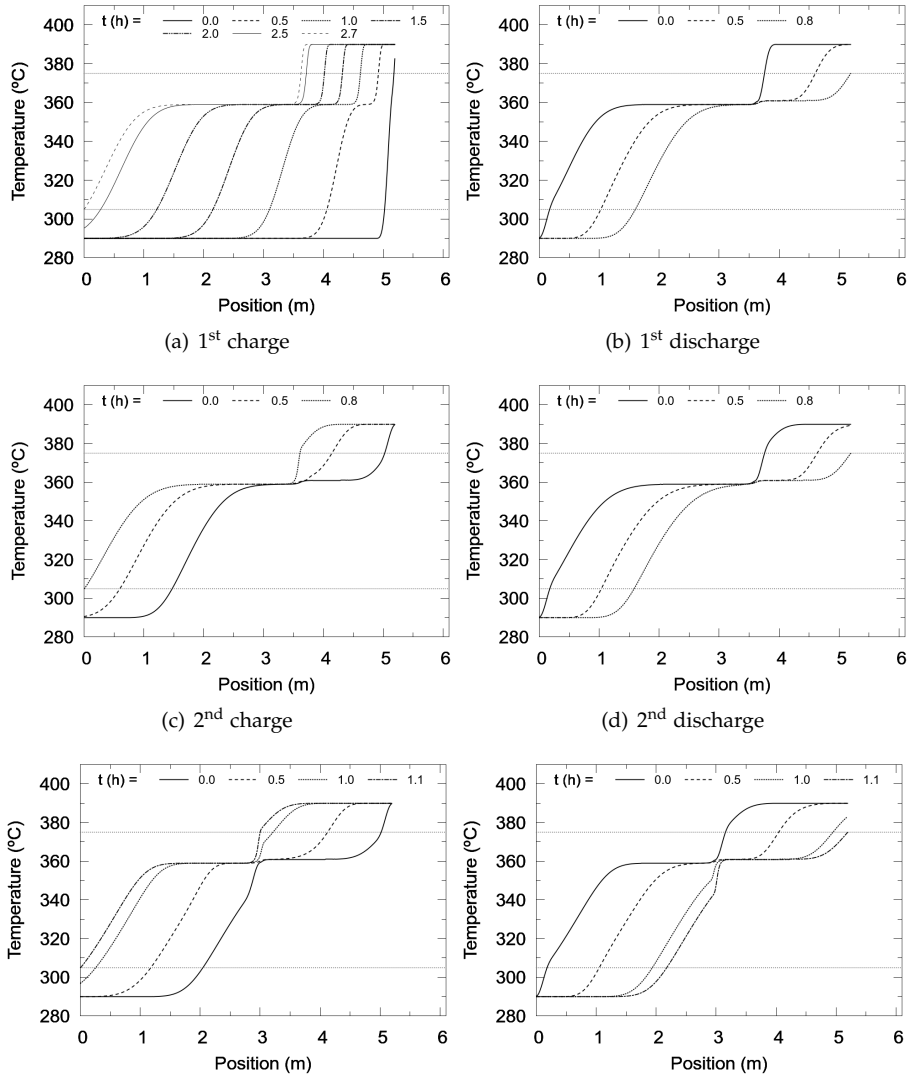

(a) 1st charge

(b) 1st discharge

(c) 2nd charge

(d) 2nd discharge

(e) Periodic state charge

(f) Periodic state discharge

Figure 4.7: Case B1. Temperature maps at various instants for the first two and last cycles. The chronological order of the curves is from left to right in the charge and from right to left in the discharge.

Temperature maps for the periodic state of both cases are shown in figures 4.8 and 4.9. A first observation is that the area between the initial and final maps for both cases is higher than that of case B1. As a result, a higher energy is stored in both cases, as can be observed in Table 4.4.

In these cases, due to the more "intelligent" choice of the melting points, a higher utilization of the whole storage capacity has been attained. For example, in case B2, as the cold fluid comes through the bottom of the tank and the thermal gradient travels to the top, the layers of PCM located at the hot zone, which have melted in the previous charging, act as thermal "buffers" for the outgoing fluid, keeping its temperature close to the melting point until almost all the PCM near the outlet has solidified. Since this temperature is inside the admissible range, the process does not stop, and the rest of the upstream filler material can be thermally discharged.

Due to the symmetry between key temperatures of cases B2 and B3 (melting points, thresholds and operating range), the resulting temperature maps for the periodic state are also symmetric. Charging process of case B2 looks the same as the discharging process of B3, with a shift of the sense in which both axis increase. Furthermore, the results of both cases shown in Table 4.4 are almost identical.

However, a slight difference is encountered in the value of exergy delivered in the discharging phase. Result for case B3, with a PCM melting point of 300°C is slightly higher than that of case B2, where a melting point of 380°C has been adopted. This result may seem strange, since one could think that a higher melting point of the PCM should result in a higher amount of hot fluid coming out of the tank and a higher amount of exergy delivered in the discharge. The explanation for this result can also be extracted from the temperature maps shown in figures 4.8 and 4.9. In case B2, the temperature of the outgoing fluid in the discharge is seen to be the PCM melting point during most of the process (Fig. 4.3.2); while in case B3, it is observed that during most of the discharging phase, the outlet fluid temperature is the maximum possible (Fig. 4.3.2). The reason for this is that the low melting point PCM, acting as a thermal buffer during the charging phase, allows the upstream filler material to be charged of sensible energy up to the maximum temperature, while the high melting point PCM of case B3 is storing most of the high temperature energy (between 380°C and 390°C) in the form of latent heat at 380°C. On the other hand, case B2 also stores less exergy than case B3, since it needs less time to be charged (see figures 4.3.2 and 4.3.2), and its final exergy efficiency (delivered/stored) is slightly higher in the former.

Cases C1-3, D1-2: Multi-layered solid-PCM (MLSPCM)

Results obtained with cases B1 - B3 show that even in the best case, only a little amount of PCM is effectively changing phase in a cycle (less than 15%). Moreover, the results of cases B2 and B3 show that an effective way of increasing the stored energy of an encapsulated PCM tank is to choose a PCM whose fusion temperature lies

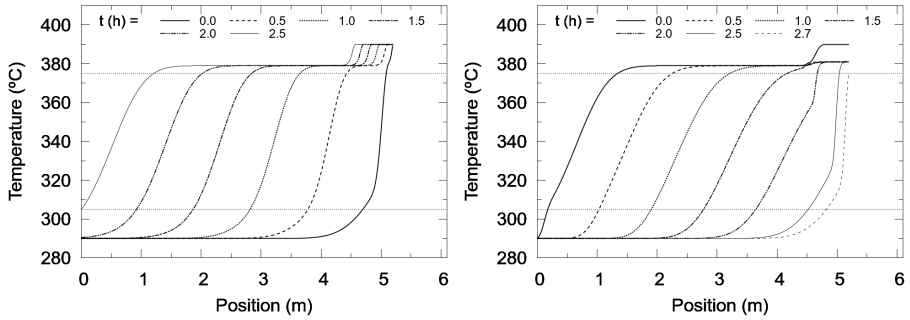

(a) Charge (b) Discharge

Figure 4.8: Case B2. Periodic state. Temperature maps at various instants. The chronological order of the curves is from right to left for the charge process and from left to right for the discharge.

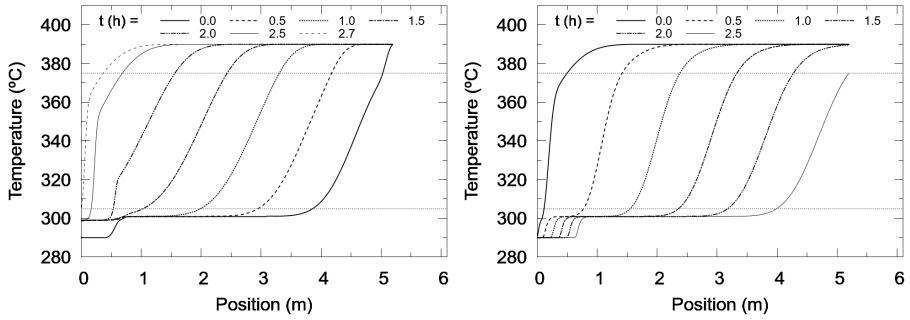

(a) Charge (b) Discharge

Figure 4.9: Case B3. Periodic state. Temperature maps at various instants. The chronological order of the curves is from right to left for the charge process and from left to right for the discharge.

between an admissible temperature interval for either one of the processes (charge or discharge). Thus, the PCM capsules located at the end of the tank, where the HTF temperature is close to its melting point, act as a thermal buffer maintaining a desirable outlet temperature, while the rest of the tank is charged (or discharged) with sensible energy.

Therefore, a tank which is filled with PCM in such a way that most of it can effectively undergo through the phase change, together with the inclusion of a cheaper

solid filler material to store the sensible energy, should be a much more efficient and cost-effective thermal storage device.

Hence, all the configurations studied in this section contain PCM layers at both extremes, one with a high melting point placed at the top of the tank (hot zone) and another with a low melting point placed at the bottom (cold zone), together with solid filler material placed in between.

The symmetry of the proposed problem, given the operation conditions,induces to design the multi-layered prototypes using symmetric configurations, i.e. using the same width for the PCM layers whose melting point are at the same distance (in temperature units) from the corresponding outlet temperatures.

Cases C1 (see sketch on Fig. 4.3.1), C2 and C4 are MLSPCM configurations with only two different PCMs collocated at both extremes of the tank and a solid filler material (quartzite rocks & sand) in the middle zone, forming a 3-layer arrangement, only differing in the width of the layers. PCMs used are those of cases B2 (KOH380) and B3 (KOH300), having melting points lying inside the corresponding admissible range.

Performance results of the three cases, in Table 4.4, show a significant improvement with respect to cases A and B1-3. The "buffering" effect of the PCM at both ends can be appreciated in figures 4.10 to 4.12. An increase in the amount of stored/released energy in the periodic state is observed. The efficiency in the usage of both the total thermal capacity and the latent energy capacity are also higher.

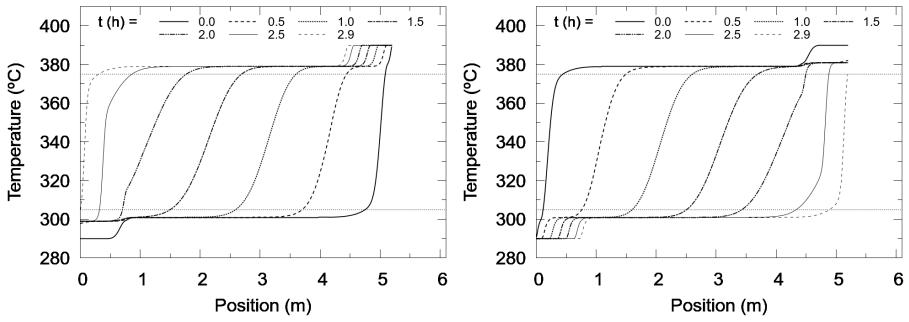

(a) Charge (b) Discharge

Figure 4.10: Case C1. Periodic state. Temperature maps at various instants. The chronological order of the curves is from right to left for the charge process and from left to right for the discharge.

C2 stores the highest amount of energy of the three, but is the one with the lowest efficiencies in terms of utilization of both total and latent storage capacities. In fact,

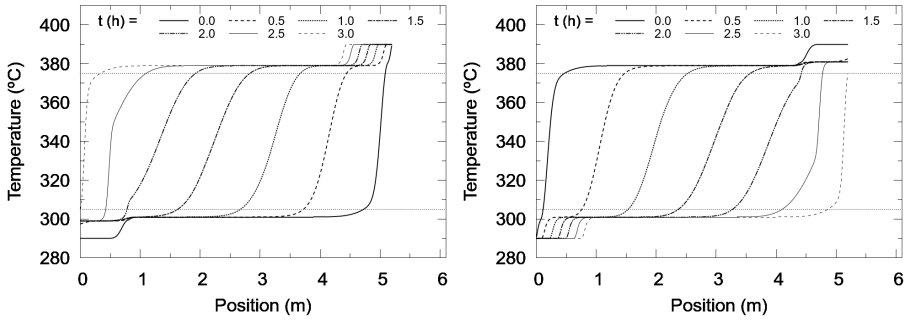

(a) Charge (b) Discharge

Figure 4.11: Case C2. Periodic state. Temperature maps at various instants. The chronological order of the curves is from right to left for the charge process and from left to right for the discharge.

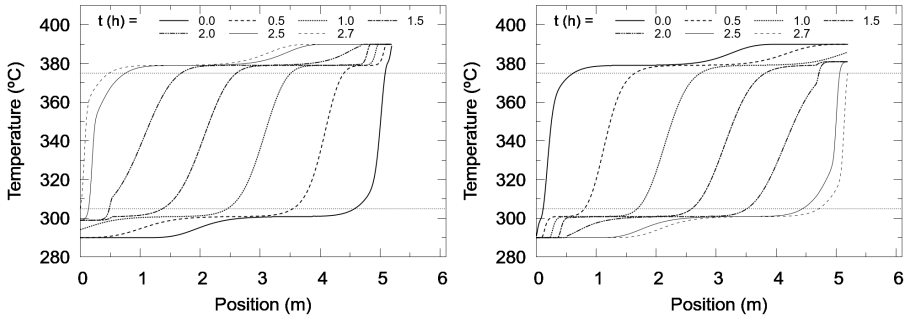

(a) Charge (b) Discharge

Figure 4.12: Case C4. Periodic state. Temperature maps at various instants. The chronological order of the curves is from right to left for the charge process and from left to right for the discharge.

C4, with the least amount of PCM, is the best in terms of efficiency. Around 93% of the PCM is effectively changing phase between successive processes in the latter case, while 74% is the corresponding value for C1 and 38% for C2. In terms of total storage, C1 stores around 4% less than C2, while C4 is around 8% worse than C2.

Regarding the values of fraction of energy stored in the form of latent heat, it can be observed that for cases C1 and C2 they are almost exactly the same and lower for case C4. This can be explained by the following reasoning. The available

energy for storage, from the HTF, is in the form of sensible energy and thus, it is proportional (with the approximation of having constant specific heat) to the temperature difference. Therefore, from the point of view of the high melting point PCM, melting at 380°C, the energy contained in the HTF which is available for being stored in the melting process, is only that between 380°C and 390°C. This is only 10% of the energy contained in the HTF between 290°C and 390°C, and 11.7% of that between 305°C and 390°C (considering both limits of the admissible range of outlet HTF temperatures in the charge). This means that, at most, only 10%-12% of the energy that needs to be extracted from the HTF can be used for melting this PCM, given the constraint for the outgoing temperature of not surpassing 305°C.

It could be argued that, having a second PCM placed at the outlet with a much lower melting point (300°C), much more energy could be stored in the form of latent heat, since the energy contained in a much broader range of temperatures is available for melting this other PCM (in the case of total utilization of the first 10% for melting the first PCM, this range would be 300°C–380°C; or less, if the sensible energy stored in the layers upstream from the second PCM is considered). However, this is not the case when the periodic state has been reached. In this state, and in the absence of thermal losses, the energy stored in the charge is the same as that delivered in the subsequent discharge. Furthermore, the same amount of PCM that melts in the charge, is solidified in the next discharge. For this reason, if 10% of the total available energy is used to melt the high melting point PCM, then only this same amount will be delivered by it in the subsequent discharge. Given the symmetry of the problem, the same reasoning can be applied to the low melting point PCM.

Therefore, as each PCM layer can only theoretically store around 10% - 12% of the total available energy, both PCMs can sum up to 20% - 24% of it, at most. Case C1 and C2 both result in a latent storage of 20%. C4, having significantly less amount of PCM, only reach to around 13%. Table 4.3 shows that the latent capacity of prototype C1, C2 and C4 is around 21%, 34% and 12%, respectively. This is the reason why in case C2 only a small fraction of the PCM effectively changed phase, having a higher latent heat capacity fraction than the theoretically possible.

Cases D1 (see sketch in Fig. 4.3.1) and D2 consist of 5-layered MLSPCM tanks. Both PCM layers at the ends are maintained, while an extra PCM layer is added in the middle zone, with a melting point equal to the mean temperature of the operation range, i.e. 340°C. Other two solid filler material layers are placed between the PCM layers.

Case D1 is seen to behave worse than the previous C1-3 cases. Figure 4.13 shows the temperature maps obtained for this case, with a similar behavior to that of B1. The presence of KOH340 acts as a thermal buffer keeping the HTF temperature close to its melting point, which is outside both admissible temperature ranges. The thermal buffering provided by the other two PCMs is not enough to allow it to melt and

solidify completely before the end of the charge and discharge processes, causing the melting point of 340°C to be a limit to the temperature jump of the solid filler layers and also of much of the middle PCM layer. As a result, the stored energy and the efficiencies are much worse than those of the previous MLSPCM prototypes.

On the other hand, case D2, with the only difference of containing a middle layer of half the width compared to D1, results in a significantly different behavior. Figure 4.14 shows the temperature maps obtained for this case, where a behavior similar to that of cases C1 and C2 can be observed. Here, the thermal buffering effect of the middle layer does not last so long and the top and bottom PCM layers are capable of bearing the "extra" exigency. In fact, the inclusion of the middle layer has resulted in an overall increase in the stored energy with almost the same efficiency, compared to case C1, which had a lower amount of PCM effectively changing phase.

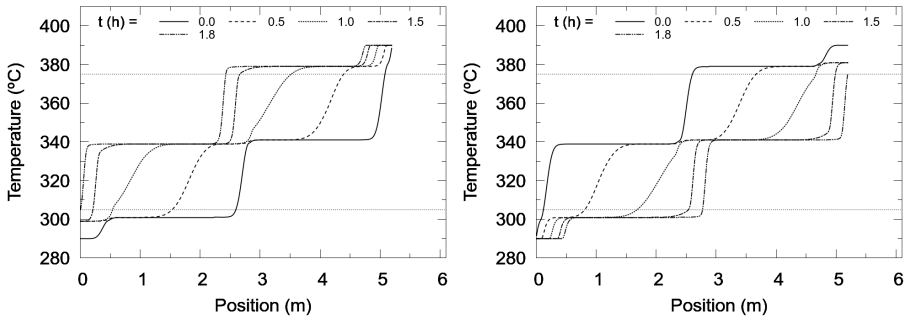

(a) Charge (b) Discharge

Figure 4.13: Case D1. Periodic state. Temperature maps at various instants. The chronological order of the curves is from right to left for the charge process and from left to right for the discharge.

Cases F1-2: Cascaded PCMs

In the cascaded PCM configurations considered here, as in MLSPCM cases, PCM layers located at both ends with melting points lying inside the admissible ranges are included.

The difference between these prototypes and MLSPCM ones, is that no solid filler material is included in the formers. Instead, several layers of different PCMs are placed inside the tank, with increasing melting points from the bottom to the top. This kind of configuration has been studied by other authors, e.g. Michels and Pitz-Paal, [13]. A sketch of configuration F1 is depicted in figure 4.3.1.

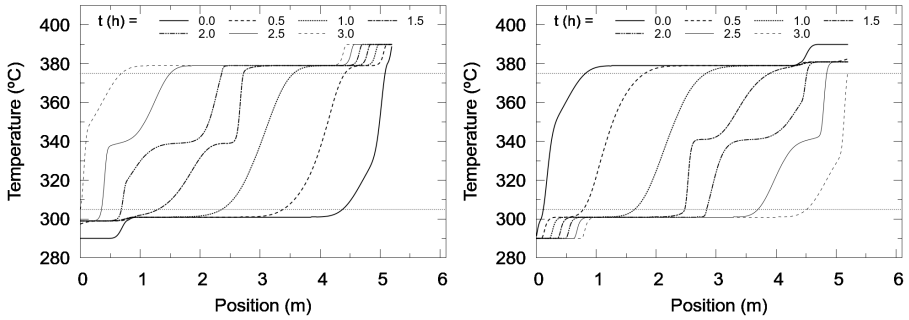

(a) Charge (b) Discharge

Figure 4.14: Case D2. Periodic state. Temperature maps at various instants. The chronological order of the curves is from right to left for the charge process and from left to right for the discharge.

The difference between F1 and F2 is in the width of the three middle layers, where the PCMs with melting points outside the admissible ranges are located. Case F1 includes more of the PCMs with melting points closer to the admissible limits (KOH370 and KOH310), while F2 includes more of the middle PCM with a temperature equal to the operating temperatures mean value (KOH340).

Results of Table 4.4 show that the performance of case F1 is significantly better than that of case F2. As both cases use the same PCM layers, the difference between them is only due to the different proportion of materials included. Temperature maps of both cases at the periodic state can be observed in figures 4.15 and 4.16. Significant differences are encountered. In case F1, the temperature range traversed by the fluid inside the tank is sensibly higher than in case F2. In case F1, when the PCM at the ends have almost completely changed of phase —maintaining outlet fluid temperature inside the admissible range— a considerable amount of the PCM layers inside the tank have also melted/solidified. This is not what happens in case F2, for which the outlet fluid temperature cannot stay within the admissible ranges enough time to allow a good utilization of sensible and latent capacities. Hence, as it has been observed with MLSPCM cases, a correct design of the PCM layers is a critical aspect in the final performance.

Case F1 has been the best of all the studied cases in thermal storage capacity. The energy stored is around 15%, 10%, 20% and 9% higher than for cases C1, C2, C4 and D2, respectively. However, the efficiency in the use of the storage capacity is not very high (65%), with 61% of the PCM effectively changing phase.

Some other cascaded PCM cases with different layer thicknesses have been tested

(not presented), with the result of F1 being the best of all. It might be possible to find other arrangements, with the same PCM layers, with better performance, although it is the authors belief that this arrangement is close to the best possible results.

Considering that an encapsulated PCM is probably much more costly than the solid filler material, MLSPCM prototypes can be expected to be more cost-effective than cascaded PCM, also considering the better efficiency of the former in the use of PCMs latent heat.

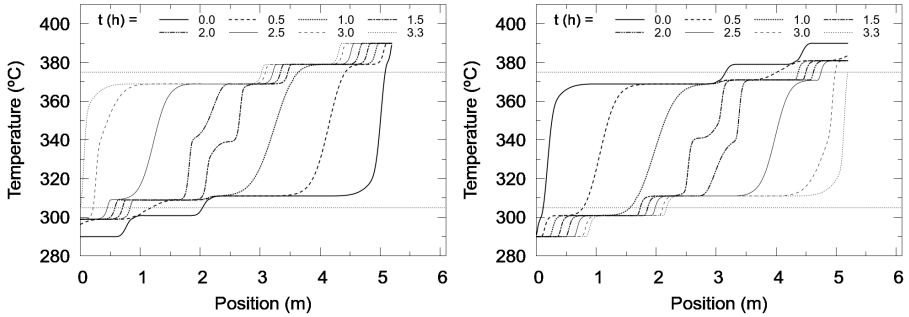

(a) Charge (b) Discharge

Figure 4.15: Case F1. Periodic state. Temperature maps at various instants. The chronological order of the curves is from right to left for the charge process and from left to right for the discharge.

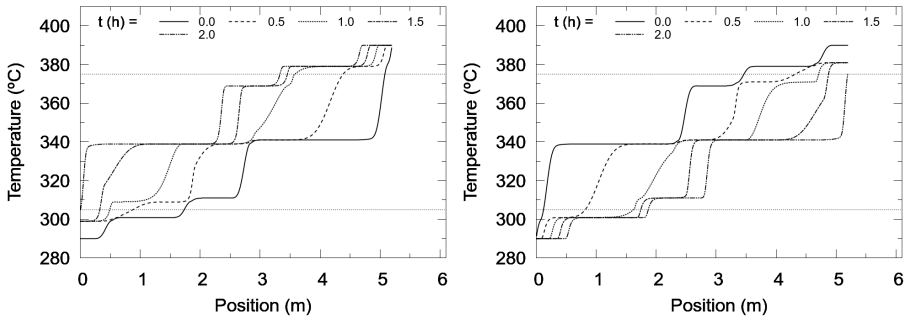

(a) Charge (b) Discharge

Figure 4.16: Case F2. Periodic state. Temperature maps at various instants. The chronological order of the curves is from right to left for the charge process and from left to right for the discharge.

Pressure losses

Pressure losses due to the presence of the filler material [first term on the right hand side of (4.6)] are below 400 Pa for all the cases studied. The highest losses are found in the thermocline system filled uniquely with solid material (case A), due to the higher compactness of the solid filler material compared to those of the encapsulated PCMs. However, when compared against the pressure differences arising due to gravitational effects ($\bar{\rho}gh \sim 10^5$ Pa) these represent less than 0.4% in all the cases, and thus, are negligible.

4.4 Conclusions

A new multi-layered solid-PCM (MLSPCM) thermocline-like thermal storage concept for CSP plants has been presented. The key aspect of this new concept is the inclusion of PCM layers at both ends of the tank, whose fusion temperatures are conveniently chosen to lie inside the predefined admissible temperature ranges for the outgoing fluid in both charge and discharge processes. These admissible temperature ranges depend on the requirements of the power generation block and the solar receivers. The PCM layers act as thermal buffers, causing the outlet fluid to remain close to their melting points, and therefore inside the admissible temperature range for the corresponding process.

In order to design and evaluate the performance of such storage devices, as well as of the other thermocline-like systems considered, a numerical model has been developed and implemented. This model has been successfully validated against experimental data.

Several simulations have been carried out for different designs of thermocline tanks, where configurations of solid, single-PCM, multi-layered solid-PCM and cascaded PCM filler material configurations have been tested. The obtained results show that the multi-layered solid-PCM concept prevents from the high thermocline degradation presented by the single-solid thermocline, resulting in a much higher efficiency in the use of the overall thermal capacity of the system. Furthermore, compared against the cascaded PCM concept, this new approach has the advantage of using much less encapsulated PCM for almost the same total stored energy, again with a higher thermal efficiency. For example, prototype C4 (MLSPCM) stores around 83% of the energy stored with prototype F1 (cascaded PCM), however, it presents a higher efficiency in the use of the storage capacity (84% vs. 65%, respectively). In fact, C4 uses only 20% of the mass of PCM and 72% of molten salt contained in prototype F1.

Therefore, MLSPCM thermocline storage systems can be considered as a promising solution for their use in CSP plants.

Acknowledgments

This work has been financially supported by the *Ministerio de Economía y Competitividad, Secretaría de Estado de Investigación, Desarrollo e Innovación*, Spain (ENE-2011-28699), by the EIT via the KIC InnoEnergy TESCONSOL project (ref. 20_2011_IP16) and by the *Secretaria d'Universitats i Recerca (SUR) del Departament d'Economia i Coneixement (ECO) de la Generalitat de Catalunya* and by the European Social Fund.

References

[1] M. Medrano, A. Gil, I. Martorell, X. Potau, and L. F. Cabeza, "State of the art on high temperature thermal ebergy storage for power generation. part 2—Case studies," *Renew. Sust. Energ. Rev.*, no. 14, pp. 56–72, 2010.

[2] G. J. Kolb, C. K. Ho, T. R. Mancini, and J. A. Gary, "Power Tower Technology Roadmap and Cost Reduction Plan," Tech. Rep. SAND2011-2419, Sandia National Laboratories, 2011.

[3] U. Herrmann, B. Kelly, and H. Price, "Two-tank molten salt storage for parabolic trough solar power plants," *Energy*, vol. 29, pp. 883–893, 2004.

[4] J. I. Ortega, J. I. Burgaleta, and F. M. Téllez, "Central Receiver System Solar Power Plant Using Molten Salt as Heat Transfer Fluid," *J. Sol. Energ.-T. ASME*, vol. 130, pp. 024501–1–6, 2008.

[5] J. E. Pacheco, S. K. Showalter, and W. J. Kolb, "Development of a Molten-Salt Thermocline Thermal Storage System for Parabolic Trough Plants," *J. Sol. Energ.-T. ASME*, vol. 124, pp. 153–159, 2002.

[6] A. Yang and S. V. Garimella, "Molten-salt thermal energy storage in thermoclines under different environmental boundary conditions," *Appl. Energ.*, vol. 87, pp. 3322–3329, 2010.

[7] R. Tamme, D. Laing, and W. D. Steinmann, "Advanced Thermal Energy Storage Technology for Parabolic Trough," *J. Sol. Energ.-T. ASME*, vol. 126, pp. 794–800, 2004.

[8] N. Calvet, J. C. Gomez, A. Faik, V. V. Roddatis, A. Meffre, G. C. Glatzmaier, S. Doppiu, and X. Py, "Compatibility of a post-industrial ceramic with nitrate molten salts for use as filler material in a thermocline storage system," *Appl. Energ.*, vol. 109, pp. 387–393, 2013.

[9] R. Shyu, J. Lin, and L. Fang, "Thermal analysis of stratified storage tanks," *J. Sol. Energ.-T. ASME*, vol. 111, pp. 54–61, 1989.

[10] I. Rodríguez, J. Castro, C. Pérez-Segarra, and A. Oliva, "Unsteady numerical simulation of the cooling process of vertical storage tanks under laminar natural convection," *Int. J. Therm. Sci.*, vol. 48, pp. 708–721, 2009.

[11] L. J. Shah and S. Furbo, "Entrance effects in solar storage tanks," *Sol. Energy*, vol. 75, pp. 337–348, 2003.

[12] M. Liu, W. Saman, and F. Bruno, "Review on storage materials and thermal performance enhancement techniques for high temperature phase change thermal storage systems," *Renew. Sust. Energ. Rev.*, vol. 16, pp. 2118–2132, 2012.

[13] H. Michels and R. Pitz-Paal, "Cascaded latent heat storage for parabolic trough solar power plants," *Sol. Energy*, vol. 81, pp. 829–837, 2007.

[14] H. Shabgard, C. W. Robak, T. L. Bergman, and A. Faghri, "Heat transfer and exergy analysis of cascaded latent heat storage with gravity-assisted heat pipes for concentrating solar power applications," *Sol. Energy*, vol. 86, no. 3, pp. 816–830, 2012.

[15] K. Nithyanandam, R. Pitchumani, and A. Mathur, "Analysis of a latent thermocline storage system with encapsulated phase change materials for concentrating solar power," *Appl. Energ.*, vol. 113, pp. 1446–1460, 2014.

[16] S. M. Flueckiger and S. V. Garimella, "Latent heat augmentation of thermocline energy storage for concentrating solar power —A system-level assessment," *Appl. Energ.*, vol. 116, pp. 278–287, 2014.

[17] W. Steinmann and R. Tamme, "Latent Heat Storage for Solar Steam Systems," *J. Sol. Energ.-T. ASME*, vol. 130, pp. 011004–1–011004–5, 2008.

[18] K. A. R. Ismail and R. Stuginsky Jr., "A parametric study on possible fixed bed models for pcm and sensible heat storage," *Appl. Therm. Eng.*, vol. 19, pp. 757–788, 1999.

[19] S. M. Flueckiger, Y. Z., and S. V. Garimella, "Review of Molten-Salt Thermocline Tank Modeling for Solar Thermal Energy Storage," *Heat Transfer Eng.*, vol. 34, no. 10, pp. 787–800, 2013.

[20] C. Xu, Z. Wang, Y. He, X. Li, and F. Bai, "Sensitivity analysis of the numerical study on the thermal performance of a packed-bed molten salt thermocline thermal storage system," *Appl. Energ.*, vol. 92, pp. 65–75, 2012.

[21] A. Modi and C. D. Pérez-Segarra, "Thermocline thermal storage systems for concentrated solar power plants: One-dimensional numerical model and comparative analysis," *Sol. Energy*, vol. 100, pp. 84–93, 2014.

[22] J. P. Bédérrecats, J. Castaing-Lasvignottes, F. Strub, and J. P. Dumas, "Study of a phase change energy storage using spherical capsules. Part ii: Numerical modelling," *Energ. Convers. Manage.*, vol. 50, pp. 2537–2546, 2009.

[23] A. Felix Regin, S. C. Solanki, and J. S. Saini, "An analysis of a packed bed latent heat thermal energy storage system using pcm capsules: Numerical investigation," *Renew. Energ.*, vol. 34, pp. 1765–1773, 2009.

[24] S. Karthikeyan and R. Velraj, "Numerical investigation of packed bed storage unit filled with pcm encapsulated spherical containers —a comparison between various mathematical models," *Int. J. Therm. Sci.*, vol. 60, pp. 153–160, 2012.

[25] P. Galione, C. D. Pérez-Segarra, I. Rodríguez, O. Lehmkuhl, and J. Rigola, "A new thermocline-pcm thermal storage concept for csp plants. numerical analysis and perspectives," in *Proceedings of the SolarPACES 2013 International Conference*, vol. 49 of *Energy Procedia*, pp. 790–799, Elsevier, 2014.

[26] G. Zanganeh, M. Commerford, A. Haselbacher, A. Pedretti, and A. Steinfeld, "Stabilization of the outflow temperature of a packed-bed thermal energy storage by combining rocks with phase change materials," *Appl. Therm. Eng.*, no. 70, pp. 316–320, 2014.

[27] N. Wakao, S. Kaguei, and T. Funazkri, "Effect of fluid dispersion coefficients on particle-to-fluid heat transfer coefficients in packed beds," *Chem. Eng. Sci.*, vol. 34, pp. 325–336, 1979.

[28] R. Krupiczka, "Analysis of thermal conductivity in granular materials," *Int. Chem. Eng.*, vol. 7, no. 1, pp. 122–144, 1967.

[29] A. Nakayama, F. Kuwahara, and Y. Kodama, "An equation for thermal dispersion flux transport and its mathematical modelling for heat and fluid flow in a porous medium," *J. Fluid Mech*, vol. 563, pp. 81–96, 2006.

[30] R. G. Holdich, *Fundamentals of particle technology*. Midland Information Technology and Publishing, 2002.

[31] F. J. Oppel, A. J. Ghajar, and P. M. Moretti, "Computer Simulation of Stratified Heat Storage," *Appl. Energ.*, vol. 23, pp. 205–224, 1986.

[32] S. M. Flueckiger, B. D. Iverson, S. V. Garimella, and J. E. Pacheco, "System-level simulation of a solar power tower plant with thermocline thermal energy storage," *Appl. Energ.*, vol. 113, pp. 86–96, 2014.

[33] N. Nallusamy, S. Sampath, and R. Velraj, "Experimental investigation on a combined sensible and latent heat storage system integrated with constant/varying (solar) heat sources," *Renew. Energ.*, vol. 32, pp. 1206–1227, 2007.

[34] A. B. Zavoico, "Solar power tower design basis document," Tech. Rep. SAND2001-2100, Sandia National Laboratories, 2001.

5

Evaluation of MLSPCM for its application in a 50MWe CSP plant.

Contents of this chapter have been submitted for publication as:

P. A. Galione, C.D. Pérez-Segarra, I. Rodríguez, S. Torras and J. Rigola, "Multi-layered solid-PCM thermocline thermal storage for CSP. Numerical evaluation of its application in a 50MWe plant.", submitted to *Applied Energy*, 2014.

Abstract

Thermocline storage concept is considered as a possible solution to reduce the cost of thermal storage in concentrated solar power (CSP) plants. Recently, a multi-layered solid-PCM (MLSPCM) concept, consisting of a thermocline-like tank combining layers of solid and phase change filler materials, was proposed. This approach has been observed to result in lower thermocline degradation throughout charge/discharge cycles, due to the thermal buffering effect of the PCM layers located at both ends of the tank. MLSPCM prototypes designed for a pilot scale plant were numerically tested and compared against other designs of single-tank thermocline systems, such as: solid-filled thermocline, tanks filled with a single encapsulated PCM and cascaded-PCM configurations. Results showed promising results of the MLSPCM configurations for their potential use in CSP plants.

In this work, the MLSPCM concept is used for designing a thermal energy storage (TES) system for a CSP plant with the dimensions and operating conditions of a parabolic trough plant of 50 MWe, similar to Andasol 1 (Granada, Spain). The

performance evaluation of each of the proposed prototypes is virtually tested by means of a numerical methodology which considers the heat transfer and fluid dynamics phenomena present in these devices. Two sets of cases are considered, one with the objective of testing the TES systems individually, by defining specific operating conditions and taking the systems to a periodic steady state; and another, aiming to evaluate their performance after several days of operation in a CSP plant, in which the weather variability and the thermal behavior of tank walls and foundation are simulated. Thermal performance parameters, such as total energy and exergy stored/released and the efficiency in the use of the storage capacity, are calculated and compared with those obtained by other thermocline-like configurations (single-solid and single-PCM), and by a reference 2-tank molten-salt system. Obtained results allow to consider MLSPCM concept as a promising alternative for thermal storage in CSP facilities.

NOMENCLATURE

A	Surface area
A_t	Transversal area of tank
A_w	Internal surface area of tank's lateral wall
C_p	Specific heat at constant pressure
d_p	Diameter of filler PCM capsule/solid particle
ex	Exergy
f	Mass liquid fraction (PCM)
F	Capsule volume fraction filled by PCM
h	Specific total enthalpy
h_{conv}	Convection coefficient
k	Thermal conductivity
k_{eff}	Effective thermal conductivity
L	Specific latent enthalpy
$m, \dot{m}$	Mass and mass flux
N_r	Number of control volumes of one filler particle/capsule
N_x	Number of tank sections
$\dot{Q}$	Thermal power
r	Radial direction
R_{cond}	Thermal conduction resistance of capsule shell
R_{conv}	Convection resistance between fluid and capsule/solid filler
t	Time
T	Temperature
U_{TC-Sh}	Heat transfer convection coefficient between the fluid in the packed bed and the tank shell
v	Velocity (seepage velocity in packed beds)
V	Volume
Δt	Time step
Δx	Tank section height
ϵ	Volume liquid fraction (porosity)
η	Efficiency
μ	Dynamic viscosity
ρ	Density

Superscripts and subscripts:

f	Fluid flow
fm	Filler material (PCM or solid)
i	Index of tank section/control volume
$i \pm 1/2$	Index of tank section's face limiting i and $i \pm 1$
in	Tank inlet
j	Index of capsule/solid filler control volume
$j \pm 1/2$	Index of filler control volume's face limiting j and $j \pm 1$
l, liq	Liquid phase
nom	Nominal
out	Tank outlet
s, sol	Solid phase

Abbreviations:

CFL	Courant, Friedrich, Lewy condition
CSP	Concentrated Solar Power
DNI	Direct Normal Irradiation
HTF	Heat Transfer Fluid
MLSPCM	Multi-Layered Solid-PCM
PB	Power Block
PCM	Phase Change Material
SF	Solar Field
TES	Thermal Energy Storage

5.1 Introduction

Thermal energy storage (TES) allows a more effective use of solar energy by reducing the mismatch between the energy supply and its demand. In concentrated solar power (CSP) facilities, TES systems increase the reliability and generation capacity of the whole system and reduce the levelized cost of electricity [1,2].

Nowadays, many CSP plants incorporate a molten-salt two-tank TES system (e.g. Andasol and Extresol in Spain, Crescent Dunes and Solana in USA), which makes use of the sensible energy capacity of the molten-salt [3,4]. However, different TES designs resulting in lower investment costs are currently under study, some of which are also based on the sensible energy capacity of the materials, such as thermocline single-tanks [5,6] and concrete storage designs [7].

In thermocline systems, both high and low temperature fluids are contained in the same tank. Thermal stratification is the mechanism separating them, and the thermal gradient produced within the fluid is called thermocline. The thermocline thickness indicates the amount of thermal mixing, which may be due to natural convection effects (see e.g. [8,9]) and strong inlet flow currents [10], and is intended to be maintained at a minimum. A modification to the original concept, aiming at

reducing the thermal mixing and also reducing the amount of molten-salt used, is to fill the tank with a cheaper solid material such as quartzite rocks, granite, sand [5], asbestos-containing wastes [11], forming a porous packed bed through which the heat transfer fluid flows.

On the other hand, several researchers have been investigating the use of phase change materials (PCM) as thermal storage media, taking advantage of the high energy density present in the phase-change phenomena. For example, Michels and Pitz-Paal [12] performed a numerical and experimental investigation of storage systems using different PCMs with cascaded melting points, contained in shell and tube heat exchangers, for parabolic trough CSP plants. Liu et al. [13] carried out an extensive review of high-temperature phase change storage materials and of thermal enhancement techniques. Shabgard et al. [14] performed a numerical analysis of cascaded latent heat storage with gravity-assisted heat pipes for CSP applications. Nithyanandam et al. [15] studied packed bed thermal storage with encapsulated PCMs for CSP by means of a numerical model. They performed parametric analyses and established guidelines for the design of latent storage systems. Flueckiger et al. [16] analyzed latent-heat-augmented thermocline storage for CSP using an integrated system-level model for the whole CSP plant and evaluated the effect of the increase of the storage capacity with the latent heat. Limitations in the thermal performance of tanks including PCMs were observed, while some improvement was obtained with some of the cascaded PCM designs.

Furthermore, Steinmann and Tamme [17] studied the combination of latent and sensible storage heat exchangers specially suited for direct steam generation solar field technology (DSG). A PCM storage unit was intended for producing the vapor generation (evaporation) and two concrete storage units for storing the sensible portion of the fluid's energy (pre and superheating).

In previous works [18, 19], a new concept of thermocline-like thermal storage device named multi-layered solid-PCM (MLSPCM), consisting of a packed bed of different layers of solid and PCM filler materials, was presented. There, MLSPCM designs of the same dimensions and operating conditions as those of the pilot scale tank presented by Pacheco et al. [5], were numerically tested and compared against other designs of single-tank thermocline-like systems such as: single-solid, single-PCM and cascaded-PCM filler configurations. Results obtained for MLSPCM prototypes showed to be promising for their potential use in CSP plants.

In this work, the MLSPCM concept is used for making up a TES system for a CSP plant. A parabolic trough of 50MW of electric output is assumed, similar to Andasol 1 plant (Granada, Spain). With this aim, two levels of analysis are carried out. Firstly, numerical simulations similar to those presented in [18] are carried out, in order to evaluate the performance of the full-scale TES prototypes under specific conditions. In these, the TES is charged and discharged consecutively until reaching

a periodic steady state. Secondly, in order to test the different TES systems under operating conditions closer to those of a CSP facility, another analysis is performed incorporating weather variation, idle processes and thermal losses to the tank shell and foundation, for several days of plant operation..

For this, a modular object-oriented code is used [20], which links the different models corresponding to the elements under study.

Similarly as in the pilot-scale prototypes presented in [18, 19], some full-scale MLSPCM configurations are observed to produce an increase of the efficiency in the use of total capacity when compared with other thermocline-like designs, especially in the isolated TES analysis. Although consideration of the variability of the operating conditions results in closer values of accumulated energy and efficiency, MLSPCM concept continues to present advantages over the solid-filled thermocline design. The advantages against single-PCM packed beds are more clear, since a similar storage is obtained using a much lower amount of encapsulated PCM, which is assumed to be a costly component compared to the solid filler material. As a result of the study, a MLSPCM prototype considered equivalent to the reference 2-tank system is presented, resulting in the same amounts of energy and exergy delivered to the power block in both analyses.

5.2 Mathematical modeling and numerical implementation

The thermocline-like TES considered are formed by different elements: thermocline packed bed (filler material and HTF), tank foundation and tank walls, which interact with each other through their boundary conditions. This implementation has been performed within the NEST platform [20], which allows linking between different elements of the thermal system. The mathematical model considers the transient behavior of the thermocline-like packed beds, the tank walls and insulation, taking into account the variable outdoor conditions (DNI, ambient temperature). A brief mathematical description, focused on the modeling of the packed bed, is presented hereafter.

5.2.1 Packed bed

The model presented in [18] is used. Mass, momentum and energy conservation equations have to be solved in order to be able to simulate the thermal behavior of a thermocline-like tank. One-dimensionality in the fluid flow and in the heat transfer inside particles/capsules is assumed. Natural convection and contact melting

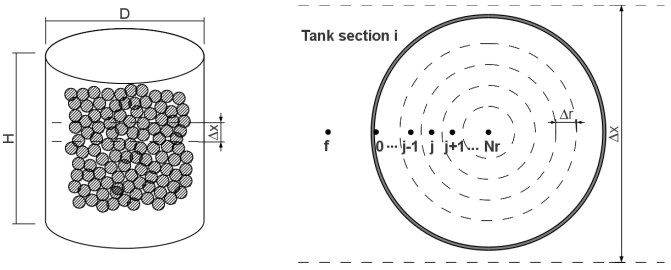

(a) Sketch representing the cylindrical container with the PCM capsules packed in a random fashion

(b) Discretization details of the tank and of a representative particle/capsule, indicating the sub-indices used for tank sections (i) and capsule control volumes (j)

Figure 5.1: Domain and discretization.

inside PCM capsules is neglected, as well as thermal conduction between different particles/capsules.

In the filler particles/capsules, a radial variation of the temperature is assumed. Conservation equations are discretized using the Finite Volume Method (FVM). The tank is divided in N_x transversal cylindrical sections of height Δx (see Fig. 5.1(a)). In each tank section, a single representative particle/capsule needs to be simulated, due to the one-dimensionality assumption. This filler particle/capsule is discretized in the radial direction in N_r control volumes, as shown in Fig. 5.1(b).

For the heat transfer fluid (HTF) going through the porous bed, the semi-discrete energy conservation equation of the fluid in the i$^{\text{th}}$ tank section ($i = 1...N_x$) results in:

$$\rho_f \epsilon_i V_i C_{p,f} \frac{\partial T_{i,f}}{\partial t} = A_t \left(k_{eff} \frac{\partial T_f}{\partial x} \right) \Bigg|_{i-1/2}^{i+1/2} - \dot{m} C_{p,f} (T_{i+1/2,f} - T_{i-1/2,f}) - n_{fm,i} \frac{T_{i,f} - T_{i,0}}{R_{conv,i} + R_{cond,i}} - U_{TC-Sh} A_{w,i} (T_{i,f} - T_{i,Sh}) \tag{5.1}$$

where $T_{i,0}$ is the temperature of the internal surface of the particles/capsules (boundary node in fig. 5.1(b)). In the advective term (second in the right hand side) the fluid is assumed to be coming from section $i-1$ and going to section $i+1$.

R_{cond} stands for the thermal resistance in the PCM capsules due to the capsule shell. The mass of the shell is disregarded here and is not considered to add any thermal inertia. The calculation of the thermal resistance due to convection between the HTF and the filler material (R_{conv}) requires the fluid-to-bed Nusselt number, which is calculated using the correlation obtained from [21]:

The effective thermal conductivity (accounting for solid-phase conduction and thermal dispersion) is evaluated as the sum of stagnant and dispersion effective conductivities, calculated with the correlations obtained from [22] and [23].

The energy balance for the inner nodes ($j = 1...N_r$) of the filler material (either PCM capsules or solid particles) remains:

$$\rho_{fm} F_i V_{i,j} \frac{\partial h_{i,j}}{\partial t} = \left(k_{fm} A \frac{\partial T}{\partial r} \right)_{i,j-1/2} - \left(k_{fm} A \frac{\partial T}{\partial r} \right)_{i,j+1/2} \tag{5.2a}$$

while for the boundary node ($j = 0$), in contact with the heat transfer fluid, results in:

$$\rho_{fm} F_i V_{i,0} \frac{\partial h_{i,0}}{\partial t} = \frac{T_{f,i} - T_{i,0}}{R_{conv,i} + R_{cond,i}} - \left(k_{fm} A \frac{\partial T}{\partial r} \right)_{i,1/2} \tag{5.2b}$$

where F_i indicates the volume fraction of the capsules occupied by the PCM (F_i=1 for the solid particles). This value is between 0 and 1 and takes into account that a void space is needed in order to allow for the thermal expansion in the melting.

The relations between enthalpy and temperature for the filler materials (solid and/or PCM) are:

$$\begin{aligned}
h - h_0 &= C_{p,s}(T - T_0), && T \leq T_s \\
h - h_0 &= C_{p,s}(T - T_0) + fL, && T_s < T \leq T_{sl} \\
h - h_0 &= C_{p,l}(T - T_{sl}) + C_{p,s}(T_{sl} - T_0) + fL, && T_{sl} < T \leq T_l \\
h - h_0 &= C_{p,l}(T - T_{sl}) + C_{p,s}(T_{sl} - T_0) + L, && T_l < T
\end{aligned}$$

where T_{sl} indicates the temperature in the phase change range chosen as the transition temperature for the specific energy from solid to liquid, or vice versa. Mass liquid fraction (f) ranges from 0 (pure solid) to 1 (pure liquid) and is calculated as a linear function of temperature in the phase change interval:

$$f = \frac{T - T_s}{T_l - T_s} \tag{5.3}$$

By taking a very narrow temperature range ($T_l - T_s$), fixed melting point PCMs can also be modeled with this approach. Hence, a unique value of h exists for each value of T, and the energy balance (Eq. (5.2)) is expressed with T as the only variable.

For evaluating the power generating potential of the energy delivered by the thermal storage, the exergy global balance of the heat transfer fluid is calculated in the following manner:

$$\dot{m}(ex_{out} - ex_{in}) = \dot{m} C_{p,f} (T_{out} - T_{in} - T_{ref}\, ln \frac{T_{out}}{T_{in}}) \tag{5.4}$$

where T_{ref} is the temperature corresponding to the dead state, which in this work has been taken as 45°C due to being a reasonable value for the temperature at which the vapor is condensed in the power generation block.

To determine the pressure drop in the packed bed, the Carman correlation is used (see e.g. [24]).

For further details of the model used, please refer to reference [18].

Discretization and validation

The criterion for choosing the time step is similar to that indicated in [18]. If the convective term of the energy equation of the HTF is the most restrictive than the diffusive term, a CFL number of 1 is imposed ($\Delta t = \epsilon \Delta x / v_f$). However, if the restriction of the diffusive term ($\Delta t_{diff} = \mathrm{C}(\epsilon \rho C_p \Delta x^2 / 2 k_{eff})$, where C is a constant chosen between 0.5 and 1) is more restrictive, then the time step used is the one resulting from this restriction.

The diffusive term of Eq. (5.1) has been discretized using a central difference spatial and fully implicit temporal integration schemes. The convective term is integrated using a fully explicit, 1st order scheme; and depending on the Péclet number ($\Delta x \, v_f / k_{eff}$), it is discretized either using an upwind scheme (coarser meshes) or a centered scheme (finer meshes), avoiding unboundedness problems for the one side and high numerical diffusion for the other. Therefore, when the mesh is coarse and the centered scheme is not used for the convective term, the time step is determined by the latter and the CFL number is set to 1. On the other hand, when the grid is fine enough, the diffusive term poses a higher (or comparable) restriction to the time step than the convective term, in which case the centered scheme is used and the CFL number is lower than 1. For further details on the discretization procedure please refer to [18].

The validation of the model was performed against two cases, one of a thermocline tank filled with a mixture of Quartzite rock and sand (experimental work of Pacheco et al. [5]) and another of a packed bed of encapsulated PCM (experimental work of Nallusamy et al. [25]). Both cases are presented in [18].

5.2.2 Tank walls, insulation and foundation

The models used for simulating the heat transfer through the tank walls, insulation and foundation are those presented in [26, 27]. A transient heat balance is performed to find the temperature of the tank walls (container + insulation) in each tank section. For the foundation, a simplified zonal 1D model has been used. More details about the formulation used for these components can be found in references [26, 27].

5.3 Cases of isolated TES under nominal conditions

Two levels of analysis are carried out in this work. The first one is developed in this section, consisting in an isolated analysis of the different TES configurations, under specific operating conditions. Therefore, flow inlet conditions are constant (and equal) for both charge and discharge processes, and no thermal losses to the ambient (nor to the walls and foundation) are considered. Thermal performance is evaluated after reaching a periodic state, which is achieved when consecutive charge/discharge cycles result in the same stored/released energy. With this, thermal performance is independent of the initial state of the first charge/discharge cycle.

Different configurations of thermocline tanks are considered by changing the filler material used. Single-solid, single-PCM and MLSPCM configurations are tested and compared against the ideal performance (no thermal losses) of the two-tank system considered as a reference. The dimensions of one tank of the two-tank molten-salt reference system are 13m height by 38m diameter (adopted from those of Andasol 1 facility [28]). Single-tank systems will be firstly designed with these same dimensions, and finally the diameter will be increased for one selected MLSPCM configuration in order to achieve the same thermal storage in the periodic state as with the molten salt system.

TES charge and discharge processes are carried out with molten salt at 390°C and 290°C, entering through the inlets placed at its top and bottom, respectively. A mass flow of 948 kg/s is assumed, which is the nominal value for Andasol 1 plant [28].

Furthermore, the following operating conditions are assumed:

- Operating time is not fixed but depends on the temperature of the fluid coming out of the tank at each process. Temperature thresholds are imposed to avoid outlet temperatures too cold or too hot to be sent to the receiving equipment (i.e solar field and power block). The temperature ranges between the thresholds and the highest (discharge) or lowest (charge) will be referred to as "admissible" temperature ranges. Each process is stopped when the temperature of the fluid coming out of the tank goes out from these admissible ranges.

  Here, both ranges have been assumed to be 15% of the maximum temperature interval (100°C); i.e. 290-305°C for the charging process and 375-390°C for the discharge.

- Ambient losses are neglected [$U_{TC-Sh} = 0$ in Eq. (5.1)].

- Several consecutive charge/discharge cycles are simulated until a periodic thermal state is reached, i.e. when there is negligible variation of the stored/released energy between consecutive cycles. Since ambient losses are neglected, the same energy that is stored in the charge must be released in the discharge at the periodic state.

Since the admissible temperature intervals for both charge and discharge processes are quite narrow, outlet fluid temperatures for all the cases are very similar. Therefore, a higher operation time is directly related to a higher stored (or released) energy.

In Table 5.1, a code for each prototype/configuration is defined. The thermocline-like prototypes can be classified according to the filler material/s used as: single-solid (A); single-PCM (B) and multi-layered solid-PCM (C). Percentages between brackets indicate the portion of total height occupied by each filler material. It should be noted that the chosen PCMs are fictitious, having the same thermal properties as those of potassium hydroxide (KOH) but with different fusion temperatures. The exception is case B1, where KOH is considered with its actual melting point (360°C according to [12]). This procedure has been adopted in order to account for the variations in performance exclusively due to the change in the fusion temperature of the PCMs. Figure 5.2 depicts a sketch of one of the prototypes tested. Table 5.2 shows the physical properties used in the simulations. The solid filler material adopted here is a mixture of quartzite rock and sand [5]. For the filler material, both PCM and solid, a diameter of 15mm is adopted. Porosity is 0.4 for the PCM layers and 0.22 for the packed bed of quartzite rock and sand. The volume fraction of capsules occupied by PCM is 85%.

Table 5.1: Codification of prototypes.

Filler material/s[a] - Tank dimensions	Code
2-Tank molten salt - 13m×38m	2-TANK
Quartzite rock & sand (Qu) (100%) - 13m×38m	A1
KOH (100%) - 13m×38m	B1
KOH380 (100%) - 13m×38m	B2
KOH300 (100%) - 13m×38m	B3
MLSPCM: KOH380-Qu-KOH300 (20%-60%-20%) - 13m×38m	C1
MLSPCM: KOH380-Qu-KOH300 (5%-90%-5%) - 13m×38m	C2
MLSPCM: KOH380-Qu-KOH300 (5%-90%-5%) - 13m×43.7m	C3
Quartzite rock & sand (Qu) (100%) - 13m×43.7m	A2

[a]Materials KOHXXX (where XXX is a 3 digit number) are fictitious PCMs with fusion temperatures indicated by the number XXX (e.g. 300°C), whose thermal properties are equal to those of KOH (whose fusion temperature is 360°C). The order in which the materials are indicated is the one in which they are placed inside the tank, from the top to the bottom. Between brackets, the proportion of the tank height occupied by each filler layer is indicated.

Table 5.3 shows the mass of solid filler material, PCM and HTF contained for each prototype. Due to the higher porosity of the PCM layers, the configurations including encapsulated PCMs have a higher amount of confined heat transfer fluid. Furthermore, as the solid filler material is more dense than the PCM, a higher amount

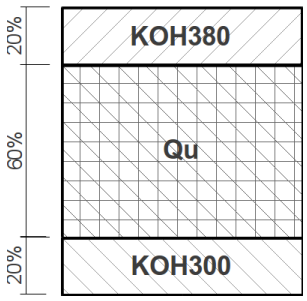

Figure 5.2: Sketch of MLSPCM prototype C1.

Table 5.2: Thermo-physical properties

	Quartzite rock & sand [30]	PCM [12]	Molten Salt [29]
$\rho\ [kg/m^3]$	2500	2040	1873.8
$C_{p,s}\ [J/kg\,K]$	830	1340	-
$C_{p,l}\ [J/kg\,K]$	-	1340	1501.5
$k_s\ [W/m\,K]$	5.69	0.5	-
$k_l\ [W/m\,K]$	-	0.5	$0.443 + 1.9 \times 10^{-4} T(^{\circ}C)$
$\mu\ [Pa\,s]$	-	-	$22.714 \times 10^{-3} - 0.12 \times 10^{-3} T + 2.281 \times 10^{-7} T^2 - 1.474 \times 10^{-10} T^3$
$L\ [J/kg]$	-	1.34×10^5	-

of the former results in a higher total mass. The same table also presents data of the storage capacity for each configuration, i.e. the maximum amount of energy that could (theoretically) be stored taking into account both sensible and latent energy contributions, with a temperature jump of 100°C (290°C- 390°C). In the case of the 2-tank system, the stored energy at the periodic state is equal to the capacity, since this system is not affected by the phenomenon of thermocline degradation and the thermal losses to the ambient are not considered in this part of the study.

5.3.1 Results and discussion

Table 5.4 shows the quantitative results obtained from the simulation of the different cases considered, after the periodic steady state has been reached. The different cases

Table 5.3: Mass confined inside the tank and storage capacity

Mass data (ton)	2-TANK	A1	B1	B2	B3	C1	C2	C3	A2
Mass of PCM	0.0	0.0	13013.4	13013.4	13013.4	5205.4	1301.3	1721.0	0.0
Mass of solid filler material	0.0	28749.8	0.0	0.0	0.0	17249.9	25874.8	34219.5	38021.6
Mass of confined HTF	27629.3	6078.4	11051.7	11051.7	11051.7	8067.8	6575.8	8696.5	8038.7
Total mass	27629.3	34828.3	24065.2	24065.2	24065.2	30523.0	33752.0	44637.0	46060.4
Storage Capacity									
Filler material (MWh)	0.00	662.84	968.78	968.78	968.78	785.22	693.44	917.07	876.61
Confined HTF (MWh)	1152.36	253.52	460.94	460.94	460.94	336.49	274.26	362.71	335.28
Total (filler+HTF) (MWh)	1152.36	916.36	1429.72	1429.72	1429.72	1121.71	967.70	1279.78	1211.89
Total sensible energy (%)	100.0	100.0	66.1	66.1	66.1	82.7	95.0	95.0	100.0
Total latent energy (%)	0.0	0.0	33.9	33.9	33.9	17.3	5.0	5.0	0.0

(or prototypes) are divided into two groups, one in which the tank dimensions are the same as those of the 2-tank system, and another in which the diameter of the tank is increased.

Results depicted in Table 5.4 correspond to simulations run with a grid with $N_x = 1040$ and $N_r = 10$. These have been checked to be good in terms of grid independence, since comparing against results obtained with a grid with double resolution (for some cases), the differences in the values of stored energy were lower than 0.6%.

Prototypes with tank dimensions of 13m $\times$ 38m

Cases A1 to C2 correspond to different thermocline configurations of tanks with the same dimensions as that of a single tank of the 2-tank system (13m $\times$ 38m).

As seen in previous works [18,19], the single-solid-filled thermocline tank shows a degradation of the thermocline throughout consecutive charge/discharge cycles, due to the restrictions on the outlet fluid temperature. As a result, the stored energy at the periodic state is around 80% of its storage capacity. This value is higher than that obtained for the small scale prototype tested in [18] (with dimensions of 5.2m $\times$ 3m), where a utilization of around 63% of the capacity was obtained. The reason for this is that the thermocline height in both cases is similar —around 2m in the case of [18] and 3m in the present case (see fig. 5.3)—while the height of the tank is very different,

resulting in a lower thermocline zone relative to the height for the case presented here ($\sim$ 23% vs. $\sim$ 33.3%).

Case A2 results in both delivered energy and exergy to the PB of $\sim$64% with respect to the obtained with the 2-tank system.

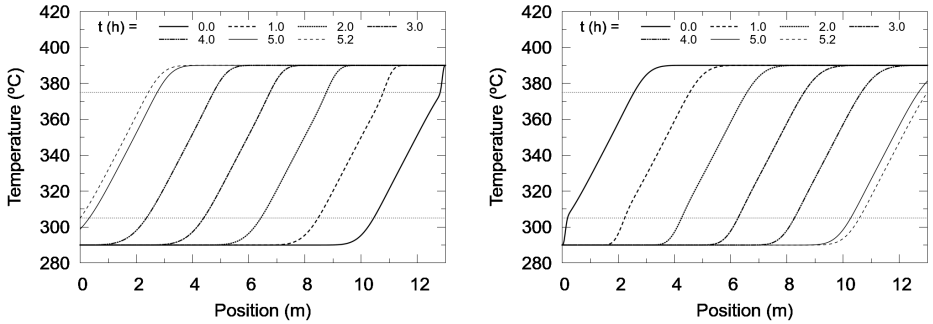

(a) Charge (b) Discharge

Figure 5.3: Case A1. Periodic state. Temperature maps at various instants. The chronological order of the curves is from right to left for the charge process and from left to right for the discharge. Horizontal dotted lines indicate the threshold temperatures.

Prototype of case B1 is filled with a single encapsulated PCM with a fusion temperature of 360°C (KOH) which is outside both admissible temperature ranges for the outgoing fluid. As in [18], the thermal performance of the prototype filled with this encapsulated PCM is the worst of all the cases studied. The percentage of PCM effectively changing phase between processes is very low (2.3%) and also the usage of the storage capacity (30%).

Figure 5.4 shows the temperature maps for the periodic state. It can be observed that the area between the initial and last temperature curves is very small, resulting in a very low utilization of the sensible energy capacity of the system.

Table 5.4: Performance results for each configuration

	Diameter = 38m							Diameter = 43.7m	
Results	2-tank	A1	B1	B2	B3	C1	C2	C3	A2
Operation time (h)[a]	8.10	5.18	3.06	6.61	6.61	7.12	6.43	8.54	6.88
Stored Energy in Filler material (MWh)	0.0	529.7	226.6	501.6	501.5	659.2	645.8	857.7	703.4
Stored Energy (Filler + confined HTF) (MWh)	1152.4	732.7	432.4	902.6	902.5	937.6	894.6	1188.7	972.9
Stored Energy / Storage capacity (%)	100.0	80.0	30.2	63.1	63.1	83.6	92.4	92.9	80.3
Stored Energy / Stored Energy in 2-tank (%)	100.0	63.6	37.5	78.3	78.3	81.4	77.6	103.2	84.4
Sensible energy stored / Total stored (%)	100.0	100.0	97.4	90.9	90.9	80.5	94.8	94.8	100.0
Latent energy stored / Total stored (%)	0.0	0.0	2.6	9.1	9.1	19.5	5.2	5.2	0.0
Effective mass of PCM changing phase (%)	-	-	2.3	16.9	16.9	94.3	95.3	96.0	0.0
Exergy difference at charge (MWh)	-553.2	-352.0	-207.7	-433.4	-436.2	-453.2	-430.3	571.8	-467.4
Exergy difference at discharge (MWh)	553.2	351.6	207.3	430.54	433.3	447.3	428.7	569.7	466.8
Exergy at discharge / Exergy at discharge of 2-tank (%)	100.0	63.5	37.5	77.8	78.3	80.9	77.5	103.0	84.4
Pumping energy / Stored Energy (%)	0.08	0.09	0.09	0.09	0.09	0.09	0.09	0.09	0.09

[a] In cases where the charge and discharge operation times are different, (e.g. B2 and B3) the mean value between processes is shown.

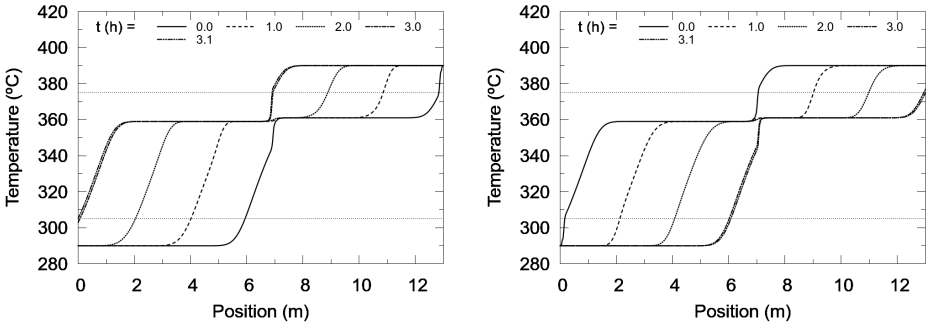

(a) Charge (b) Discharge

Figure 5.4: Case B1. Periodic state. Temperature maps at various instants. The chronological order of the curves is from right to left for the charge process and from left to right for the discharge. Horizontal dotted lines indicate the threshold temperatures.

Cases B2 and B3 have the common feature of using PCMs whose melting points lie inside each of the admissible temperature ranges. Temperature maps for the periodic state of both cases are shown in figures 5.5 and 5.6. A first observation is that the area between the initial and final maps for both cases is significantly higher than that of case B1. As a result, a higher utilization of the storage capacity, and thus, a higher stored energy, is obtained with these prototypes. Due to the symmetry between key temperatures of cases B2 and B3 (melting points, thresholds and operating range), the resulting temperature maps for the periodic state are also symmetric and the thermal performance results for both cases are almost identical. It can be observed that the efficiency in the use of the phase change material and of the whole storage capacity are much higher than that of prototype B1, but not yet ideal (17% and 63%, respectively, for both B2 and B3).

Cases C1 and C2 are MLSPCM configurations with only two different PCMs collocated at both extremes of the tank and a solid filler material (quartzite rocks & sand) in the middle zone, forming a 3-layer arrangement, only differing in the width of the layers. Figure 5.2 shows a sketch of the configuration of prototype C1. Due to the symmetry of the operating conditions, the design of the filler materials configuration is also symmetric. The PCMs used are those whose melting points are contained in the admissible temperature ranges for the outgoing fluid in both processes, KOH380 and KOH300.

In [18], it was observed that only the energy contained in the HTF between the inlet temperature and the melting point of the PCM located at the inlet can be "used" for producing the phase-change of the PCM, at most. This is, in the charge process,

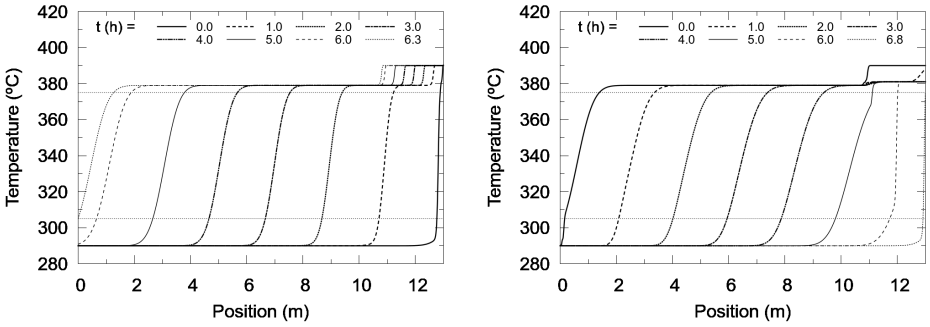

(a) Charge (b) Discharge

Figure 5.5: Case B2. Periodic state. Temperature maps at various instants. The chronological order of the curves is from right to left for the charge process and from left to right for the discharge. Horizontal dotted lines indicate the threshold temperatures.

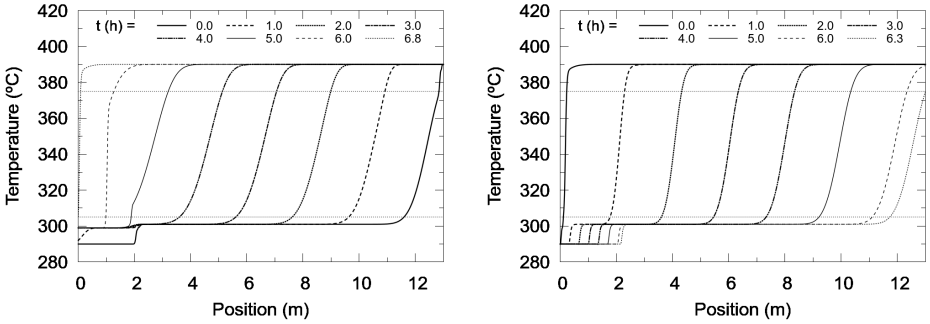

(a) Charge (b) Discharge

Figure 5.6: Case B3. Periodic state. Temperature maps at various instants. The chronological order of the curves is from right to left for the charge process and from left to right for the discharge. Horizontal dotted lines indicate the threshold temperatures.

only the energy contained between 390°C (inlet) and 380°C is available for melting the PCM layer of KOH380 (located at the top). Therefore, as only 10-12% of the whole energy available to be stored can be used for producing the phase-change of each PCM layer, then only 20-24% of the energy can be stored/released in the form of latent energy. Hence, in order to assure that most of the PCM will effectively undergo

a change of phase, configurations with a latent energy capacity of less than 20% are considered here. Observe, from Table 5.3, that prototype C1 has a latent energy capacity of 17% of the total storage capacity and this value is only 5% in C2.

Performance results of these two cases, are the best in terms of efficiency in the use of the storage capacity (C1 84%, C2 92%) and in the use of the latent energy (94-95% of the PCM changing phase between processes). In terms of total energy and exergy delivered, their results are similar to those obtained in cases B2 and B3, with around 78-81% of those obtained in the 2-tank system. All this is possible with the use of a relatively small amount of encapsulated PCM, being most of the tank filled with the cheaper solid material.

Figures 5.7 and 5.8 show the temperature maps after reaching the periodic state, where the thermal buffering effect of the PCMs collocated at both ends of the tank can be observed. In each process, phase changing capsules located close to the fluid outlet, force the temperature of the outgoing HTF to remain close to the PCM melting point, and thus, inside the corresponding admissible range. This allows a longer operating time and a higher thermal filling of the whole tank.

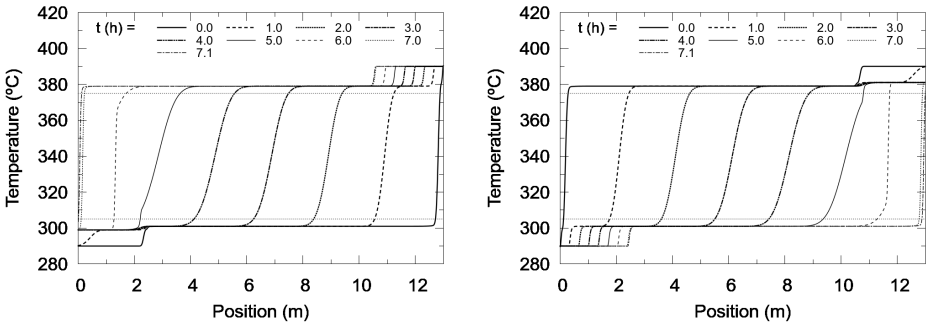

(a) Charge (b) Discharge

Figure 5.7: Case C1. Periodic state. Temperature maps at various instants. The chronological order of the curves is from right to left for the charge process and from left to right for the discharge. Horizontal dotted lines indicate the threshold temperatures.

Regarding the pressure losses produced by the presence of the filler material, it can be seen that they are negligible (less than 1% of total pressure losses). Pumping energy needed to overcome these, plus the gravitational force, represent less than 0.1% of the stored energy for all cases.

In summary, compared against solid-filled thermocline design, MLSPCM concept present higher storage capacity together with a higher efficiency in its utilization.

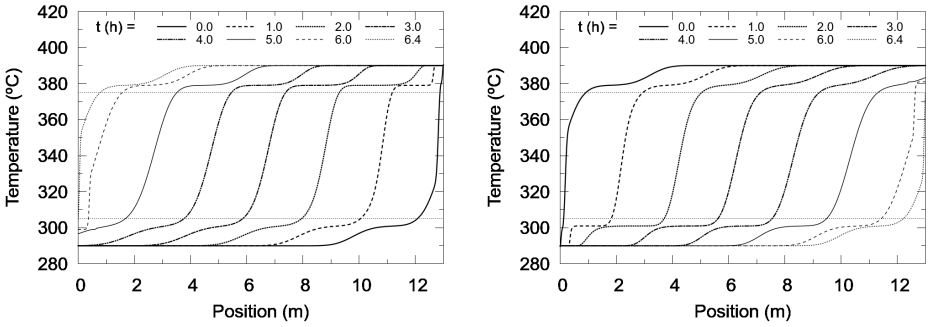

(a) Charge (b) Discharge

Figure 5.8: Case C2. Periodic state. Temperature maps at various instants. The chronological order of the curves is from right to left for the charge process and from left to right for the discharge. Horizontal dotted lines indicate the threshold temperatures.

Furthermore, although presenting lower overall capacity, MLSPCM prototypes yield a much higher efficiency than single-PCM ones, resulting in similar values of total energy storage.

Prototypes with larger diameter (13m $\times$ 43.7m)

Prototype C2 is probably the most cost-effective among those including encapsulated PCMs, due to its high efficiency and low amount of PCM used. However, in order to yield the same values of energy —and more precisely, exergy — delivered to the power block as those of the 2-tank molten-salt system, the storage capacity of the single-tank system has to be increased. Hence, the tank diameter is enlarged.

Case C3 corresponds to this new case, with a tank diameter of 43.7m, where thermal performance values can be seen to be very similar to those of the ideal 2-tank system. The stored/released energy and exergy delivered to the PB are around 3% higher than with the 2-tank, while the efficiencies in the use of the total and latent capacities are very high.

This prototype has a volume 32% higher than one tank of the 2-tank system and requires around 68% less amount of molten salt than the latter. On the other hand, it needs to hold around 62% more weight and requires two small layers of encapsulated PCM (with less than 4% of total weight).

Case A2, which has the same tank dimensions as C3 but is totally filled with solid material, results in an effective storage of around 84% with respect to that of the 2-tank system and around 84% with respect to the obtained with C3.

Figures 5.9 and 5.10 depict the temperature maps of these two cases in the periodic state. It can be observed how the inclusion of the PCM layers induce a higher utilization of the sensible energy capacity of the tank, as already observed between cases A1 and C2.

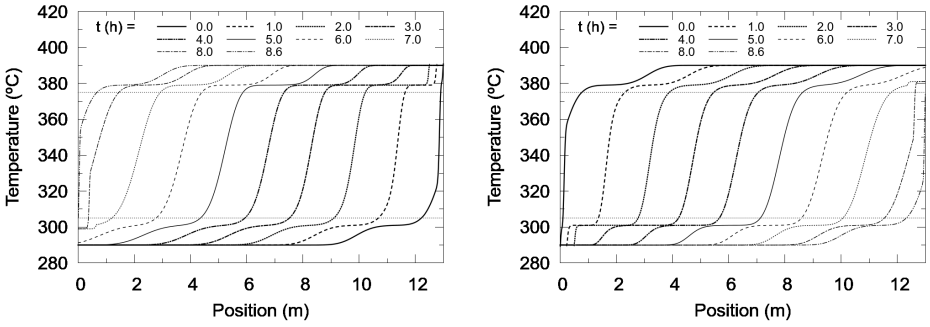

(a) Charge (b) Discharge

Figure 5.9: Case C3. Periodic state. Temperature maps at various instants. The chronological order of the curves is from right to left for the charge process and from left to right for the discharge. Horizontal dotted lines indicate the threshold temperatures.

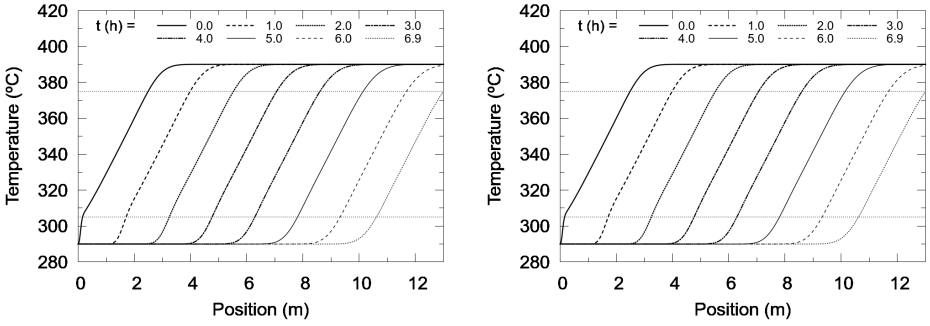

(a) Charge (b) Discharge

Figure 5.10: Case A2. Periodic state. Temperature maps at various instants. The chronological order of the curves is from right to left for the charge process and from left to right for the discharge. Horizontal dotted lines indicate the threshold temperatures.

In summary, a single-tank TES system equivalent to the reference 2-tank system, results smaller and more efficient when using an appropriate MLSPCM configuration than when using a solid-filler material.

5.4 Cases of TES integrated into a CSP facility

In this section, the analysis of the TES systems integrated into a CSP facility is performed, by taking into consideration the variations of the direct normal irradiation (DNI) on the solar field (SF), as well as the thermal energy losses to the ambient through the tank shell and foundation. Furthermore, idle processes are simulated; i.e. when there is no fluid flow through the tank.

The parameters for the reference CSP plant are shown in Table 5.5. The heat transfer fluid passing through the TES is molten salt. A sketch of the plant with a single-tank TES is shown in Fig. 5.11. The thermo-physical properties of the different materials in the packed beds are the same used for the previous cases. The efficiency of the heat exchanger intended to transfer heat between the fluids from the SF and TES is assumed to be 1.

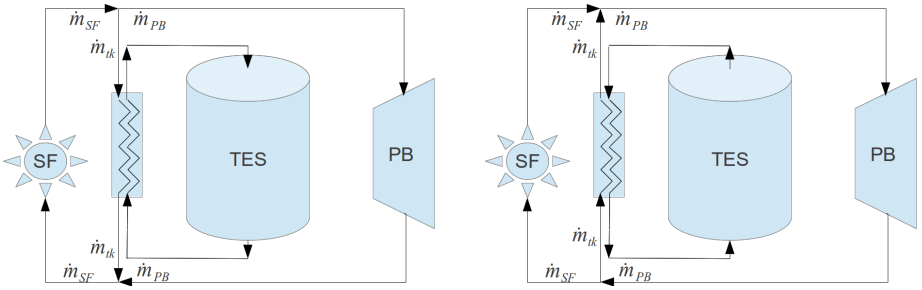

(a) Charge (b) Discharge

Figure 5.11: Sketch of CSP plant with single-tank TES.

5.4.1 Operating conditions

The same values of temperature of fluid coming from the solar field and from the power block (PB) as those of section 5.3 are adopted here, 390°C and 290°C, respectively. Furthermore, the same admissible temperature ranges are here considered, i.e. 375-390°C for the discharge and 290-305°C for the charge. However, one difference between the criterion used here and the one used in section 5.3 is that the temperature

Table 5.5: Parameters of reference CSP plant

Turbine nominal power (MWe)	50
Solar field technology	Parabolic trough
Solar field area (m^2)	510120
Solar field peak efficiency (%)	70
Power block peak efficiency (%)	38
Storage capacity w/ 2-tank system (MWhth)	1152

limits are not applied to the fluid flows coming out of the TES directly. Instead, the controlled temperature is that of the fluid coming into both, the SF and the PB. Hence, if the TES is being charged and the PB is generating power simultaneously, the fluid entering the SF is a mixture of the fluid streams coming from the PB and from the TES heat exchanger (see the sketch in Fig. 5.11(a)), and therefore, its temperature is not that of the cold fluid coming out of the TES but a weighted average of the temperatures of both streams. Something similar occurs with the temperature of the flow going to the PB if the TES is discharged at the same time as the SF is collecting heat (see the sketch in Fig. 5.11(b)). Therefore, the current criterion is less restrictive, from the point of view of the TES, since the temperature of the fluid coming out of it could be outside the corresponding admissible range but the process would not be stopped, as long as the temperature of the fluid coming into the receiving equipment still remains inside this range.

To avoid several charge and discharge processes being started and stopped in small time intervals, different (more restrictive) thresholds have been defined for starting the processes; i.e. a discharge is not initiated if the temperature at the top of the tank is lower than 380°C, while a temperature at the bottom of the tank higher than 300°C is required for charging the tank.

The initial conditions for the TES, in the first day of simulation, are uniform temperatures of 290°C for the whole tank and 15°C for the soil.

The simulations are carried out for 17 days in summer (from June 30 to July 17) in Seville, Spain. The direct normal irradiation (DNI) and the rest of weather data are obtained from METEONORM software version 4.0. Table 5.6 depicts some basic information for this location.

For determining the power coming from the solar field, the following equation is used:

$$\dot{Q}_{SF} = DNI \times A_{SF} \times \eta_{SF}$$

where the DNI is multiplied by the surface area (A_{SF}) and overall efficiency of the solar field (η_{SF}), which is taken as the peak efficiency of the solar field in Andasol

1 plant [28] (see Table 5.5). It is assumed that the mass flow coming from the solar field is directly sent to the power block until the nominal power is reached, then, the excess flow is used to charge the storage system. When the mass flow from the SF is not enough to reach the nominal electric power, the TES discharge starts and the mass flow passing through the heat exchanger, placed between the SF and TES, is calculated as the difference between the mass flow coming from the SF and that needed for generating nominal power in the PB. The discharge continues until the threshold temperature is reached ($T_{PB} < 375$ °C). After this, an idle process takes place until there is excess energy available to charge again the storage system.

The nominal thermal power, from the point of view of the TES, is calculated as

$$\dot{Q}_{PB,nom} = \frac{\text{Nominal power}}{\eta_{PB} \times 0.98} = 134.26 \text{ MW}$$

where 0.98 is the assumed efficiency of the heat exchanger of the PB (not shown in figure 5.11) and η_{PB} is the efficiency of the PB (see Table 5.5).

From this value, the nominal molten salt mass flow passing through the TES is calculated as

$$\dot{m}_{HTF,nom} = \frac{\dot{Q}_{PB}}{C_{p,HTF} \times \Delta T_{HTF}} = 894.2 \text{ kg/s} \tag{5.5}$$

where ΔT has been taken as 100°C (290-390°C). This value is a little lower than the one used in section 5.3 (948 kg/s), which corresponds to that of Andasol 1 plant according to [28]. Therefore, $\dot{m}_{HTF,nom}$ is the mass flow passing through the TES in the discharge, when there is no available energy from the SF.

Table 5.6: Location basic data

			July		
Location	Latitude (º)	Longitude (º)	T_{max} (°C)	T_{min} (°C)	DNI (kWh/m^2 day)
Seville, Spain	37.37	5.97	39.6	16.2	7.58

In figure 5.12, the curves of thermal power coming from the SF, thermal power needed to generate the nominal (electric) power in the PB and the remaining thermal power available to be stored in the TES, are plotted for the time range of the simulations.

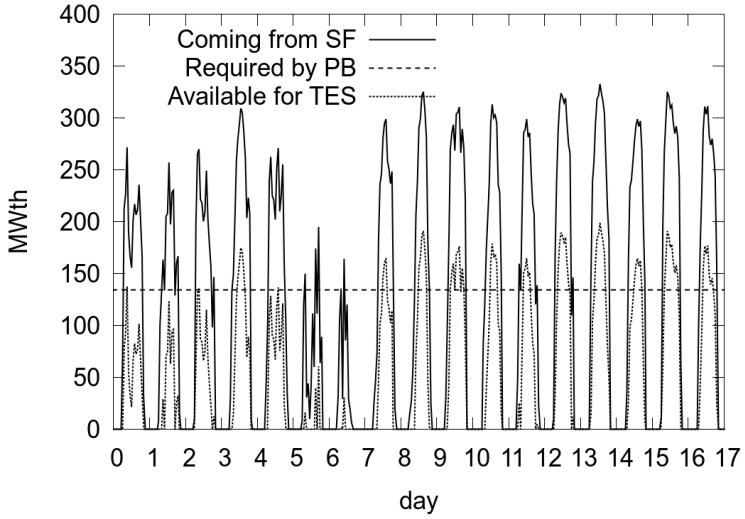

Figure 5.12: Thermal power (in MW) coming from the solar field, required by the power block (for nominal power generation) and available for storage, in the 17 days of simulation.

5.4.2 Tank configurations

The same configurations tested in the simplified case (Table 5.1) are here tested, with the addition of the tank shell, insulation and foundation.

The tanks are made of steel A516gr70, while the insulation material for the lateral wall and roof is Spintex342G-100. The insulation is covered with a thin layer of aluminum 2024 T6.

Common geometric parameters for all the cases:

- Vertical wall thickness, e = 0.039 m.
- Bottom wall thickness, e = 0.021 m.
- Insulation thickness: e = 0.4 m.
- Foundation thicknesses: dry sand, e = 0.006 m; foam-glass, e = 0.420 m; heavy weight concrete, e = 0.450 m; soil, e = 9.140 m.

The thermo-physical properties of all the used materials can be found in [26].

5.4.3 Results and discussion

Table 5.7 shows the results for all the presented cases, which are expressed as mean values, per day, of the 17 days of simulation.

Firstly, it can be seen that the reference 2-tank TES shows zero energy losses, due to being considered as the ideal case, i.e. the hot tank is always at 390°C and the cold tank at 290°C. However, the storage capacity is not entirely used because of the fact that not in some days there is not enough available energy (from the SF) to fill the 2-tank system completely. On the other hand, in some days there is an excess of energy and some has to be discarded (see the "unused available energy" row in Table 5.7), probably by defocusing some collector lines in the solar field.

In the last row of Table 5.7, the number of days for which the temperature threshold is reached by the outlet fluid in the charging process is presented. This can be seen as the number of days in which the effective thermal capacity is exhausted. The term "effective" is used in order to differentiate between the capacity indicated in Table 5.3, which is the ideal capacity and does not depend on the temperature thresholds, and the "real" one which is the one that results from the simulations with the restrictions in the outlet temperature. In the case of the 2-tank, since the threshold is never reached, the number of days in which the system is totally charged is indicated.

The fact of not exhausting the effective capacity in every day of simulation distinguishes the present operating conditions from those of section 5.3, since in the latter the charge was not stopped until the temperature threshold was reached.

The differences in the values of total energy coming from the SF and available energy for storage, between the different prototypes, is due to interpolation errors of the input data. These are available at intervals of one hour and are needed for each time step of simulation, with a frequency in the order of seconds and dynamically determined by the code, resulting in different interpolation steps for each case.

Table 5.7: Performance results for each configuration.

Results	Diameter = 38m							Diameter = 43.7m	
	2-tank	A1	B1	B2	B3	C1	C2	C3	A2
Total energy from SF (MWh)	2798.6	2776.3	2776.1	2776.1	2780.8	2776.3	2776.3	2776.6	2776.3
Energy available for charging the TES (MWh)	1151.0	1125.8	1126.2	1126.1	1126.2	1125.8	1125.8	1125.8	1125.8
Energy delivered to the PB by the TES (MWh)	959.4	715.3	397.0	794.6	762.4	805.7	777.3	963.6	879.0
Energy delivered by TES / TES capacity (%)	83.3	78.1	27.8	55.6	53.3	71.8	80.3	75.3	72.5
Energy delivered by TES / Delivered by 2-tank (%)	100.0	74.6	41.4	82.8	79.5	84.0	81.0	100.4	91.6
Energy losses (MWh)	0.0	3.4	3.6	3.3	3.4	3.4	3.4	4.2	4.3
Energy losses / Energy delivered to PB by TES (%)	0.0	0.4	0.9	0.4	0.4	0.4	0.4	0.4	0.5
Exergy delivered to the PB by the TES (MWh)	460.6	343.2	190.3	379.1	365.7	384.4	372.4	461.6	421.7
Exergy Delivered/ Delivered by 2-tank (%)	100.0	74.5	41.3	82.3	79.4	83.5	80.8	100.2	91.5
Unused available energy (MWh)	191.6	402.9	692.1	221.7	330.5	311.3	342.9	154.8	236.1
Nº of days in with the charge is stopped by threshold	10[a]	13	14	12	12	12	12	9	11

[a]Temperature thresholds are never reached by the 2-tank TES, and therefore, the number of days correspond to those when the system is totally charged.

For the solid-filled thermocline prototype A1, the values of energy and exergy delivered to the PB are lower than those obtained with the 2-tank (74.5%). However, these differences are not as high as those shown in section 5.3. This is in part due to the variability of the available energy for storage, which in some days is lower than the storage capacity, and also to the less restrictive operating conditions for the TES (mentioned above), which allow a greater thermal filling than that allowed in section 5.3. Figure 5.13 shows the initial and final temperature maps for charge and discharge processes in the 10^{th} day, with durations of more than 6 hours each. It can be observed that the final temperature at the charge goes beyond the threshold (305°C) due to the mixing effect mentioned before, and that the tank is thermally filled to a higher extent than in section 5.3 (compare with Fig. 5.3). The difference between the temperature maps at the end of the charge and at the start of the discharge is because an idle process of around 5.5 hours and another charge of around 18 minutes occur between them. Comparing the number of days in which the storage tank "effective" capacity is exhausted, it is observed that this happens in 10 days for the 2-tank system and in 13 for A1. As mentioned above, this explains why the efficiency in the use of total capacity is closer between the 2-tank and A1 prototypes than in section 5.3, where all the prototypes were charged until reaching the threshold temperature.

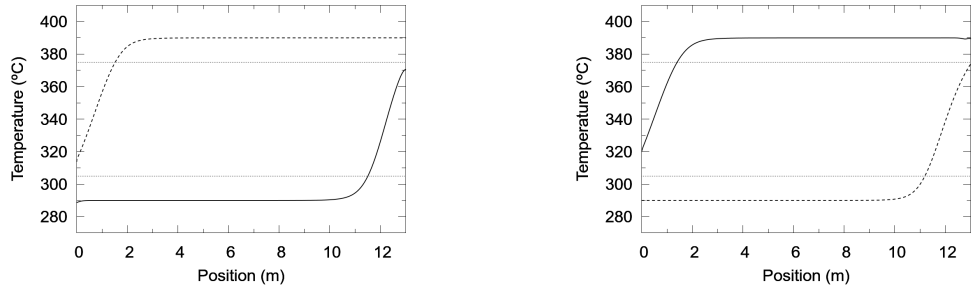

(a) Charge (b) Discharge

Figure 5.13: Temperature maps of day 10 for charge and discharge processes for prototype A1. Solid line indicates the temperature at the start of the process and dashed line at the end. Horizontal dotted lines indicate the threshold temperatures.

For prototype B1, the results are much worse, being in agreement with those obtained previously. Similarly as in section 5.3, the results for prototypes B2 and B3 are much better than for B1 and comparable to those of C2, in terms of total energy and exergy delivered, but worse than the latter in terms of efficiency.

MLSPCM prototypes C1 and C2 result in a storage of around 84% and 80% compared to the 2-tank, respectively. Their efficiency in the use of total capacity is

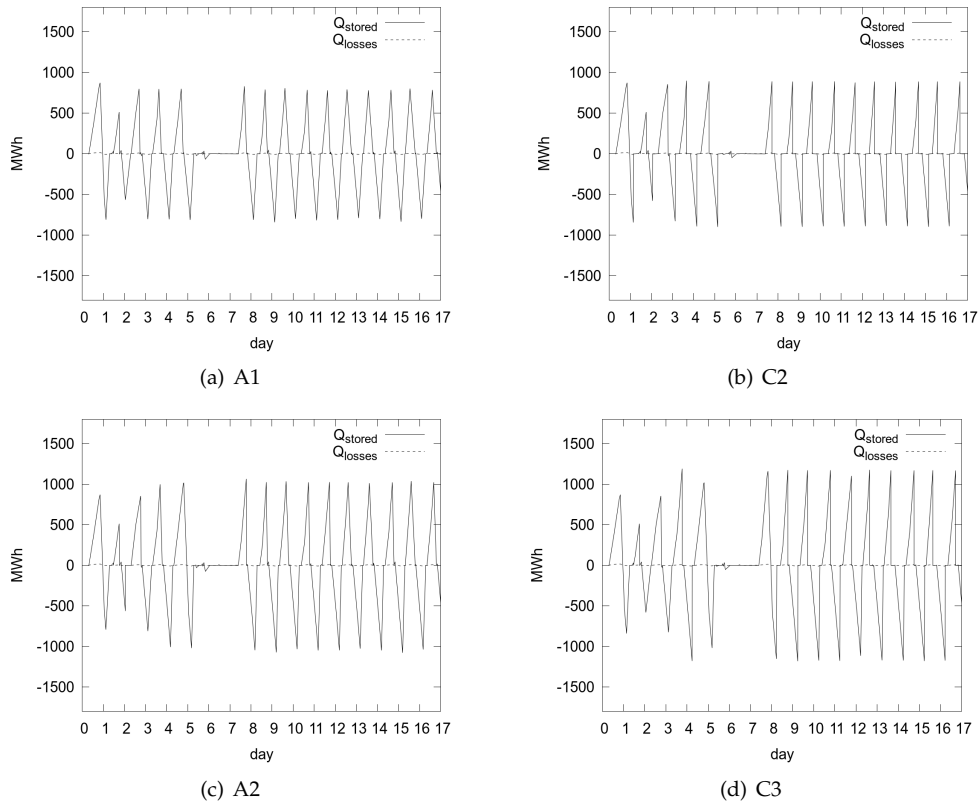

(a) A1 (b) C2

(c) A2 (d) C3

Figure 5.14: Evolution of the energy stored and lost for several prototypes. Values are reset to 0 at the end of each process. Stored energy (continuous line) has positive values in the charge and negative values in the discharge. Thermal losses (dashed line) are positive when heat comes out of the packed bed (by conduction through the walls) and negative when it comes into it.

lower than that obtained in section 5.3, which again, is mostly due to the occurrence of days of low radiation in which the available energy is not enough to fill the TES. Hence, the total energy effectively stored is closer to that obtained by prototype A1, although still higher. C2 still results in a higher use of the storage capacity than A1, but C1 shows a lower value.

Prototype C3, which has the same configuration as C2 but with a higher diameter, is seen to result in almost the same amount of exergy delivered to the power block as in the 2-tank system, and therefore it is considered as equivalent to the latter, since

it would result in almost the same amount of power generation. When comparing energy efficiencies of prototypes C3 and A2 it can be observed that it is higher in the former than in the latter (75.3% vs 72.5%), but still very similar. Case A2 delivers 91.5% of the exergy delivered by the ideal 2-tank. This is 9% lower than that achieved by the C2 configuration.

In Fig. 5.14, the energy stored and lost for prototypes A1, C2, A2 and C3 are plotted for each day. It can be seen that in the first days there is a significant variation of stored/delivered energy and from the 8^{th} day on, it is stabilized. This is due, on the one hand, to the particular initial conditions of the first day (uniform low temperature), and on the other, to the DNI variations in the first seven days. Particularly, in days 6 and 7 all the TES remain uncharged due to the low amount of available irradiation.

In all cases, the thermal losses are very low (less than 1% of the energy delivered to the PB by the TES for all the cases, and around 0.5% for most), which is an indication of having enough thermal insulation. Due to the transient operation of the tanks, in the discharge processes heat comes into to the packed bed through the tank walls and foundation instead of coming out, and therefore, these components act as additional thermal storage media.

5.5 Conclusions

MLSPCM thermocline-like thermal energy storage prototypes have been designed for their utilization in a CSP plant. A parabolic trough plant of 50MWe, similar to Andasol 1 (Granada, Spain), has been adopted as reference. The analysis has been carried out using verified and validated models of the thermocline-like configurations, tank walls and foundation.

Two different analyses were performed, one centered in evaluating the performance of the TES systems under specific conditions, in which the TES is charged and discharged consecutively until reaching a periodic steady state; and another in which the same TES configurations are tested under 17 days of operation in the reference CSP plant. In the latter case, weather conditions of Seville (Spain) were adopted, the variation of the operating conditions due to the changes in the direct normal irradiation were simulated, and the tank walls and foundation were taken into account.

MLSPCM single-tank systems, with the same tank dimensions as one of the two-tank molten salt tanks, were compared to the latter system as well as to other single-tank configurations. Furthermore, one of the MLSPCM configurations was chosen for designing a bigger tank, aimed to achieve the same amount of energy stored as that of the two-tank system.

The first analysis confirms the conclusions taken in previous works [18,19], indicating that MLSPCM configurations diminish the degradation of the thermocline of

single-tank solid-filled designs, produced by the restrictions in the outflow temperature. Hence, both total capacity and the extent at which it is harnessed are increased. Compared against single-PCM packed beds, MLSPCM designs yield a much higher efficiency in the use of total capacity, especially when the amount of PCM effectively changing phase is evaluated. Compared against the two-tank system, MLSPCM prototype C3 is considered as its equivalent in terms of energy and exergy delivered to the power block, with a volume 32% higher than that of one of the two tanks and needing only 32% of the amount of molten-salt. On the other hand, the total weight hold by C3 is 62% higher and it needs a relatively small amount of PCM (less than 4% of total weight). If the comparison is performed against a single-solid filled thermocline tank with the same dimensions (i.e. prototype A2), C3 stores around 20% more energy/exergy, holding almost the same weight (around 3% less) and needing around 8% more molten-salt, besides the extra PCM layers.

The second analysis, incorporating more aspects related to the operation of the CSP plant, result in lower differences between the performance of MLSPCM and single-solid thermocline configurations. On one hand, the restrictions on the temperature of the heat transfer fluid are not applied to the flow coming out of the TES, but to that entering the solar field or the power block. This change results in less restrictive operating conditions for the TES, and therefore, the thermocline degradation occurring in the single-solid filled thermocline is not so high. Furthermore, the fact of having days of low radiation result in a penalization of the capacity factor of the systems with higher capacity. Nevertheless, in this analysis, the MLSPCM prototypes tested still show higher values of stored energy/exergy and efficiency (C2 and C3) than single-solid thermocline tanks. When compared against the reference 2-tank system, prototype C3 is still considered equivalent to it, since the values of stored energy and exergy are almost exactly the same. In these conditions, prototype A2 delivers around 10% less energy/exergy to the power block than C3 in the 17 days of simulation.

Thermal losses to the ambient are observed to be very low for all the cases (less than 1%), and the tank walls and foundation act as extra thermal storage media.

As in previous works, MLSPCM concept shows to be promising as an alternative to the other TES configurations tested, as well as to the standard two-tank system. However, variability of operating conditions are seen to affect the relative advantage of using one or another TES system, and therefore, it is possible that TES designs which are optimal for the isolated conditions are not so for the real application. Optimization of MLSPCM designs to one or another CSP facility needs to be studied in further detail, with long-term simulations incorporating all the relevant aspects, such as the real limitations for the HTF temperature, the different thermo-physical properties of the available PCMs and the economic evaluation.

Acknowledgments

This work has been financially supported by the *Ministerio de Economía y Competitividad, Secretaría de Estado de Investigación, Desarrollo e Innovación*, Spain (ENE-2011-28699), by the EIT via the KIC InnoEnergy TESCONSOL project (ref. 20_2011_IP16) and by the *Secretaria d'Universitats i Recerca (SUR) del Departament d'Economia i Coneixement (ECO) de la Generalitat de Catalunya* and by the European Social Fund.

References

[1] M. Medrano, A. Gil, I. Martorell, X. Potau, and L. F. Cabeza, "State of the art on high temperature thermal ebergy storage for power generation. part 2—Case studies," *Renew. Sust. Energ. Rev.*, no. 14, pp. 56–72, 2010.

[2] G. J. Kolb, C. K. Ho, T. R. Mancini, and J. A. Gary, "Power tower technology roadmap and cost reduction plan," Tech. Rep. SAND2011-2419, Sandia National Laboratories, 2011.

[3] U. Herrmann, B. Kelly, and H. Price, "Two-tank molten salt storage for parabolic trough solar power plants," *Energy*, vol. 29, pp. 883–893, 2004.

[4] J. I. Ortega, J. I. Burgaleta, and F. M. Téllez, "Central receiver system solar power plant using molten salt as heat transfer fluid," *J. Sol. Energ.-T. ASME*, vol. 130, pp. 024501–1–6, 2008.

[5] J. E. Pacheco, S. K. Showalter, and W. J. Kolb, "Development of a molten-salt thermocline thermal storage system for parabolic trough plants," *J. Sol. Energ.-T. ASME*, vol. 124, pp. 153–159, 2002.

[6] A. Yang and S. V. Garimella, "Molten-salt thermal energy storage in thermoclines under different environmental boundary conditions," *Appl. Energ.*, vol. 87, pp. 3322–3329, 2010.

[7] R. Tamme, D. Laing, and W. D. Steinmann, "Advanced thermal energy storage technology for parabolic trough," *J. Sol. Energ.-T. ASME*, vol. 126, pp. 794–800, 2004.

[8] J. L. Shyu, R.J. and L. Fang, "Thermal analysis of stratified storage tanks," *J. Sol. Energ.-T. ASME*, vol. 111, pp. 54–61, 1989.

[9] I. Rodríguez, J. Castro, C. Pérez-Segarra, and A. Oliva, "Unsteady numerical simulation of the cooling process of vertical storage tanks under laminar natural convection," *Int. J. Therm. Sci.*, vol. 48, pp. 708–721, 2009.

[10] L. J. Shah and S. Furbo, "Entrance effects in solar storage tanks," *Sol. Energy*, vol. 75, pp. 337–348, 2003.

[11] N. Calvet, J. C. Gomez, A. Faik, V. V. Roddatis, A. Meffre, G. C. Glatzmaier, S. Doppiu, and X. Py, "Compatibility of a post-industrial ceramic with nitrate molten salts for use as filler material in a thermocline storage system," *Appl. Energ.*, vol. 109, pp. 387–393, 2013.

[12] H. Michels and R. Pitz-Paal, "Cascaded latent heat storage for parabolic trough solar power plants," *Sol. Energy*, vol. 81, pp. 829–837, 2007.

[13] M. Liu, W. Saman, and F. Bruno, "Review on storage materials and thermal performance enhancement techniques for high temperature phase change thermal storage systems," *Renew. Sust. Energ. Rev.*, vol. 16, pp. 2118–2132, 2012.

[14] H. Shabgard, C. W. Robak, T. L. Bergman, and A. Faghri, "Heat transfer and exergy analysis of cascaded latent heat storage with gravity-assisted heat pipes for concentrating solar power applications," *Sol. Energy*, vol. 86, no. 3, pp. 816–830, 2012.

[15] K. Nithyanandam, R. Pitchumani, and A. Mathur, "Analysis of a latent thermocline storage system with encapsulated phase change materials for concentrating solar power," *Appl. Energ.*, vol. 113, pp. 1446–1460, 2014.

[16] S. M. Flueckiger and S. V. Garimella, "Latent heat augmentation of thermocline energy storage for concentrating solar power —A system-level assessment," *Appl. Energ.*, vol. 116, pp. 278–287, 2014.

[17] W. Steinmann and R. Tamme, "Latent heat storage for solar steam systems," *J. Sol. Energ.-T. ASME*, vol. 130, pp. 011004–1–011004–5, 2008.

[18] P. Galione, C. D. Pérez-Segarra, I. Rodríguez, A. Oliva, and J. Rigola, "Multi-layered solid-PCM thermocline thermal storage concept for CSP plants. Numerical analysis and perspectives." Manuscript submitted to *Appl. Energ.*, 2014.

[19] P. Galione, C. D. Pérez-Segarra, I. Rodríguez, O. Lehmkuhl, and J. Rigola, "A new thermocline-pcm thermal storage concept for CSP plants. Numerical analysis and perspectives," in *Proceedings of the SolarPACES 2013 International Conference*, vol. 49 of *Energy Procedia*, pp. 790–799, Elsevier, 2014.

[20] R. Damle, O. Lehmkuhl, G. Colomer, and I. Rodríguez, "Energy simulation of buildings with a modular object-oriented tool," in *Proc. ISES Solar World Congress 2011*, 2011.

[21] N. Wakao, S. Kaguei, and T. Funazkri, "Effect of fluid dispersion coefficients on particle-to-fluid heat transfer coefficients in packed beds," *Chem. Eng. Sci.*, vol. 34, pp. 325–336, 1979.

[22] R. Krupiczka, "Analysis of thermal conductivity in granular materials," *Int. Chem. Eng.*, vol. 7, no. 1, pp. 122–144, 1967.

[23] A. Nakayama, F. Kuwahara, and Y. Kodama, "An equation for thermal dispersion flux transport and its mathematical modelling for heat and fluid flow in a porous medium," *J. Fluid Mech*, vol. 563, pp. 81–96, 2006.

[24] R. G. Holdich, *Fundamentals of particle technology*. Midland Information Technology and Publishing, 2002.

[25] N. Nallusamy, S. Sampath, and R. Velraj, "Experimental investigation on a combined sensible and latent heat storage system integrated with constant/varying (solar) heat sources," *Renew. Energ.*, vol. 32, pp. 1206–1227, 2007.

[26] I. Rodríguez, C. D. Pérez-Segarra, O. Lehmkuhl, and A. Oliva, "Modular object-oriented methodology for the resolution of molten salt storage tanks for CSP plants," *Appl. Energ.*, vol. 109, pp. 402–414, 2013.

[27] S. Torras, C. D. Pérez-Segarra, I. Rodríguez, J. Rigola, and A. Oliva, "Parametric study of two-tank TES systems for CSP plants," in *Proceedings of the SolarPACES 2014 International Conference*, 2014.

[28] U. Herrmann and R. Kistner, "The Andasol Project," tech. rep., FLABEG Solar Int. GmbH, Solar Millennium AG, 2002. Workshop on Thermal Storage for Trough Power Systems, `http://www.nrel.gov/csp/troughnet/pdfs/uh_anda_sol_ws030320.pdf`.

[29] A. B. Zavoico, "Solar power tower design basis document," Tech. Rep. SAND2001-2100, Sandia National Laboratories, 2001.

[30] C. Xu, Z. Wang, Y. He, X. Li, and F. Bai, "Sensitivity analysis of the numerical study on the thermal performance of a packed-bed molten salt thermocline thermal storage system," *Appl. Energ.*, vol. 92, pp. 65–75, 2012.

6

Conclusions and further research

6.1 Conclusions

The present thesis was focused on the numerical simulation of thermal energy storage systems using phase change materials. Two levels of numerical analysis were addressed, one in the field of CFD, with the objective of accurately simulating complex heat transfer and fluid dynamics phenomena present in the solid-liquid phase transitions; and another one aiming at simulating whole thermal storage tanks —using solid and/or PCM filler materials— throughout several charge/discharge cycles, with several suitable simplifications and incorporating empirical correlations. Apart from the development and implementation of numerical tools, the application of thermal energy storage in CSP plants was addressed and a new concept of single-tank thermal storage was proposed.

In chapter 2, a fixed-grid enthalpy formulation for simulating the heat transfer and fluid dynamics phenomena in solid-liquid phase change probles was presented. The model was implemented into the framework of *TermoFluids* (TF), an object-oriented highly parallel CFD code intended for 3D simulations in unstructured meshes. Due to the intention of using the turbulence models already available in TF, the model was designed to be used with explicit time-integration schemes. The fluid was considered Newtonian and incompressible, and the density change between solid and liquid phases was not considered at this stage. The form of the convective term of the energy equation was discussed, and it was concluded that only the liquid phase properties should be taken into account in this term. Pressure-velocity decoupling was presented in a somewhat detailed manner, indicating its treatment in solid boundaries. The resulting system of equations of pressure was presented and its particular form in

the solid nodes was pointed out. Time integration of the momentum source term introduced by the porosity model was discussed, different expressions for the case of melting at a fixed temperature were studied and an alternative form was proposed. The implemented numerical model was tested using three different cases, and the results were compared against experimental and numerical results from the literature. Good agreement with numerical results was observed in general, since the overall behaviour of the experiments was reproduced fairly well. Some differences were encountered though, but the discrepancies were in accordance with results obtained by other authors.

Chapter 3 dealt with the extension of the fixed-grid model presented in Ch. 2, by including the variation of the thermo-physical properties with the temperature, and its application into a case of PCM melting inside a spherical capsule. The formulation and algorithms for determining the temperature and liquid porosity from the total enthalpy, for phase change occurring at both, fixed temperature or temperature range, were described. Modifications regarding different aspects, such as the treatment of the conservation equations taking into account the thermal expansion/contraction, the approach for decoupling the pressure of solid and liquid-containing domains and the determination of the source term coefficient introduced by the porous medium approach, were presented in detail. Different possibilities for the discretization of the energy equation were included. With the intention of accurately simulating the melting of n-Octadecane, a thorough search for thermo-physical properties was carried out. The correlations used were presented and discussed. Scaling of the latent heat with the density ratio when working with a unique density for both phases, was suggested. Several two and three-dimensional simulations of the case study using different discretization schemes for the convective term of the energy equation, constant and variable thermo-physical properties and two different thermal boundary conditions, were performed. Symmetry-preserving scheme showed to give more accurate results than UPWIND scheme. Different flow patterns were observed between 2D and 3D simulations, obtaining a better agreement with the experiment with 3D analyses. However, the evolution of the melting rate did not show significant differences. Accounting for the full variation of the properties with the temperature resulted in slightly higher melting rate, mostly due to the variation of thermal conductivity with the temperature. The density difference between solid and liquid phases seemed to affect mostly through its effect on the total energy needed for melting the same volume of material. Overall, a good agreement between experiment and numerical results was observed, specially for 3D simulations taking into account the variation of the thermo-physical properties with the temperature. Results obtained were closer to the experimental results than those presented by other authors [1, 2]. Discrepancies were considered to be mainly due to not taking into account a temperature range for the phase change and to not having very accurate

boundary thermal conditions.

In chapter 4, a numerical model for designing and evaluating the performance of single-tank TES systems, consisting of a porous medium of solid and/or PCM filler materials through which a heat transfer fluid flows, was presented and validated against experimental data. Furthermore, a new multi-layered solid-PCM (MLSPCM) thermocline-like thermal storage concept for CSP plants was presented. The key aspect of this new concept is the inclusion of PCM layers at both ends of the tank, whose fusion temperatures must be conveniently chosen to lie inside the predefined admissible temperature ranges for the outgoing fluid in both charge and discharge processes. These admissible temperature ranges depend on the requirements of the power generation block and the solar receivers. PCM layers act as thermal buffers, causing the outlet fluid to remain close to their melting points, and therefore inside the admissible temperature range for the corresponding process. Several simulations were carried out for different designs of thermocline tanks, which were classified according to the filler materials included as: single-solid, single-PCM, MLSPCM and cascaded PCM. Obtained results showed that MLSPCM concept prevents from the high thermocline degradation presented by the single-solid thermocline, resulting in a much higher efficiency in the use of the overall thermal storage capacity. Furthermore, MLSPCM resulted in higher storage than all the single-PCM designs tested. Compared against the cascaded PCM designs, MLSPCM showed similar values of stored energy while making use of much less encapsulated PCM, with a higher efficiency in the capacity utilization. As a conclusion MLSPCM thermocline storage systems can be regarded as a promising solution for their use in CSP plants.

In chapter 5, the MLSPCM concept was taken further into the design of full-scale TES systems for a CSP plant of 50MWe. Parabolic trough plant Andasol 1 (Granada, Spain) was adopted as reference. Two different analyses were carried out, one centered in evaluating the performance of the TES systems under specific conditions, in which the TES is charged and discharged consecutively until reaching a periodic steady state; and another in which the same TES configurations are tested under 17 days of operation in the reference CSP plant. In the latter case, weather conditions of Seville (Spain) were adopted, the variation of the operating conditions due to the changes in the direct normal irradiation were simulated, and the tank walls and foundation were taken into account. The first analysis confirmed the conclusions taken in the previous chapter, indicating that MLSPCM configurations diminish the degradation of the thermocline of single-tank solid-filled designs, produced by the restrictions in the outflow temperature. Both total capacity and the extent at which it is harnessed were increased. Compared against single-PCM packed beds, MLSPCM designs yielded a much higher efficiency in the use of total capacity. Compared against the two-tank system, a MLSPCM prototype with a volume 32% higher than that of one tank (C3), resulted equivalent in terms of energy and exergy delivered to

the power block. Such prototype needs only 32% of the amount of molten-salt needed by the two-tank system. On the other hand, the total weight held by the MLSPCM design is 62% higher and it requires a relatively small amount of PCM (less than 4% of total weight). Compared against a single-solid filled thermocline tank with the same dimensions, C3 resulted in a thermal storage around 20% higher, holding almost the same weight (around 3% less) and needing around 8% more molten-salt, apart from the extra PCM layers. The second analysis, which incorporated more aspects related to the operation of the CSP plant, resulted in lower differences between the performance of MLSPCM and single-solid thermocline configurations. This was explained by the less restrictive operating conditions for the TES systems, which reduced the thermocline degradation in single-solid prototypes; and by the fact of having days with low radiation penalizing the extent in which the systems with higher capacity were used. Nevertheless, MLSPCM prototypes tested still showed higher values of stored energy/exergy and efficiency (C2 and C3) than single-solid thermocline tanks. When compared against the reference 2-tank system, prototype C3 still resulted equivalent to it, since the values of stored energy and exergy obtained were almost exactly the same. In these conditions, prototype A2 delivered around 10% less energy/exergy to the power block than C3 in the 17 days of simulation. Thermal losses to the ambient were observed to be very low for all the cases (less than 1%), and the tank walls and foundation acted as extra thermal storage media. Therefore, MLSPCM concept showed to be promising as an alternative to the other TES configurations tested, as well as to the standard two-tank system. However, variability of operating conditions were observed to affect the relative advantage of using one or another TES system, and therefore, it is possible that TES designs which are optimal for the isolated conditions are not so for the real application. Optimization of MLSPCM designs to one or another CSP facility needs to be studied in further detail, with long-term simulations incorporating all the relevant aspects, such as the real limitations for the HTF temperature, the different thermo-physical properties of the available PCMs and the economic evaluation.

As a final remark, it is worth noting that the developed numerical models are also applicable to many different problems than those treated in this work. With the solid-liquid CFD model, problems such as the manufacturing of glass, crystals and metals and the preservation of food and medicaments could be simulated. With the packed bed TES model, thermal storage in low temperature applications could be evaluated. Furthermore, the MLSPCM concept for single-tank thermal storage can also be of use in applications different from CSP.

6.2 Further research

Although the formulation for the case of phase change occurring at a temperature range —in which a mushy region is formed— was developed, no case simulated in this work corresponds to such situation. In this kind of problem, there are some parameters, such as the coefficient of the momentum source term (S) and the $h - T$ relation, that should be "tuned" for each material and case. This work should be addressed in the future, although the needed experimental data for validation are difficult to obtain.

On the other hand, although with the developed model it is already possible to perform simulations of solidification processes, in order to be able to simulate all the phenomena involved (nucleation, anisotropy of the thermal conductivity) more physics should be added.

Another interesting subject for further research is to extend the solid-liquid model to incorporate the possibility to simulate the movement of the solid phase and its dynamical interaction with the liquid phase. This would allow to increase the capabilities of the model, allowing the simulation of —for example— the unconstrained melting of PCM in capsules, which would be of great use in the applications of interest of this thesis.

Furthermore, the coupling of the solid-liquid phase change model with other multiphase models, such as level-set of VOF, would allow the simulation of phenomena in which liquid, solid and gas phases participate. This, for example, would enable to predict the behavior of encapsulated PCM taking into account the void space left for allowing thermal expansion.

In order to complete the analysis of thermal storage including PCM capsules, useful correlations of melting rate and Nusselt numbers could be drawn from the CFD simulations for their incorporation into the TES single-tank code.

An advantage of fixed-grid models, such as the presented in the first two chapters, is that it is closely related to the equations of fluid flow through porous media, since the liquid-solid interface is modeled as such. This is another natural link between the different subjects of study of this thesis. It is expected that the development carried out in the solid-liquid phase change modeling may serve as a starting point for future developments of porous media models, for their application into CFD modeling of packed beds and thermocline tanks.

Regarding MLSPCM TES systems, further research should address optimization issues, with long-term simulations incorporating all the relevant aspects, such as the real limitations for the HTF temperature, the different thermo-physical properties of the available PCMs and the economic evaluation. Moreover, analysis of MLSPCM TES systems for CSP central tower plants —with the consequent increase in the higher operating temperature— should also be carried out. The promising results obtained with MLSPCM designs should also lead to their experimental evaluation in the future.

References

[1] F. L. Tan, S. F. Hosseinizadeh, J. M. Khodadadi, and L. Fan, "Experimental and computational study of constrained melting of phase change materials (PCM) inside a spherical capsule," *Int. J. Heat Mass Tran.*, vol. 52, pp. 3464–3472, 2009.

[2] W. Zhao, Elmozughi, A.F., A. Oztekin, and S. Neti, "Heat transfer analysis of encapsulated phase change material for thermal energy storage," *Int. J. Heat Mass Tran.*, no. 63, pp. 323–335, 2013.

Appendix A

Main publications in the context of this thesis

A.1 Journal papers

- P. Galione, O. Lehmkuhl, J. Rigola, and A. Oliva, “Fixed-grid modeling of solid-liquid phase change in unstructured meshes using explicit time schemes,” *Numer. Heat Tr. B-Fund.*, vol. 65, pp. 27–52, 2014.
- P. A. Galione, O. Lehmkuhl, J. Rigola and A. Oliva, "Fixed-grid numerical modeling of melting and solidification using variable thermo-physical properties —Application to the melting of n-Octadecane inside a spherical capsule," submitted to *International Journal of Heat and Mass Transfer*, 2014.
- P. A. Galione, C. D. Pérez-Segarra, I. Rodríguez, A. Oliva, and J. Rigola, “Multi-layered solid-PCM thermocline thermal storage concept for CSP plants. Numerical analysis and perspectives.” submitted to *Applied Energy*, 2014.
- P. A. Galione, C.D. Pérez-Segarra, I. Rodríguez, S. Torras and J. Rigola, "Multi-layered solid-PCM thermocline thermal storage for CSP. Numerical evaluation of its application in a 50MWe plant.", submitted to *Applied Energy*, 2014.

A.2 Conference papers

- P. Galione, C. D. Pérez-Segarra, I. Rodríguez, S. Torras, and J. Rigola, "Numerical evaluation of multi-layered solid-PCM thermocline-like tanks as thermal energy storage systems for CSP applications," in Proceedings of the *SolarPACES 2014 International Conference*, Beijing, China, 2014.

- P. A. Galione, O. Lehmkuhl, J. Rigola, C. D. Pérez-Segarra and A. Oliva, "Unstructured 3D numerical modeling of the melting of a PCM contained in a spherical capsule," in Proceedings of the *ECCOMAS 2014 —6th European Conference on Computational Fluid Dynamics (ECFD VI)*, Barcelona, Spain, 2014.

- P. A. Galione, C. D. Pérez-Segarra, I. Rodríguez, O. Lehmkuhl, J. Rigola and A. Oliva, "Numerical modeling and experimental validation of encapsulated PCM Thermal Energy Storage tanks for Concentrated Solar Power Plants," in Proceedings of the *Eurotherm Seminar #99 —Advances in Thermal Energy Storage*, Lleida, Spain, 2014.

- S. Torras, J. Castro J. Rigola, S. Morales, P. Galione, O. Lehmkuhl and A. Oliva, "Numerical modeling and experimental validation of Thermal Energy Storage tanks for propulsion systems under cryogenic conditions.," in Proceedings of the *Eurotherm Seminar #99 —Advances in Thermal Energy Storage*, Lleida, Spain, 2014.

- P. Galione, C. D. Pérez-Segarra and I. Rodríguez, O. Lehmkuhl, and J. Rigola, "A new thermocline-pcm thermal storage concept for csp plants. numerical analysis and perspectives," in *Proceedings of the SolarPACES 2013 International Conference*, vol. 49 of *Energy Procedia*, pp. 790–799, Elsevier, 2014.

- P. Galione, J. Rigola, J. Castro and I. RodrÃguez, "Solid-liquid phase change with turbulent flow," in Proceedings of *Turbulence, Heat and Mass Transfer 7*, Palermo, Italy, 2012.

- J. Castro, P. Galione, S. Morales, O. Lehmkuhl, J. Rigola, C. D. Pérez-Segarra, A. Oliva. "Numerical modelling of the phase change material heat accumulator under fast transient gasification conditions in a low thrust cryogenic propulsion (ltcp) system," in Proceedings of *Space Propulsion 2012*, Bordeaux, France, 2012.

- P. Galione, Lehmkuhl, O., J. Rigola, A. Oliva, and R. I, "Numerical simulations of energy storage with encapsulated phase change materials. Special emphasis on solid-liquid phase change CFD modelling," in *Proc. 12th Int. Conf. Energy Storage (INNOSTOCK)*, no. INNO-SP-56, 2012.